TUDelft

Delft University of Technology

Modeling CO$_2$ dissociation in microwave plasma reactors through quasi-steady state non-equilibrium vibrational kinetics

Moreno Wandurraga, Sergio

Important note
To cite this publication, please use the final published version (if applicable).
Please check the document version above.

MODELING CO₂ DISSOCIATION IN MICROWAVE PLASMA REACTORS THROUGH QUASI-STEADY STATE NON-EQUILIBRIUM VIBRATIONAL KINETICS

MODELING CO₂ DISSOCIATION IN MICROWAVE PLASMA REACTORS THROUGH QUASI-STEADY STATE NON-EQUILIBRIUM VIBRATIONAL KINETICS

Dissertation

for the purpose of obtaining the degree of doctor
at Delft University of Technology
by the authority of the Rector Magnificus prof.dr.ir. T.H.J.J. van der Hagen
chair of the Board for Doctorates
to be defended publicly on
Wednesday 15 July 2020 at 12:30 o'clock

by

Sergio Hernando MORENO WANDURRAGA

Master of Science in Mechanical Engineering
Delft University of Technology, the Netherlands
born in Bucaramanga, Colombia

This dissertation has been approved by the promotors

Composition of the doctoral committee:
  Rector Magnificus   Chairperson
  Prof.dr.ir. A. I. Stankiewicz   Delft University of Technology, promotor
  Prof.dr. G. Stefanidis   KU Leuven, Belgium, promotor

  Independent members:
  Prof.dr. D.J.E.M. Roekaerts   Delft University of Technology
  Prof.dr.ir. M.C.M. van de Sanden   Eindhoven University of Technology
  Prof.dr.ir. L. Lefferts   University of Twente
  Prof.dr. H. Geerlings   Delft University of Technology
  Dr. J. E. Lang   Evonik Industries AG, Germany
  Prof.dr.ir. W. de Jong   Delft University of Technology
                                (reserve member)

To my parents,
Maria Elvira y Leonardo.

CONTENTS

SUMMARY

Plasma reactors emerge as a promising alternative to cope with some of the biggest challenges currently faced by humanity, the global warming, the increasing global energy demand and the need for efficient storage of electricity from renewable energy sources. Plasma reactors have the potential to enable the storage of green renewable electricity into fuels and chemicals through processes whereby CO_2 can be used as a feedstock. Owing to these potential benefits there is a need to investigate this technology from a chemical and process engineering perspective.

Big challenges are still hindering the development of plasma reactors into a feasible industrial technology. Despite its limitations, computer modelling is an excellent tool to tackle such challenges. It is well known that the chemistry of non-thermal plasmas is usually the most challenging and complex part of plasma modelling due to the large number of species and reactions involved, which can reach hundreds and thousands ones, respectively; hence, there is need for practical approaches to study, design and optimize plasma reactors. This thesis summarizes the research performed towards the development of engineering approaches to study and model plasma reactors by taking CO_2 dissociation in a non-thermal microwave plasma reactor as the case study.

The vibrational kinetics of CO_2 under the typical conditions of non-thermal microwave plasma are studied through an isothermal reaction kinetics model. The importance of the different collisional processes is evaluated throughout the conditions and timescales at which the CO_2 dissociation takes place. The long timescale behavior of the vibrational-to-translational temperature ratio at different conditions is discussed and it is shown that its behavior at increasing gas temperatures can be fitted to an algebraic expression. This temperature ratio has been identified as a key variable to achieve an energetically efficient dissociation.

The vibrational-to-translational temperature ratio is shown to be useful for the reduction of vibrational kinetics, enabling their implementation in practical engineering models. A novel reduction methodology is developed and demonstrated for the case of CO_2 by lumping relevant vibrationally excited states within a single

group. Through this methodology, the dissociation and vibrational kinetics of CO_2 can be captured in a reduced set of reactions, dramatically decreasing the calculation time of the model.

A two-step modelling approach for plasma reactors is also developed. The approach is applied for the case of CO_2 dissociation in a surface wave microwave plasma reactor. The reduction methodology is applied to incorporate the vibrationally enhanced dissociation of CO_2 in the chemistry of the model. The model predictions are compared to experimental results to validate the model and obtain insight into the performance of the reactor.

The reduction methodology and the modelling approach are the result of studying the CO_2 dissociation in a non-thermal microwave plasma reactor. Nonetheless, these are based on general fundamentals that apply to other types of discharges and chemistries as well. The modelling approach can be used for process engineering applications involving the design, optimization and verification of plasma reactors and their performance. The reduction methodology can be implemented in the modelling approach when the vibrationally enhanced dissociation is considered relevant.

SAMENVATTING

In het licht van de uitdagingen zoals de opwarming van de aarde, de toenemende energiebehoefte en de noodzaak voor efficiënte opslag van energie gegenereerd door hernieuwbare bronnen die de mens heeft, geven plasma reactoren een veelbelovend alternatief, Plasma reactoren hebben de potentie om de energie uit hernieuwbare bronnen om te zetten in brandstoffen en chemicaliën door middel van processen waarbij CO_2 als grondstof kan worden gebruikt. Met dit in gedachte is er een behoefte voor verder onderzoek naar deze technologie vanuit een chemisch en procestechnologie oogpunt.

Er zijn grote uitdagingen in het ontwikkelen van plasma reactoren naar een industrieel relevante technology. Modellering met behulp van computers is een uitstekende tool in het beantwoorden van deze uitdagingen, ondanks de huidige limitaties. Het is algemeen bekend dat normaliter de scheikunde van niet-thermische plasmas de grootste uitdaging en complexiteit levert in het modelleren van plasma, vanwege de grote aantallen reacties en intermediairen, die soms tot in de honderden of duizenden oplopen. Dit resulteert in de noodzaak voor pragmatische aanpakken in de studie, design en optimalisatie van plasma reactoren. Deze dissertatie vat het onderzoek samen dat is uitgevoerd met als doel de ontwikkeling van technische methodieken voor de studie en modellering van plasma reactoren met CO_2 dissociatie in een niet-thermische microgolf plasma reactor als onderzoek voorbeeld.

De vibrationele kinetiek van CO_2 onder typische condities van een niet-thermische microgolf plasma zijn onderzocht door middel van een isothermisch reactiekinetiek model. Het belang van verschillende botsing processen is geëvalueerd onder verschillende condities en tijdschalen waaronder CO_2 dissociatie plaats vindt. Het gedrag van vibrationele-tot-translationele temperatuur verhoudingen op langere tijdschalen en onder verschillende condities is onderzocht. Geobserveerd is dat het gedrag bij toenemende temperaturen van het gas kan omschreven worden door middel van een algebraïsche formule. Het is vastgesteld dat deze temperatuur ratio een kritische variabele is in het bereiken van een energetische efficiënte dissociatie.

Het is aangetoond dat de vibrationele-tot-translationele temperatuur ratio bruikbaar is voor het reduceren van vibrationele kinetiek, wat de implantatie toelaat in pragmatische engineering modellen. Een innovatieve reductie methodologie is ontwikkeld en de toepassing hiervan is aangetoond met behulp van een case study van CO_2 waarbij de relevante vibrationele, hoog-energetische toestanden tot een enkele groep zijn gereduceerd. Met behulp van deze methodologie, kan de dissociatie en de vibrationele kinetiek van CO_2 omschreven worden met een gereduceerde set van reacties, wat tot een dramatische afname van de benodigde berekeningstijd leidt.

Vervolgens is een twee-stap aanpak voor het modelleren van plasma reactoren ontwikkeld. Deze aanpak is toegepast op de CO_2 dissociatie in een oppervlakte golf microgolf plasma reactor. De reductie methodologie is toegepast om de door vibratie verhoogde dissociatie van CO_2 in het model te incorporeren. De uitkomsten van het model zijn vergeleken met de experimentele resultaten om het model te valideren en inzicht in de prestatie van de reactor te krijgen.

Het reductie model en de modellering aanpak zijn het resultaat van de studie van CO_2 dissociatie in een niet-thermische microgolf plasma reactor. Zowel de methodologie als de aanpak zijn gebaseerd op basisprincipes die ook voor andere types van ontladingen en scheikunde gelden. De modellering aanpak kan ook gebruikt worden voor procestechnologische toepassingen, zoals onder meer het ontwerp, optimalisatie en verificatie van plasma reactoren en de prestaties van deze. De reductie methodologie kan geïmplementeerd worden in de modellering aanpak wanneer de verhoogde dissociatie door middel van vibraties relevant wordt geacht.

1

INTRODUCTION

1.1. CO_2 as a feedstock

Global warming as a result of the accumulation of greenhouse gases in the atmosphere is an undeniably fact. Numerous studies support the claim that human activity, particularly after the industrial revolution ca. 1750, have modified the climate patterns mainly due to the emission of greenhouse gases. These gases reside in the atmosphere, absorbing and emitting radiation in the infrared spectrum. The surface temperature of the Earth is regulated through this process and without these gases we would freeze. On the contrary, at high concentrations of greenhouse gases, the infrared radiation from the Earth's surface cannot escape and thus the planet gets heated. It is also known that, among the greenhouse gases, CO_2 makes the largest contribution to global warming due to its high concentration and long atmospheric lifetime.

After the industrial revolution, the main source of CO_2 emissions is the combustion of fossil fuels. Great efforts have been made to reduce CO_2 emissions, mainly by developing sustainable energy technologies and by pushing the transition from a fossil-fuel based economy to a sustainable economy. Nevertheless, this transition poses additional challenges, such as the intermittent and fluctuating nature of some renewable sources. Wind turbines and solar panels generate electricity only when the wind is blowing and the sun is shining. In addition to this unsteady and almost unpredictable behavior there are also diurnal and seasonal variations. Therefore, there is a need for efficient means to store any surplus of green electricity on peak production-low demand periods so that it can be used in high demand-low production periods. Efficient electricity storage is thus critical to ensure a reliable and stable green electricity grid.

Electricity storage technologies should have a fast response time to cope with sudden fluctuations, as well as high energy efficiency to minimize losses in the energy conversion process and a high energy density to facilitate the handling and transportation of the energy carrier. In this regard, liquid fuels are still the most convenient energy carriers due to their higher gravimetric and volumetric energy density in comparison to other energy carriers, see figure 1.1. This characteristic property of energy carriers is important for energy intensive applications in remote locations and crucial for portable applications such as transportation, for which the energy carrier is transported within. For instance, freight and long-distance passenger transportation are energy intensive applications that may operate for long

periods of time before restocking the energy carrier. Liquid fuels, either fossil or synthetic, will probably remain as the best energy carrier for some important applications.
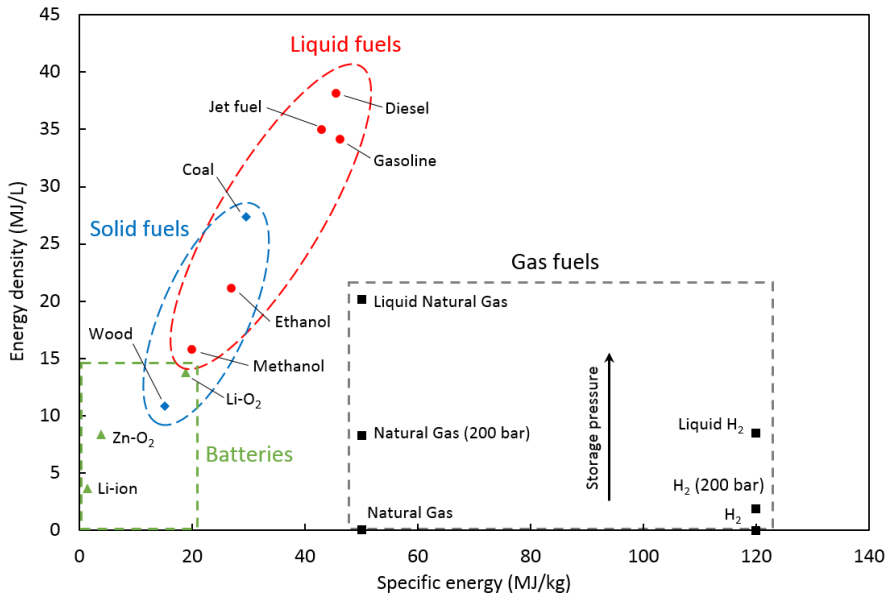
Fig. 1.1. Energy content per unit mass and unit volume for selected energy carriers. Adapted from [1–3].

The implementation of sustainable energy technologies is not enough to stop CO_2 emissions. Several technologies aimed at capturing CO_2 are therefore under development and implementation. Carbon Dioxide Removal (CDR) and Carbon Capture and Storage (CCS) are a group of technologies intended to capture and store the CO_2. In the former, the CO_2 is directly removed from the atmosphere, whereas in the latter the CO_2 is captured from large point sources, such as factories and powerplants. The captured CO_2 is then stored, usually in underground geological formations to avoid contact with the atmosphere. Despite the efficiency of these technologies, there is uncertainty regarding the security of the storage, especially the probability of CO_2 leakage to the atmosphere over a long period of time.

A different approach is taken by Carbon Capture and Utilization (CCU) technologies, whereby the captured CO_2 is not stored but utilized. The major challenge in these technologies is the CO_2 utilization, as this molecule is known to

be very stable. Indeed, conventional chemical processes have come short in finding energetically efficient and carbon neutral processes able to brake or react the CO_2 molecule. Most of the energy used in industrial processes, particularly heat, still comes from fossil fuel and thus contributes to make conventional utilization processes unsustainable. Therefore, to achieve a sustainable CO_2 utilization, non-conventional process technologies running on green electricity must be considered.

Microwave plasma is a promising non-conventional technology that can enable CO_2 utilization. Indeed, microwave plasma reactors have the potential to enable the production of synthetic fuels from captured CO_2. In the Solar Fuels concept, renewable electricity surplus can be used to power a microwave plasma reactor and synthetize fuels from green hydrogen and captured CO_2 in a single process step. This process allows for chemical storage of green electricity into a fuel that can later be used locally, during high demand-low production periods. The solar fuel can also be used elsewhere, as one advantage of fuels is the existing infrastructure for their transportation and utilization. In the current context of increasing energy demand and predicted scarcity of fossil fuels, the solar fuels are a plausible and sustainable alternative.

The challenge that for a long time had been presented as of how to reduce CO_2 emissions should now be substituted by how to utilize CO_2. An energetically efficient and carbon neutral (or negative) recycling of the carbon atoms within the emitted CO_2 is the challenge to overcome. Additional applications, besides synthetic fuels, can be opened by splitting the CO_2 molecule and utilizing the produced CO as feedstock in subsequent chemical processes. Microwave plasma reactors can also enable such route and bring us closer to a sustainable economy.

1.2. The benefits of non-thermal plasma reactors

Plasma is usually regarded as the fourth state of the matter. The transition from gas to plasma eventually takes place when enough energy is put into a gas, either from a heat source or an electromagnetic field. In plasma, molecules dissociate and electrons lose their bonds, forming ions in the process. Plasma is an ionized gas, a mixture of neutrals, ions and electrons that exhibit a collective behavior and is electrically quasi-neutral. The plasma state is sustained as long as new electrons are produced to replace those that diffuse to the walls or become lost in collisions.

When this condition is not met, the plasma ceases to exist, recombination processes take place and the gas state is obtained again.

Plasma occurs spontaneously in nature, as in the case of lightning or solar corona. Artificial plasmas, best known as gas discharges, are usually generated at low pressures by using electromagnetic fields (figure 1.2). Indeed, it is mostly at low pressures that the unique characteristics of plasma enable the intensification of chemical processes. Temperatures and energies in a plasma reactor can significantly exceed those of conventional chemical processing technologies, producing a high concentration of energetic and chemically active species. These species trigger reactions that in ordinary chemistry are difficult or even impossible to achieve [4].
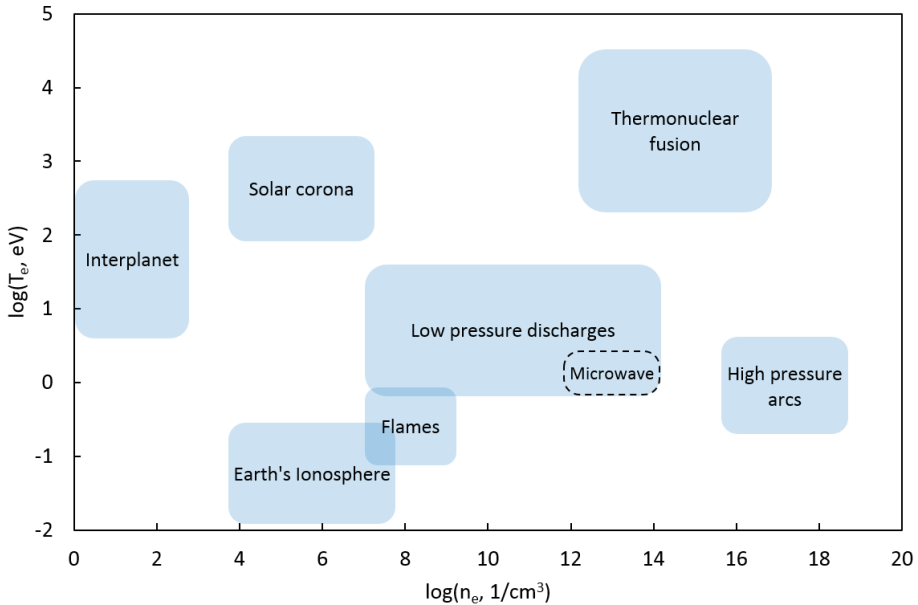
Fig. 1.2. Typical values of electron temperature, T_e, and electron number density, n_e, for selected natural and artificial plasmas. Adapted from [4,5]. (1 eV $\approx$ 11600 K).

Plasmas are classified in thermal and non-thermal plasmas. The former is in quasi-equilibrium and its chemical processes are described by a single temperature. On the contrary, non-thermal plasma can be far from thermodynamic equilibrium and is characterized by multiple temperatures, which are related to different species and their excited states. The chemical processes in this plasma can be determined by

other temperatures different than the gas temperature, enabling high temperature chemistry at low gas temperatures. Non-thermal plasma is usually generated at low pressures, low powers or pulsed discharges. It is also more selective than thermal plasma as the energy is used to generate a high number of excited species instead of being used to heat the background gas.

The characteristics of non-thermal plasma reactors are favorable for the dissociation and utilization of CO_2. Plasma reactors offer additionally benefits, such as compactness, robustness and fast response time to temporal variations at the inlet [6,7]. They are therefore a suitable technology to cope with the intermittent and fluctuating pattern of renewable sources.

Among the plasma technologies, the non-thermal microwave plasma is particularly efficient in splitting the CO_2 molecule, reaching energy efficiencies up to 90% [4]. Microwave plasma is usually generated at low pressures, between 100 and 300 Torr, and is characterized by low electron temperatures $T_e \approx 0.5 - 2$ eV, high electron densities $n_e \approx 10^{12} - 10^{14}$ 1/cm^3 and ionization degrees around 10^{-5} [4,8,9] (figure 1.2). The vibrational excitation of the CO_2 molecule has been identified as the means to achieve such high energy efficiencies. High vibrational excitation rates are related to low electron temperatures and high electron densities (figure 1.2).

The mechanism behind the efficient dissociation of CO_2 is the vibrationally enhanced dissociation, in which the vibrational energy in the asymmetric mode can effectively reduce the energy barrier of the dissociation reaction. In such way, the endothermic reaction is carried out efficiently, breaking the very stable CO_2 molecule with less heating of the gas. In a nutshell, under adequate conditions, the low-lying asymmetric vibrational states get excited by electron collisions and they transfer their energy to higher vibrational states thus creating an overpopulation of highly energetic states that can easily dissociate. This is claimed to be the most efficient dissociation mechanism.

Despite the potential benefits of CO_2 dissociation in microwave plasma reactors, there are still big challenges to overcome to make this a feasible industrial technology [10,11]. There is a well-known trade-off between high chemical conversion and high energy efficiency [12], e.g. for the highest reached energy efficiency of 90%

the chemical conversion was lower than 15% - 20% [4]. Due to the complexity of non-thermal chemistry, all chemical processes taking place in the discharge are not fully understood [8]. Other concerns are the scalability of the reactors and the instabilities that arise at pressures closer to atmospheric values while attempting to maintain the non-equilibrium characteristics of the plasma [4,13].

The dissociation of CO_2 in microwave plasma has experimentally been investigated for decades [14]. More recently, various techniques have been used to gain new insight into the effect of different reactor configurations, operating conditions and gas compositions on the behavior of CO_2-containing plasmas [9,12,13,15–27]. Despite the extensive experimental research, there are still many uncertainties that must be addressed to fully understand the non-thermal plasma processes. Therefore, there is a need to develop reliable plasma reactor models to improve our understanding of the plasma processes, evaluate different reactor designs and optimize the performance of microwave plasma reactors.

1.3. Challenges of modeling non-thermal plasma reactors

Computer modelling is an excellent tool to deal with the scientific and engineering challenges of plasma reactors. Diverse aspects hindering this technology can be tackled through computer modelling; for instance, the fundamental understanding of molecular processes can be improved, the reaction rates constants can be validated, and the design and scalability of the reactors can be explored.

Different modelling approaches have recently been used to get insight into the plasma processes and the reactor performance [8,28–38]. The State-To-State (STS) kinetic model is still the most common approach to gain fundamental understanding of the physical and chemical processes taking place in a non-thermal plasma. STS kinetic models consider relevant interactions among distinct energy states of atoms and molecules. The energy states of atoms and molecules are considered as separate species and their interactions as independent reactions. Thus, a large number of species (tens to hundreds) and a huge number of reactions (hundreds to thousands) are common in this approach. Additional efforts have been made to reduce the very complex STS kinetic models into manageable reduced kinetic models suitable to multidimensional models, which are intended to improve the design and performance of plasma reactors [39,40].

There are also many challenges in modelling non-thermal plasma reactors. Regarding zero-dimensional kinetic models, some processes taking place inside the plasma are still not fully understood, or have not even been identified. Furthermore, crucial data required for modelling, such as cross sections or rate constants, are not available. Regarding the more complex multidimensional self-consistent models, their physics involve variables whose time and lengths scale differ widely in magnitude, making the non-linear system of equations numerically challenging to solve. For instance, the self-consistent model of non-thermal microwave plasma reactor solves for the electromagnetic wave propagation, electrostatics, mass conservation and diffusion, fluid dynamics, energy conservation and heat transfer, reaction kinetics and the drift diffusion equations for electrons.

Given the potential of the plasma reactor technology, it is beneficial to investigate its performance from a chemical or process engineering point of view. There is need for practical engineering plasma models that consider dimensionality and transport, and ultimately allow for integration of a plasma reactor to a process system.

1.4. Scope of the thesis

This thesis summarizes the research performed towards the development of engineering approaches to study and model non-thermal plasma reactors. The study of non-thermal plasma requires specific knowledge of plasma physics and chemistry; therefore, prior knowledge in plasma is necessary for the reader of this book. Nonetheless, this research has been performed from an engineering perspective and this thesis has been written accordingly.

The study is centered on the dissociation of CO_2 in a non-thermal microwave plasma reactor. For this purpose, the CO_2 plasma is studied under the typical experimental conditions and the timescales at which the dissociation takes place. Although limited to this type of discharge, the study is based on more general fundamentals that apply to other types of discharges as well. Hence, the reduction methodology, the modelling approach and the findings can potentially be applied to discharges with similar characteristics, i.e. sustained high electron energies and low electron temperatures. Likewise, even though the chemistry is restricted to that of pure CO_2 plasma, given its current relevance and potential applications, the

reduction methodology, the modelling approach and the findings can potentially be applied to similar chemistries, i.e. pure molecular plasmas of diatomic and triatomic molecules.

This research aims to address the following research questions:

1. Which are the most relevant molecular processes for CO_2 dissociation in a non-thermal microwave plasma reactor under typical experimental conditions? (Chapters 2, 3).

2. Is there a key parameter that influences the vibrationally enhanced dissociation of CO_2? What is this parameter, how can it be computed and how does it vary in the discharge? (Chapters 2, 3).

3. How can complex state-to-state kinetics, particularly vibrational kinetics, be drastically reduced so that they can be implemented in engineering models that consider dimensionality and transport? (Chapters 2, 3, 4).

4. How can process engineering models of non-thermal plasma reactors that consider process equipment inputs (power and process conditions) and reactor performance evaluation (conversion and energy efficiency) be made? (Chapters 3, 4).

1.5. Outline of the thesis

This thesis is organized in five chapters, starting from a general introduction to some main challenges faced by human society, which are also main drivers of the research in plasma reactors, and a brief overview of the technology and the challenges to overcome. The subsequent chapters are organized in a logical manner, from the plasma chemistry of detailed state-to-state vibrational kinetics to the modelling and evaluation of a microwave plasma reactor from an engineering perspective. The last chapter is dedicated to the conclusions of this research. A brief summary of the chapters' content is given next.

Chapter 1 introduces the context and motivations driving this research. The potential applications of non-thermal plasma reactors are given in the context of global warming, the increasing global energy demand, the migration to renewable

energy sources and the need for efficient storage of green electricity. A brief introduction to plasma and non-thermal plasma reactors is also given, together with the challenges that are hindering the development of this technology. Plasma modelling is presented as an excellent tool to cope with such challenges, despite having its own difficulties, which are also mentioned in brief. The research questions behind this research are also presented in this chapter.

In Chapter 2 the vibrational kinetics of CO_2 under the typical conditions of non-thermal microwave plasma are studied by using an STS reaction kinetic model. The influence of the different collisional processes is evaluated throughout the conditions and timescales at which the CO_2 dissociation takes place. Likewise, the long timescale behavior of the vibrational-to-translational temperature ratio at different conditions is discussed in detail and it is shown that its behavior at increasing gas temperatures can be fitted to an algebraic expression. The limitations of this approximation are also discussed, specifically the conditions and timescales at which it yields better results.

Chapter 3 introduces a reduction methodology to simplify vibrational kinetics and enable their implementation into multidimensional models. The four key elements of the methodology are discussed in detail and demonstrated for the case of CO_2: 1) lump the vibrational levels in a fictitious species CO_2^*, 2) compute the population distribution of these vibrational levels, 3) use the algebraic expression developed in Chapter 2 to approximate the vibrational temperature and 4) calculate reaction rate constants for the species CO_2^*. By using this methodology, it is shown that the dissociation and vibrational kinetics of CO_2 can be captured in a reduced set of reactions, substantially decreasing the calculation time of the kinetic model.

A two-step modelling approach for plasma reactors is presented in Chapter 4. The approach is applied for the case of CO_2 dissociation in a non-thermal surface wave microwave plasma reactor. The reduced vibrational kinetics developed in Chapter 3 are used to include the vibrationally enhanced dissociation of CO_2 in the chemistry of the model. The modelling results are compared with the experimental results and the dominant dissociation paths in the plasma reactor are discussed in detail. Limitations of the modelling approach are discussed as well, especially those with major contribution to the discrepancies between experimental and

modelling results. The relation between Chapters 2, 3 and 4 is displayed in figure 1.3.

Finally, in Chapter 5, the conclusions drawn from this research are summarized and an outlook on the technology of non-thermal microwave plasma reactors is also given.

Chapter 2
Study of the CO_2 vibrational kinetics (STS kinetic model).
- Evaluation of collisional processes and their timescales.
- Analysis of the vibrational-to-translational temperature ratio.

Algebraic expression to approximate the vibrational-to-translational temperature ratio at increasing gas temperatures.

Chapter 3
Reduction methodology for vibrational kinetics (applied for CO_2).
- Lump the vibrational levels in the fictitious species CO_2^*.
- Make use of the algebraic expression developed in Chapter 2.

Reduced vibrational kinetics for CO_2 dissociation in a non-thermal microwave discharge.

Chapter 4
Two-step modelling approach for plasma reactors (applied for CO_2).
- Make use of the reduced vibrational kinetics developed in Chapter 3.
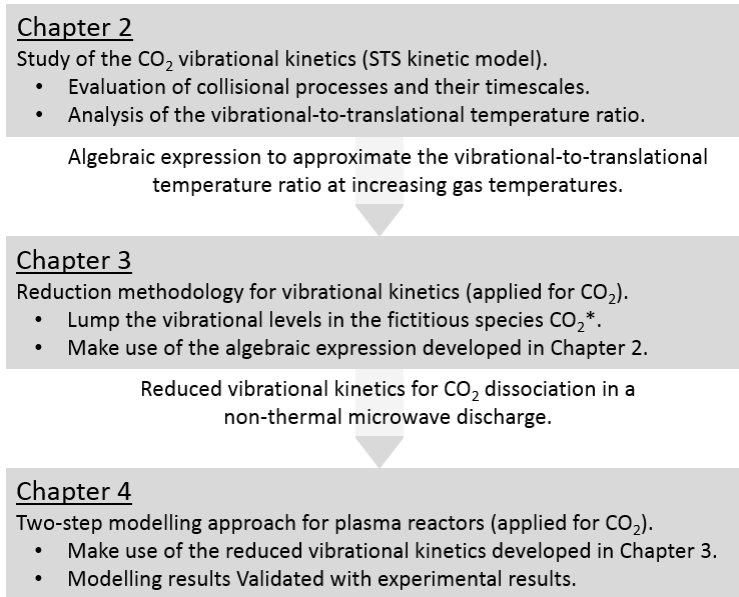- Modelling results Validated with experimental results.

Fig. 1.3. Relationship between Chapters 2,3 and 4. The chapters follow a logical sequence, from the small scales of vibrational levels and collisional processes to the larger scales of microwave plasma reactor modeling from an engineering point of view.

References

1 P. . Edwards, V. . Kuznetsov and W. I. . David, *Philos. Trans. R. Soc. A Math. Phys. Eng. Sci.*, 2007, **365**, 1043–1056.

2 L. J. Hardwick and C. P. de León, *Johnson Matthey Technol. Rev.*, 2018, **62**, 134–149.

3 C. F. Shih, T. Zhang, J. Li and C. Bai, *Joule*, 2018, **2**, 1925–1949.

4 A. Fridman, *Plasma chemistry*, Cambridge University Press, 2008.

5 M. A. Lieberman and A. J. Lichtenberg, *Principles of Plasma Discharges and Materials Processing*, John Wiley & Sons, Inc., Hoboken, NJ, USA, 2005.

6 Q. Wang, B. Spasova, V. Hessel and G. Kolb, *Chem. Eng. J.*, 2015, **262**, 766–774.

7 J. R. Roth, *Industrial Plasma Engineering*, IOP Publishing Ltd., 1995, vol. 1.

8 T. Kozák and A. Bogaerts, *Plasma Sources Sci. Technol.*, 2015, **24**, 015024.

9 T. Silva, N. Britun, T. Godfroid and R. Snyders, *Plasma Sources Sci. Technol.*, 2014, **23**, 025009.

10 A. Lebouvier, S. a. Iwarere, P. D'Argenlieu, D. Ramjugernath and L. Fulcheri, *Energy & Fuels*, 2013, **27**, 2712–2722.

11 J. F. de la Fuente, A. A. Kiss, M. T. Radoiu and G. D. Stefanidis, *J. Chem. Technol. Biotechnol.*, 2017, **92**, 2495–2505.

12 L. F. Spencer and A. D. Gallimore, *Plasma Sources Sci. Technol.*, 2013, **22**, 015019.

13 W. Bongers, H. Bouwmeester, B. Wolf, F. Peeters, S. Welzel, D. van den Bekerom, N. den Harder, A. Goede, M. Graswinckel, P. W. Groen, J. Kopecki, M. Leins, G. van Rooij, A. Schulz, M. Walker and R. van de Sanden, *Plasma Process. Polym.*, 2017, **14**, 1600126.

14 V. D. Rusanov, A. a. Fridman and G. V. Sholin, *Uspekhi Fiz. Nauk*, 1981, **134**, 185.

15 G. Chen, N. Britun, T. Godfroid, V. Georgieva, R. Snyders and M.-P. Delplancke-Ogletree, *J. Phys. D. Appl. Phys.*, 2017, **50**, 084001.

16 N. den Harder, D. C. M. van den Bekerom, R. S. Al, M. F. Graswinckel, J. M. Palomares, F. J. J. Peeters, S. Ponduri, T. Minea, W. A. Bongers, M. C. M. van de Sanden and G. J. van Rooij, *Plasma Process. Polym.*, 2017, **14**, 1600120.

17 C. M. Mitsingas, R. Rajasegar, S. Hammack, H. Do and T. Lee, *IEEE Trans. Plasma Sci.*, 2016, **44**, 651–656.

12

18   J. F. de la Fuente, S. H. Moreno, A. I. Stankiewicz and G. D. Stefanidis, *Int. J. Hydrogen Energy*, 2016, **41**, 21067–21077.

19   J. F. de la Fuente, S. H. Moreno, A. I. Stankiewicz and G. D. Stefanidis, *Int. J. Hydrogen Energy*, 2017, **42**, 12943–12955.

20   I. Belov, V. Vermeiren, S. Paulussen and A. Bogaerts, *J. CO2 Util.*, 2018, **24**, 386–397.

21   M. Tsuji, T. Tanoue, K. Nakano and Y. Nishimura, *Chem. Lett.*, 2001, **1**, 22–23.

22   T. Oberreuther, C. Wolff and A. Behr, *IEEE Trans. Plasma Sci.*, 2003, **31**, 74–78.

23   A. Vesel, M. Mozetic, A. Drenik and M. Balat-Pichelin, *Chem. Phys.*, 2011, **382**, 127–131.

24   S. Dobrea, I. Mihaila, V. Tiron and G. Popa, *Rom. Reports Phys.*, 2014, **66**, 1147–1154.

25   T. Silva, N. Britun, T. Godfroid and R. Snyders, *Plasma Process. Polym.*, 2017, **14**, 1600103.

26   T. Silva, N. Britun, T. Godfroid, J. van der Mullen and R. Snyders, *J. Appl. Phys.*, 2016, **119**, 173302.

27   N. Britun, T. Silva, G. Chen, T. Godfroid, J. van der Mullen and R. Snyders, *J. Phys. D. Appl. Phys.*, 2018, **51**, 144002.

28   T. Kozák and A. Bogaerts, *Plasma Sources Sci. Technol.*, 2014, **23**, 045004.

29   M. Capitelli, G. Colonna, G. D'Ammando and L. D. Pietanza, *Plasma Sources Sci. Technol.*, 2017, **26**, 055009.

30   T. Silva, M. Grofulović, B. L. M. Klarenaar, A. S. Morillo-Candas, O. Guaitella, R. Engeln, C. D. Pintassilgo and V. Guerra, *Plasma Sources Sci. Technol.*, 2018, **27**, 015019.

31   P. Diomede, M. C. M. van de Sanden and S. Longo, *J. Phys. Chem. C*, 2017, **121**, 19568–19576.

32   P. Diomede, M. C. M. van de Sanden and S. Longo, *J. Phys. Chem. A*, 2018, **122**, 7918–7923.

33   E. V. Kustova and E. A. Nagnibeda, *Chem. Phys.*, 2006, **321**, 293–310.

34   E. V. Kustova and E. A. Nagnibeda, *Chem. Phys.*, 2012, **398**, 111–117.

35   I. Armenise and E. Kustova, *J. Phys. Chem. A*, 2018, **122**, 8709–8721.

36   L. D. Pietanza, G. Colonna, G. D'Ammando, A. Laricchiuta and M. Capitelli, *Plasma Sources Sci. Technol.*, 2015, **24**, 042002.

37   L. D. Pietanza, G. Colonna, G. D'Ammando, a. Laricchiuta and M. Capitelli, *Chem. Phys.*, 2016, **468**, 44–52.

38   L. D. Pietanza, G. Colonna, G. D'Ammando and M. Capitelli, *Plasma Phys. Control. Fusion*, 2017, **59**, 014035.

39   J. F. de la Fuente, S. H. Moreno, A. I. Stankiewicz and G. D. Stefanidis, *React. Chem. Eng.*, 2016, **1**, 540–554.

40   A. Berthelot and A. Bogaerts, *Plasma Sources Sci. Technol.*, 2016, **25**, 045022.

2

BEHAVIOR AND MODELING OF THE VIBRATIONAL-TO-TRANSLATIONAL TEMPERATURE RATIO AT LONG TIME SCALES IN CO₂ VIBRATIONAL KINETICS

Non-thermal microwave plasma reactors can efficiently split the CO_2 molecule. However, big challenges remain before this technology becomes a feasible industrial technology. Computer modeling can be very useful to tackle such challenges. Detailed kinetic modeling is commonly used to get insights into the complex vibrational kinetics of CO_2 as vibrational excitation is strongly related to the energy efficiency in the dissociation process. The vibrational-to-translational temperature ratio has been identified as a key variable to achieve high energy efficiencies. This ratio has also been used to simplify detailed CO_2 vibrational kinetics, notably reducing the number of species and reactions required to model the non-thermal plasma. In this paper we use an isothermal reaction kinetics model to study the vibrational kinetics of CO_2 under the typical conditions used in non-thermal microwave plasma experiments. The importance of the different collisional processes is evaluated throughout the conditions and timescales at which CO_2 dissociation takes place. The long timescale behavior of the vibrational-to-translational temperature ratio at different conditions is discussed in detail. It is shown that its behavior at increasing gas temperatures can be fitted to an expression that incorporates the Landau-Teller temperature dependence. This is confirmed by average Adjusted R-square values higher than 0.99 and average Root Mean Square Error values smaller than 0.22 at low gas temperatures. The limitations of the fitting expression are also discussed, specially the conditions and timescales at which it yields better results.

2.1. Introduction

Non-thermal microwave plasma reactors have been experimentally proven to be successful in splitting the CO_2 molecule [1–9]. Moreover, the vibrational excitation of the asymmetric stretching mode has been identified as the means to achieve energy efficiencies as high as 90% [10]. It is claimed that the energy stored in this vibrational mode can effectively reduce the energy barrier of endothermic reactions. In such way, the dissociation reaction is carried out efficiently, breaking the CO_2 molecule with less heating of the gas. In this dissociation mechanism, low-lying asymmetric vibrational states get excited through electron collisions and they transfer their energy to higher vibrational states thus creating an overpopulation of highly energetic states that can easily dissociate. Further information on this mechanism can be found elsewhere [10,11].

Some pieces are still missing in the puzzle of making CO_2 dissociation in microwave plasma reactors a feasible industrial technology, e.g. the well-known trade-off between high chemical conversion and high energy efficiency. In this regard, computer modeling is a resourceful tool to cope with the challenges ahead. Diverse aspects hindering plasma reactors technology can be tackled through computer modeling, for instance, the fundamental understanding of molecular processes can be improved, the reaction rates constants can be validated and the scalability of the reactors can be explored.

Different modeling approaches have been used to get insights into the plasma processes and the reactor performance [12–22]. The detailed study of vibrational kinetics requires the calculation of population densities for different vibrational energy levels, usually the full span, from ground state to dissociation limit. The complete vibrational distribution of a vibrational mode is determined by including all its vibrational levels in the study and analyzing their different interactions. In such cases, two approaches are usually employed. The most common approach is the State-To-State (STS) kinetic model, in which energy states of atoms and molecules are considered as separate species and their relevant interactions are considered as independent reactions (elementary steps). In this approach the energy levels are considered discrete and a large number of species and reactions are not rare. A more recent approach [14,15] replaces the discrete energy levels by a continuous vibrational energy function. The equation for the rate of change of the species is thus replaced by a drift-diffusion Fokker-Plank equation, with transport

parameters computed from rate constants of state to state interactions. This approach has the potential to be much more computationally efficient than the traditional STS kinetic model approach.

Additional efforts have been addressed to reduce the very complex STS kinetics models into manageable kinetics models suitable to multidimensional models, which are intended to improve the design and performance of plasma reactors [23,24]. In our previous research on the matter we proposed a reduction methodology that employs the vibrational to translation temperature ratio as a key parameter for the reduction of the vibrational kinetics [23]. In this reduction methodology, all asymmetric vibrational levels of CO_2 are grouped within the fictitious species CO_2^* and the vibrational to translation temperature ratio is used to compute weighted algebraic rate constants of reactions involving CO_2^*. The application of this methodology results in a dramatic reduction of the number of reactions and species required to describe the vibrationally enhanced dissociation of CO_2. Recently, the reduction methodology has been used in a two-step modeling approach to model a surface wave microwave plasma reactor [25]. The importance of this temperature ratio has also been discussed in other works [14,15,26], where it is mentioned that the non-equilibrium effect leading to the vibrationally enhanced dissociation of CO_2 is better exploited at high values of this ratio. Higher values of the temperature ratio lower the energy level for the point of no return, beyond which vibrationally excited molecules most likely increase their vibrational energy and dissociate.

In this paper we use an isothermal STS reaction kinetics model to study the vibrational kinetics of CO_2, particularly the kinetics of the asymmetric vibrational mode. In addition, the effect of symmetric sublevels on the kinetics of asymmetric levels is also investigated. The analysis is limited to the typical experimental conditions used for pure CO_2 dissociation in non-thermal microwave plasma and the timescales at which this dissociation takes place. The relevance of the different collisional processes is also evaluated throughout the conditions and timescales. Finally, the long timescale behavior of the vibrational to translational temperature ratio is discussed in detailed as it has been identified as a key variable to achieve an efficient dissociation.

2.2. Model description

The reaction kinetics model solves the particle conservation equation for all the species in the plasma. It represents the plasma as point in space, disregarding dimensionality and transport. The rate of change of a species is given by the chemical reactions and is computed from the following equation

$$\frac{dn_i}{dt} = \sum_k \left(\nu_{i,k}^{\text{R}} - \nu_{i,k}^{\text{L}} \right) \left(k_{k,\text{f}} \prod_i n_i^{\nu_{i,k}^{\text{L}}} - k_{k,\text{r}} \prod_i n_i^{\nu_{i,k}^{\text{R}}} \right) \tag{2.1}$$

where n_i is the number density of the species i, $\nu_{i,k}^{\text{R(L)}}$ is the right(left)-hand-side stoichiometric coefficient of the species i in reaction k and $k_{k,\text{f(r)}}$ is the forward (reverse) reaction rate constant for reaction k. Elementary reactions between specific energy states of the CO_2 molecule are included in this STS reaction kinetics model. The electron density n_e and electron temperature T_e are assumed constant, as well as the heavy species temperature T.

Table 2.1. Species considered in the CO_2 model.

Type	Species
Neutral ground state (1)	CO_2
Vibrationally excited states (84)	$CO_2\nu_a$, $CO_2\nu_b$, $CO_2\nu_c$, $CO_2\nu_n$, $CO_2\nu_{n,a}$, $CO_2\nu_{n,b}$, $CO_2\nu_{n,c}$
Charged species (2)	CO_2^+, e

The species considered in the model are CO_2 species and electrons, see table 2.1. To preserve the electroneutrality of the plasma the CO_2 ion density is made equal to the electron density. The analysis of the CO_2 vibrational kinetics is the objective of this paper and therefore no other species different than CO_2 are included. Moreover, no specific rotationally or electronically excited states of CO_2 are considered, as they have no direct influence in the vibrational kinetics. These excited states affect the vibrational kinetics through the variation of the electron temperature, which is a parameter of this kinetic model. The vibrational state of the CO_2 molecule is specified by three quantum numbers $(i_1\ i_2\ i_3)$, indicating the vibrational levels in the symmetric stretching, symmetric bending and asymmetric stretching vibrational modes, respectively. Symmetric bending levels have a degeneracy of $i_2 + 1$ as the bending can take place in orthogonal planes. Stretching modes are non-degenerate. Furthermore, the vibrational levels

$((i_1 + 1)\, i_2\, i_3)$ and $(i_1\, (i_2 + 2)\, i_3)$ are coupled due to the proximity of their energy, they coexist and are therefore grouped into a single species. In this case, the total degeneracy of the species is the sum of the degeneracies of the grouped states and is referred to as statistical weight.

Table 2.2. Vibrationally excited species, their energies and statistical weights.

Species	Vibrational states $(i_1\, i_2\, i_3)$	Energy (eV) $E_{(i_1\, i_2\, i_3)}$	Statistical Weight $\sum(i_2 + 1)$
$CO_2\nu_a$	(0 1 0)	0.083	2
$CO_2\nu_b$	(0 2 0) + (1 0 0)	0.166	4
$CO_2\nu_c$	(0 3 0) + (1 1 0)	0.250	6
$CO_2\nu_n$	(0 0 n)	$E_{(0\, 0\, n)}$	1
$CO_2\nu_{n,a}$	(0 1 n)	$E_{(0\, 1\, n)}$	2
$CO_2\nu_{n,b}$	(0 2 n) + (1 0 n)	$E_{(0\, 2\, n)}$	4
$CO_2\nu_{n,c}$	(0 3 n) + (1 1 n)	$E_{(0\, 3\, n)}$	6

The first three symmetric bending levels are included in the model as purely symmetric vibrational species and as "sublevels" of asymmetric vibrational states, see table 2.2. The symmetric levels are denoted by the subscripts *a*, *b* and *c*, and the asymmetric vibrational levels are denoted by the index *n*. The vibrational energy levels can be computed from the triatomic anharmonic oscillator model, which to the second order of approximation reads [27]

$$\frac{E_{(i_1\, i_2\, i_3)}}{hc} = \sum_n \omega_n (i_n + d_n/2) + \sum_{m \geq n} x_{nm}(i_n + d_n/2)(i_m + d_m/2) + x_{l_2 l_2} l_2^2 \qquad (2.2)$$

where $E_{(i_1\, i_2\, i_3)}$ is the vibrational energy, h is the Planck constant, c the speed of light, i_n and d_n the vibrational quantum number and the degeneracy of the vibrational mode n, respectively. The special quantum number l_2 related to the quasi-rotation around the principal axis of the molecule is assumed to be 0. The spectroscopic constants are given in table 2.3.

According to this model and these spectroscopic constants, the first asymmetric level has an energy of 0.29 eV and the asymmetric level 21, with an energy of 5.47 eV, lies in the dissociation limit of the molecule (5.5 eV). It is assumed that this level is the highest asymmetric level before the molecule dissociates. Thus, the index *n* in $CO_2\nu_n$ runs from 1 to 21, whereas in $CO_2\nu_{n,(a,b,c)}$ runs from 1 to 20.

Table 2.3. Spectroscopic constants for computing the vibrational energy levels of CO_2 [27].

Constant	Value (1/cm)
ω_1	1354.31
ω_2	672.85
ω_3	2396.32
x_{11}	-2.93
x_{12}	-4.61
x_{13}	-19.82
x_{22}	1.35
x_{23}	-12.31
x_{33}	-12.47
$x_{l_2 l_2}$	-0.97

Figure 2.1 shows the vibrational energy scale with selected species in the model. It is clear from this figure that the symmetric levels are closer together and that $CO_2 v_{n-1,(a,b,c)} < CO_2 v_n$, therefore the "sublevel" designation. Moreover, due to the anharmonicity of the molecule, the vibrational levels come closer as the energy increases.
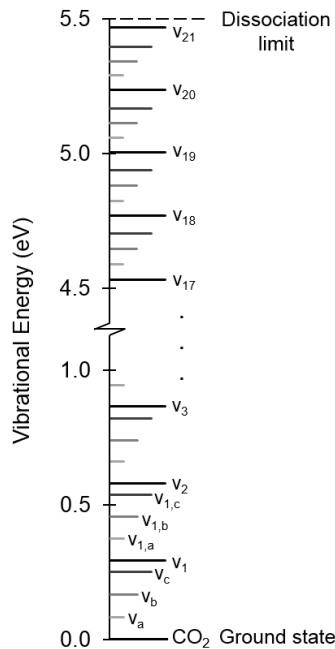

Fig. 2.1. Vibrational energy levels of selected CO_2 species in the model, from equation 2.2. Asymmetric level 21 is the highest asymmetric level, thus, for $CO_2 v_n$ $n = 1, 2, \ldots, 21$, whereas for $CO_2 v_{n,(a,b,c)}$ $n = 1, 2, \ldots, 20$. See also appendix A.

The set of reactions is based on the vibrational kinetics developed by Kozák et al [12,13]. Notable differences are the addition of symmetric sublevels and their reactions, the gradual relaxation of symmetric (sub)levels b and c, and the assumption of a Maxwellian Electron Energy Distribution Function (EEDF). Dissociation reactions are excluded as well as reactions between charged species. The considered reactions are thus limited to electron impact vibrational excitation and vibrational relaxation, along with their reverse reactions. The rate constants for the latter are computed from the detailed balance principle, which ensures that under thermal equilibrium conditions at a temperature T^* the correct densities for the vibrational levels are obtained

$$k_{k,r} = k_{k,f} \frac{\prod g^L}{\prod g^R} \exp\left(\frac{-(\sum E^L - \sum E^R)}{T^*}\right) \tag{2.3}$$

where $g^{L(R)}$ and $E^{L(R)}$ are the statistical weight and the energy of a species at the left(right)-hand-side of the reaction, respectively, and T^* is the temperature governing the reaction, T_e for electron impact reactions and T for heavy species reactions.

Table 2.4. Electron impact reactions. Forward rate constants computed from the cross sections of the references.

No	Reaction	Ref	Note
eVs1	$e + CO_2 \leftrightarrow e + CO_2 v_a$	28	A
eVs2	$e + CO_2 \leftrightarrow e + CO_2 v_b$	29	A
eVs3	$e + CO_2 \leftrightarrow e + CO_2 v_c$	28	A
eVa1	$e + CO_2 \leftrightarrow e + CO_2 v_1$	28	B

Notes

A: For symmetric sublevels, $e + CO_2 v_n \leftrightarrow e + CO_2 v_{n,(a,b,c)}$. The cross sections are shifted according to the threshold energy of the reaction $E_{th} = E_{n,(a,b,c)} - E_n$.

B: The cross section is shifted and scaled for the excitation from an asymmetric level n to a higher asymmetric level m, $e + CO_2 v_n \leftrightarrow e + CO_2 v_m$. Fridman's approximation is used with scaling factors $\alpha = 0.5$ and $\beta = 0$ [10].

Table 2.4 lists the electron impact reactions included in the model. Through these reactions the kinetic energy of the electrons is transferred to the CO_2 molecule as vibrational energy. Due to the lack of experimental data the cross sections of the reactions shown in table 2.4 are used to compute the cross sections of reactions involving higher vibrational levels. Reactions eVs1-3 correspond to the vibrational

excitation of the first three symmetric levels and their cross sections are shifted to compute the cross sections of the analogous reactions forming symmetric sublevels, $e + CO_2\nu_n \leftrightarrow e + CO_2\nu_{n,(a,b,c)}$. This translation is done according to the threshold energy for the sublevel excitation $E_{th} = E_{n,(a,b,c)} - E_n$. The cross section for the vibrational excitation of the first asymmetric level, Reaction eVa1, is scaled and shifted to compute the cross section for the vibrational excitation from any asymmetric level n to a higher asymmetric level m, $e + CO_2\nu_n \leftrightarrow e + CO_2\nu_m$. Fridman's approximation[10] with scaling factors $\alpha = 0.5$ and $\beta = 0$ is used for the calculation of the cross sections. All cross sections are integrated with a Maxwellian EEDF for different electron temperatures to obtain the rate constants of the reactions as functions of the electron energy.

Table 2.5. Vibrational relaxation reactions. Rate constants in (m^3/s). VT: Vibrational-Translational (s: symmetric, a: asymmetric), VV': Intermode Vibrational-Vibrational, VV: Intramode Vibrational-Vibrational.

No	Reaction	Forward rate constant, $k_{k,f}$	Ref	Note
VTs1	$CO_2\nu_a + CO_2 \leftrightarrow CO_2 + CO_2$	$7.14 \times 10^{-14}\exp\left(-177T^{-1/3} + 451T^{-2/3}\right)$	30	A
VTs2	$CO_2\nu_b + CO_2 \leftrightarrow CO_2\nu_a + CO_2$	$1.94 \times 10^{-13}\exp\left(-177T^{-1/3} + 451T^{-2/3}\right)$	30	A
VTs3	$CO_2\nu_c + CO_2 \leftrightarrow CO_2\nu_b + CO_2$	$2.90 \times 10^{-13}\exp\left(-177T^{-1/3} + 451T^{-2/3}\right)$	30	A
VTa1	$CO_2\nu_1 + CO_2 \leftrightarrow CO_2\nu_a + CO_2$	$4.25 \times 10^{-7}\exp\left(-407T^{-1/3} + 824T^{-2/3}\right)$	30	B
VTa2	$CO_2\nu_1 + CO_2 \leftrightarrow CO_2\nu_b + CO_2$	$8.57 \times 10^{-7}\exp\left(-404T^{-1/3} + 1096T^{-2/3}\right)$	30	B
VTa3	$CO_2\nu_1 + CO_2 \leftrightarrow CO_2\nu_c + CO_2$	$1.43 \times 10^{-11}\exp\left(-252T^{-1/3} + 685T^{-2/3}\right)$	30	B
VV'1	$CO_2\nu_1 + CO_2 \leftrightarrow CO_2\nu_a + CO_2\nu_b$	$2.13 \times 10^{-11}\exp\left(-242T^{-1/3} + 633T^{-2/3}\right)$	30	C
VV1	$CO_2\nu_1 + CO_2\nu_1 \leftrightarrow CO_2 + CO_2\nu_2$	$1.8 \times 10^{-17}\exp\left(24.7T^{-1/3} - 65.7T^{-2/3}\right)$	13,31,32	D

Notes

A: For symmetric sublevels, $CO_2\nu_{n,(a,b,c)} + CO_2 \leftrightarrow CO_2\nu_{n,(,a,b)} + CO_2$.

B: Scale as $CO_2\nu_n + CO_2 \leftrightarrow CO_2\nu_{n-1,(a,b,c)} + CO_2$ for higher asymmetric levels.

C: Scales as $CO_2\nu_n + CO_2 \leftrightarrow CO_2\nu_{n-1,a} + CO_2\nu_b$ and $CO_2\nu_n + CO_2 \leftrightarrow CO_2\nu_{n-1,b} + CO_2\nu_a$ for higher asymmetric levels.

D: Scales as $CO_2\nu_n + CO_2\nu_m \leftrightarrow CO_2\nu_{n-1} + CO_2\nu_{m+1}$ for asymmetric levels n and m.

The vibrational relaxation reactions in the model include Vibrational-Translational relaxation (VT), Intramode Vibrational-Vibrational relaxation (VV) and Intermode Vibrational-Vibrational relaxation (VV'), see table 2.5. In the VT relaxation process, energy is transferred between the vibrational and translational (heat) degrees of freedom. Reactions VTs1-3 correspond to VT relaxation of symmetric (sub)levels in a descending ladder fashion, i.e. $\nu_{(n,)c} \xrightarrow{\text{VTs3}} \nu_{(n,)b} \xrightarrow{\text{VTs2}} \nu_{(n,)a} \xrightarrow{\text{VTs1}} \nu_{(n)}$. The rate constants are assumed to be the same for the relaxation of symmetric sublevels as the asymmetric mode does not take part in the process.

Reactions VTa1-3 correspond to the VT relaxation of an asymmetric level n to a lower asymmetric level $n-1$ with a symmetric sublevel a, b or c, i.e. $v_n \xrightarrow{\text{VTa1(2,3)}} v_{n-1,a(b,c)}$. The latter subsequently relaxes through reactions VTs1-3, losing its symmetric sublevels and becoming purely asymmetric again. Therefore, the combined effect of the VT reactions can be seen as an asymmetric VT relaxation process from level n to level $n-1$. Nevertheless, the addition of symmetric sublevels has an effect on the kinetics of this relaxation process.

In the VV' relaxation process, the energy is transferred between different vibrational modes, i.e. between the asymmetric and the symmetric modes in this case. Through this reaction, a fraction of the energy from the asymmetric mode is transferred to the symmetric modes of the collision partner. Thus, for a reacting asymmetric level n, the outcome is a lower asymmetric level $n-1$ with a symmetric sublevel a or b and the excitation of the ground state CO_2 to a symmetric level b or a, respectively, see notes in table 2.5. In the VV relaxation process the energy is transferred between levels of the same vibrational mode, i.e. the asymmetric mode in this model. This process is fast, nearly resonant, due to the small energy losses related to the anharmonicity of the molecule. Through this process, the vibrational energy predominantly flows toward higher levels due the lower energy requirement. The reverse process is not as efficient since the additional energy must be taken form the translational degree of freedom. The rate constants for the reactions VTa1-3, VV'1 and VV1 are computed as done by Kozák et al [12,13]. The complete reaction scheme for an asymmetric vibrational level n is illustrated in figure 2.2.
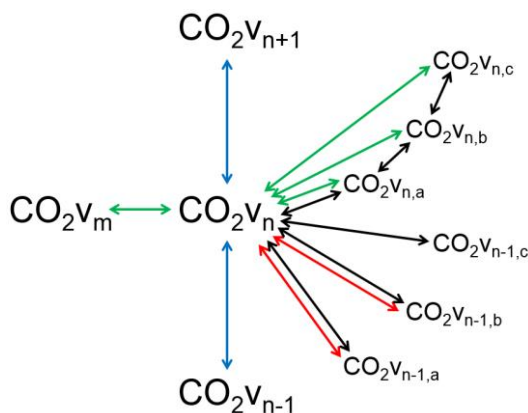

Fig. 2.2. Vibrational reactions scheme for a species CO_2v_n, showing eV reactions (green), VV relaxation (blue), VT relaxation (black) and VV' relaxation (red).

2.3. Results

The isothermal vibrational kinetics model was implemented on the Heavy Species Transport Module of the commercial software COMSOL Multiphysics, see appendix A for further details. This module can be configured to solve for equation 2.1 in a single 1D uniform element, having three parameters as inputs for the model: the electron mean energy $\bar{\varepsilon} = {}^3/_2\, T_e$, n_e and T. Pressure has no influence on the heavy species reactions as the number of reacting species is the same at either side of the reaction. The influence of the pressure on the electron impact reactions can be eliminated by choosing the electron density in a way that the ratio of electrons to neutral species, i.e. the ionization degree $\alpha = n_e\, /n_n$, remains unchanged for the same temperature T. The parameters were varied within the range of typical values for CO_2 dissociation experiments in non-thermal microwave plasmas, with $\bar{\varepsilon} = 0.75, 1.5, 2.25$ eV ($T_e = 0.5, 1, 1.5$ eV); $n_e = 10^{18}, 10^{19}, 10^{20}$ $1/m^3$ and $T = 300 - 1500$ K, in steps of 200 K. The temperature range is also restricted to these values due to the validity of the forward rate constant expressions [30]. The pressure was held constant at 100 torr for all calculations.

Figure 2.3 shows the steady state vibrational distribution functions (VDF) of the asymmetric mode for different set of reactions, at $T_e = 1$ eV (~ 11600 K), $T = 900$ K and $n_e = 10^{18}$ $1/m^3$. The VDFs have been normalized to facilitate the comparison of results, thus, the shown densities correspond to the relative populations of the asymmetric vibrational levels CO_2v_n with respect to the ground state CO_2. The Boltzmann distributions at the gas and electron temperatures are also shown for reference. These distributions are also obtained if vibrational relaxation (VV + VT + VV') and excitation processes (eV) are considered separately. Clearly, these processes are competing to bring the CO_2 species into thermal equilibrium with their corresponding driving temperatures, T or T_e. The VDFs that result from including both processes, relaxation and excitation, should therefore lie within these Boltzmann distributions. Nevertheless, as seen in figure 2.3, the densities of high vibrational levels can exceed their corresponding densities of the Boltzmann distribution at T_e. When eV and VV reactions are considered together, the well-known Treanor distribution [33] is obtained. This distribution is the result of the vibrational excitation (determined by T_e), the vibrational energy

exchange (determined by T) and the anharmonicity of the molecule. The combined effect is the preferential flow of vibrational energy to highly excited levels.
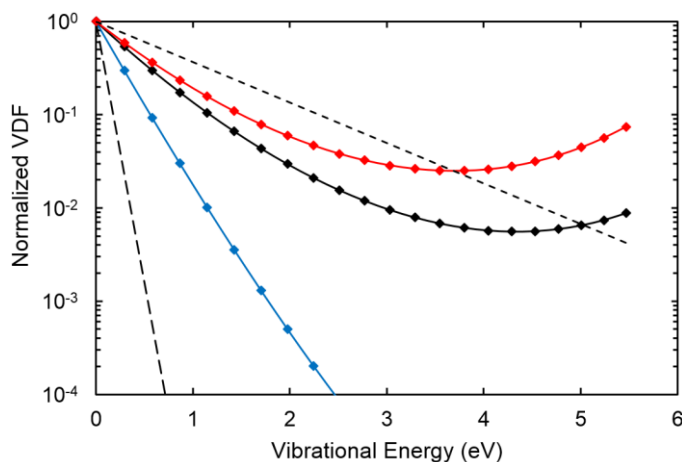

Fig. 2.3. Normalized steady state vibrational distribution function for different sets of reactions. Results with eV + VV in red (Treanor distribution), eV + VV + VT + VV' in black and eV + VV + VT + VV' without symmetric sublevels (Kozák) in blue. Boltzmann distributions at T (long dash) and at T_e (short dash) shown for reference. Calculations performed at $T_e = 1$ eV ($\sim$11600 K), $T = 900$ K and $n_e = 10^{18}$ 1/m^3.

Treanor-like VDFs can also be obtained when the processes for vibrational energy "loss", VT and VV', are included in the calculations. The VDF obtained for the complete vibrational kinetics model, shown in black in figure 2.3, indicates that eV and VV dominate over VT and VV' at the mentioned conditions. Favorable conditions for the Treanor effect are high electron densities and low electron temperatures, to ensure high vibrational excitation rates, and low heavy species temperatures to maintain a low rate of vibrational energy loss. The rates of vibrational energy exchange (VV) are high even at low temperatures due to its nearly-resonant characteristic. Figure 2.3 also shows that a Treanor-like VDF was not obtained when an instant VT relaxation of the symmetric sublevels is assumed. This assumption neglects the sequential fashion of the VT relaxation of symmetric sublevels and therefore speeds up the VT relaxation of the asymmetric levels.

The vibrational excitation of the system is commonly indicated by the vibrational temperature, T_V, which should lie between the temperatures driving the competing processes, T_e and T. The vibrational temperature of the asymmetric mode, based on

the first vibrational level, can be computed from $T_V = E_1/\ln(n_0/n_1)$. It is important to remark that this vibrational temperature refers to the departure from equilibrium of the first vibrational level and provides no information about the population of higher vibrational levels unless a defined VDF is assumed, e.g. Boltzmann or Treanor distribution.

Table 2.6 lists the steady state vibrational temperatures for the same sets of reactions of figure 2.3, with $T_e = 1$ eV, $n_e = 10^{18}$ 1/m^3 and $T = 300, 900$ and 1500 K. For the case of eV + VV reactions the vibrational temperature increases with the gas temperature. The reason for this behavior is that there is almost no vibrational energy lost to the translational mode, the gas temperature approaches the electron temperature and the rate of vibrational energy exchange increases, rising the Treanor distribution and partially straightening it as well. The effect of the symmetric sublevels in the complete vibrational kinetics model is also evident when comparing the vibrational temperatures obtained with and without these sublevels. At 300 K the effect of the symmetric sublevels is small, the vibrational temperatures are very close and the VDFs at the low energy region are similar. At 900 K the vibrational temperature obtained when considering the symmetric sublevels almost doubles the vibrational temperature obtained by assuming an instant relaxation of symmetric sublevels (see also figure 2.3). At 1500 K the VT relaxation rates further increase and difference between the vibrational temperatures decreases to 50%.

Table 2.6. Steady state vibrational temperatures in K for selected gas temperatures and sets of reactions. Calculations performed at $T_e = 1$ eV (~11600 K) and $n_e = 10^{18}$ 1/m^3.

Reactions	Gas Temperature (K)		
	300	900	1500
eV + VV	2762	6470	8274
eV + VV + VT + VV'	2967	5430	3045
eV + VV + VT + VV' (no sublevels)	3076	2802	2037

The variation in the vibrational temperatures of table 2.6 can also be understood by analyzing the characteristics times of the kinetic processes in the plasma. These are computed from the rate constants of the reactions and the densities of colliding partners and provide insights into the timescales at which the different processes take place. The characteristic time for the electron impact vibrational excitation of the asymmetric mode is computed from the corresponding rate constant and the

electron density, $\tau_{eVa} = (k_{eVa1}(T_e)n_e)^{-1}$. For electron temperatures between $0.5 - 1.5$ eV and an electron density of 10^{19} $1/m^3$ this characteristic time has an order of magnitude of $\sim 10^{-6}$ s. This value of the electron density corresponds to an ionization degree of $\sim 10^{-5}$ for a pressure of 100 torr and a gas temperature of 900 K. The characteristic times for vibrational relaxation are computed similarly and the results are presented in table 2.7.

Table 2.7. Order of magnitude of characteristic relaxation times in (s), for a pressure of 100 torr and gas temperatures of 300 K and 1500 K.

Characteristic time	300 K	1500 K	Note
$\tau_{\mathrm{VTs}} = \left(k_{\mathrm{VTs}}(T)n_g(T)\right)^{-1}$	10^{-5}	$10^{-7} - 10^{-6}$	A
$\tau_{\mathrm{VTa}} = \left(k_{\mathrm{VTa}}(T)n_g(T)\right)^{-1}$	$10^{-4} - 10^{0}$	$10^{-7} - 10^{-5}$	B
$\tau_{\mathrm{VV'}} = \left(k_{\mathrm{VV'}}(T)n_{\mathrm{CO_2}}(T)\right)^{-1}$	10^{-5}	10^{-7}	C
$\tau_{\mathrm{VV}} = \left(k_{\mathrm{VV}}(T)n_{\mathrm{CO_2}}(T)\right)^{-1}$	10^{-9}	10^{-8}	D

Notes

A: VT relaxation of symmetric sublevels, $CO_2v_c \rightarrow CO_2v_b \rightarrow CO_2v_a \rightarrow CO_2$. Computed from rate constants of reactions VTs1-3 and gas density. The relaxation time is shorter for higher sublevels, $\tau_{\mathrm{VTs3}} \lesssim \tau_{\mathrm{VTs2}} \lesssim \tau_{\mathrm{VTs1}}$.

B: VT relaxation of asymmetric levels, $CO_2v_1 \rightarrow CO_2v_a$, $CO_2v_1 \rightarrow CO_2v_b$, $CO_2v_1 \rightarrow CO_2v_c$. Computed from rate constants of reactions VTa1-3 for the relaxation of the first asymmetric vibrational level. In general, for the studied temperature range, $\tau_{\mathrm{VTa3}} \approx \tau_{\mathrm{VTa2}} \ll \tau_{\mathrm{VTa1}}$.

C: VV' relaxation, $CO_2v_1 + CO_2 \rightarrow CO_2v_a + CO_2v_b$. Computed from the CO_2 density and the rate constant of reaction VV'1 for the relaxation of the first asymmetric vibrational level.

D: VV relaxation, $CO_2v_1 + CO_2 \rightarrow CO_2 + CO_2v_1$. Computed from the scaled rate constant of reaction VV1.

A quick comparison of the results in table 2.7 indicates that the fastest process is VV relaxation and the slowest process is the VT relaxation of asymmetric levels (VTa). VV' relaxation takes place at timescales comparable to that of VT relaxation of symmetric sublevels (VTs). Indeed, symmetric sublevels are formed in the VV' relaxation and a lower asymmetric sublevel is attained only after VTs relaxation takes place. Since VTs relaxation takes place in a descending ladder fashion, the limiting step is the VT relaxation of the lowest symmetric sublevel a, which is the bottleneck of the process (see note A in table 2.7). Likewise, at high temperatures the VT relaxation of sublevel a also hinders the VTa relaxation, particularly the reactions whereby sublevels b or c are formed (see note B in table 2.7). Therefore, the relaxation of symmetric sublevels hinders the relaxation of

asymmetric levels, resulting in Treanor-like VDFs (see figure 2.3) and higher vibrational temperatures (see table 2.6) when these are considered.

At low temperatures, the relation $\tau_{VV} \ll \tau_{eVa} < \tau_{VTs} < \tau_{VTa}$ holds. VV relaxation is ~3 orders of magnitude faster than electron impact vibrational excitation, implying that the latter limits the rate at which high vibrational levels are reached. In other words, significant excitation of high vibrational levels can only take place at timescales longer than ~10^{-6} s. Moreover, vibrational excitation and vibrational energy exchange processes are faster than vibrational energy loss processes, leading thus to an overpopulation of high vibrational levels (Treanor effect). At high temperatures, the relation is $\tau_{VV} \ll \tau_{eVa} \sim \tau_{VTs} \sim \tau_{VTa}$, with VV relaxation still ~2 orders of magnitude faster than electron impact vibrational excitation. VT relaxation takes place at shorter timescales, comparable to those of electron impact vibrational excitation, and therefore no significant vibrational excitation is achieved (see table 2.6). For the conditions used in the calculation of the characteristic times, the vibrational kinetics model reaches the steady state at timescales of ~$10^{-4} - 10^{-3}$ s. However, the VDF is mostly developed at shorter timescales (~10^{-5} s) and slowly approaches its steady state form.

Table 2.6 shows that, for the complete kinetic model, the vibrational temperature increases as the gas temperature increases from 300 K to 900 K. At a gas temperature of 1500 K, the vibrational temperature decreases to approximately the same value obtained with a gas temperature of 300 K. This behavior is not observed in the non-thermal degree of the plasma, T_V/T, which is shown in figure 2.4 for different values of the parameters T_e, n_e and T. This temperature ratio is an intrinsic comparison of VV and VT relaxation, which are competing processes in the vibrational energy transfer to higher levels. It is seen in figure 2.4 that T_V/T decreases as the gas temperature increases for all combinations of the studied electron density and electron temperature values. Moreover, for high values of the electron density (top and middle graphs in figure 2.4) the temperature ratio decreases in a very similar fashion. At higher temperatures it is expected that the curves approach the value of 1 and thus $T_V = T$, as clearly seen for the lowest electron density (bottom graph in figure 2.4). In addition, for the lowest electron density and high electron temperatures, the decrease in the temperature ratio is not as smooth as seen in other curves of figure 2.4. This is partially explained by the calculation method, in which the electron density and electron mean energy are

fixed to specific values removing their inherent interdependency. The ionization rate coefficient is given by the ionization cross section and the EEDF. For a Maxwellian EEDF, the ionization rate coefficient increases with the electron temperature. The calculations were therefore performed considering all combinations of electron densities and electron temperatures, acknowledging that the calculation method decouples these variables.

Nonetheless, a rough estimate of the relation between the electron density and electron temperature can be obtained by solving the steady state of the electron impact ionization and dissociative recombination reactions for different values of the electron temperature. The total ionization cross section [28] of reaction $e + CO_2 \rightarrow 2e + CO_2^+$ is used in the calculations. Likewise, the rate constant given by $2.0 \times 10^{-11} T_e^{-0.5} T_g^{-1}$ (m³/s) [34] is used for the dissociative recombination reaction, $e + CO_2^+ \rightarrow CO + O$. It is further assumed that CO and O instantaneously recombine to form CO_2 again. The results of these calculation are presented in table 2.8.

Table 2.8. Steady state electron density for selected values of the electron temperature. Calculations performed at a pressure of 100 torr.

T_e (eV)	n_e (1/m³)	α (T = 300 K)	α (T = 1500 K)
1.00	4.1×10^{17}	1.3×10^{-7}	6.4×10^{-7}
1.25	8.4×10^{18}	2.6×10^{-6}	1.3×10^{-5}
1.50	6.6×10^{19}	2.0×10^{-5}	1.0×10^{-4}
1.75	3.0×10^{20}	9.2×10^{-5}	4.6×10^{-4}
2.00	9.4×10^{20}	2.9×10^{-4}	1.5×10^{-3}

Electron densities in orders of magnitude between 10^{17} and 10^{20} $1/m^3$ were obtained for electron temperatures between 1.00 and 2.00 eV, resulting in ionization degrees ranging from 10^{-7} to 10^{-3} in the gas temperature range of $300 - 1500$ K. The variation of the ionization degree with the gas temperature is due to expansion of the gas since the steady state electron density remains constant for the temperatures shown in table 2.8. The non-thermal degrees computed with these electron temperatures and densities are shown in figure 2.5. As the gas temperature increases the non-thermal degree declines in a very similar way for all electron temperatures. However, at a very low ionization degree, the rates of vibrational excitation are also very low and for temperatures higher than ~1000 K the VT relaxation completely dominates and $T_V = T$ (see black dots in figure 2.5).

Fig. 2.4. Non-thermal degree, T_V/T, as function of the gas temperature. Computed with the complete vibrational kinetics model for electron densities of 10^{20} (top), 10^{19} (middle), 10^{18} $1/m^3$ (bottom) and electron temperatures of 0.5 (black), 1.0 (blue), 1.5 eV (red). Solid lines cover the range of validity of rate constants in table 2.5. Calculations inside this range of validity were performed in steps of 200 K, whereas steps of 500 K were used for temperatures higher than 1500 K.
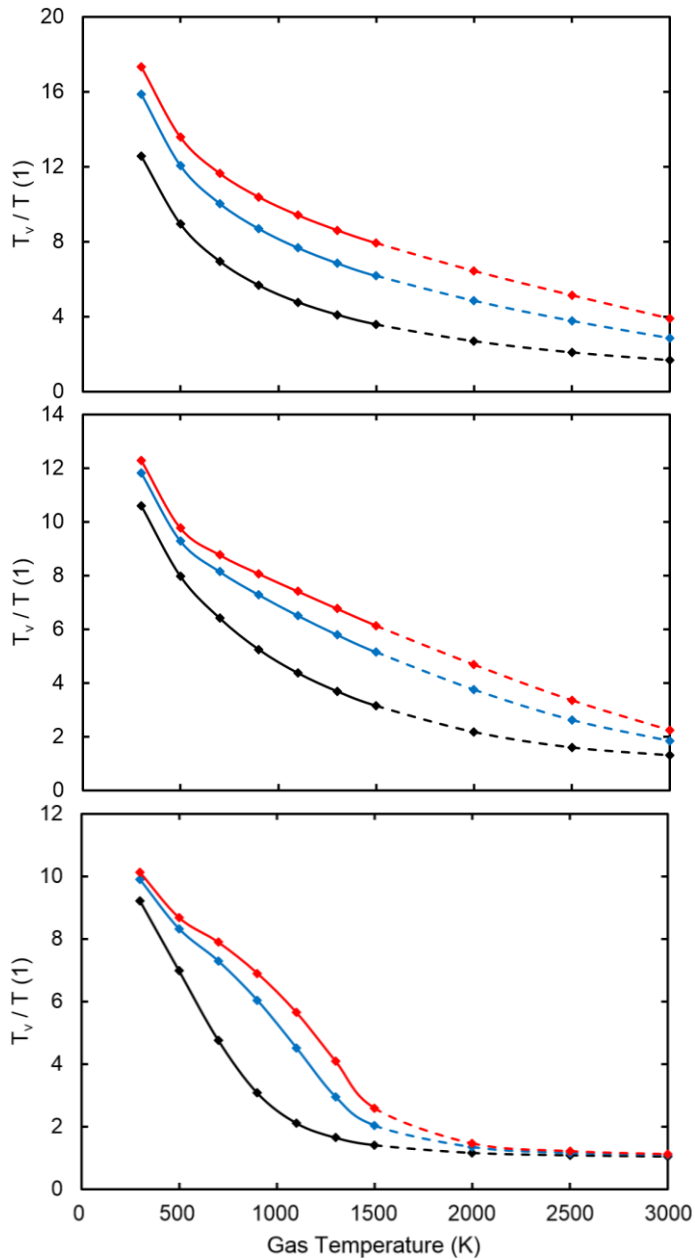
Fig. 2.5. Non-thermal degree, T_V/T, as function of the gas temperature. Computed with the complete vibrational kinetics model for the electron temperatures and corresponding electron densities given in table 2.8: 1.00 (black), 1.25 (blue), 1.50 (red), 1.75 (green) and 2.00 eV (orange). Solid lines for the fitted functions within the range of validity of rate constants in table 2.5, dashed lines for higher temperatures. Calculations inside this range of validity were performed in steps of 200 K, whereas steps of 500 K were used for temperatures higher than 1500 K.
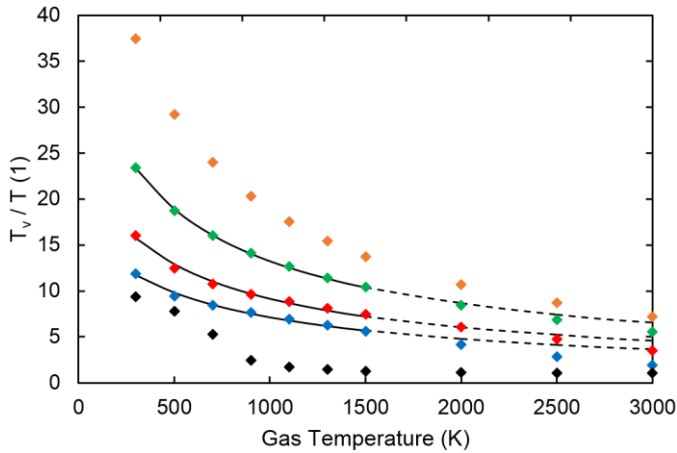
Indeed, at high temperatures, the dots seem to approach the value of 1 at different gas temperatures. However, it is not possible to verify this in the model due to the temperature limitation in the validity of the rate constant expressions. At sufficiently high electron densities, the vibrational excitation and VV relaxation effectively compete against VT relaxation, and therefore the limit at which the non-thermal degree becomes 1 is when thermal equilibrium is reached and $T_e = T = T_V$.

The non-thermal degree data shown in figure 2.5 can be fitted to the following expression with *A* and *B* being fitting parameters [23].

$$T_V/T = \frac{A}{T} \exp\left(\frac{B}{T^{1/3}}\right) \tag{2.4}$$

This expression incorporates the well-known Landau-Teller temperature dependence of VT relaxation, showing the strong influence of the gas temperature in the probability of energy transfer between the translation and vibrational degrees of freedom. This temperature dependence is also seen in the rate constant

31

expressions of vibrational relaxation reactions in table 2.5, although these also include a second order correction term.

Figure 2.5 shows the fitted curves for the electron temperatures and densities resulting in ionization degrees within the typical range of values, i.e. in the order of magnitude between 10^{-6} and 10^{-4} (see table 2.8). The fittings were performed considering only the computed data in the gas temperature range of $300 - 1500$ K and have, in average, an Adjusted R-square higher than 0.99 and a Root Mean Square Error (RMSE) smaller than 0.22. These Goodness-of-Fit statistics are very good and validate equation 2.4 in the lower gas temperature range. At higher temperatures, outside the range of validity of rate constant expressions, the quality of the fitting decays. Nonetheless, the trends remain correct and the fitted curves approximately match the results of the vibrational kinetics model. It is to be noted that equation 2.4 can also describe the behavior of the steady state non-thermal degree when sublevels are not included.

Equation 2.4 has been previously used to approximate the evolution of the temperature ratio T_V/T with increasing gas temperatures [23,25] and dramatically reduce the vibrational kinetics of CO_2 in non-equilibrium microwave plasma. However, the origin of equation 2.4 was not addressed in detail in neither of those works as their purpose were to present a reduction methodology for vibrational kinetics and a two-step modeling approach for plasma reactors.

The reduction methodology is based on the wide difference in the timescales of the processes, especially at low gas temperatures. The characteristic times relation at low gas temperatures is $\tau_{VV} \ll \tau_{eVa} < \tau_{VTs} < \tau_{VTa} \ll \tau_{Diss}$ (see table 2.7 and subsequent discussion), where the characteristic time for CO_2 dissociation is the largest. The calculation of this characteristic time is performed for the first asymmetric vibrational level, assuming that its vibrational energy effectively reduces the energy barrier of the dissociation reaction [10]. Higher vibrational levels dissociate faster and the highest level, which lies in the dissociation limit, dissociates at timescales around ~10^{-10} s. Nevertheless, the formation of high vibrational levels is limited by the electron impact vibrational excitation and slowed down by the competing VT relaxation, which implies that significant dissociation via vibrational excitation can only take place at timescales longer than ~10^{-6} s.

Therefore, in the reduction methodology the processes are divided into the very fast (immediate) VV relaxation and the slower competing processes that take place at longer, but similar timescales. VV relaxation is at least 10^2 times faster than slower processes in the gas temperature range of $300 - 1500$ K (10^3 times at low temperatures, see table 2.7). Equation 2.4 is then used to update the T_V/T ratio at the longer timescales as VT relaxation proceeds and the gas temperature increases.

2.4. Conclusions

We have used a reaction kinetics model to study the vibrational kinetics of CO_2 plasma under the different conditions typically used in CO_2 dissociation experiments in non-thermal microwave plasmas. We showed that Treanor-like vibrational distribution functions can be obtained at low gas temperatures even if VT relaxation is included in the calculations. We also pointed out that symmetric sublevels can play an important role in defining the vibrational distribution function. In fact, at some conditions the vibrational temperature can almost double when VT relaxation of symmetric sublevels is accounted for in the model.

A timescale analysis of the collisional processes based on the first asymmetric vibrational level was performed to get insights into the behavior of the vibrational kinetics. It was found that, in general, VV relaxation is the fastest process and VT relaxation of asymmetric levels is the slowest process throughout the studied conditions. Moreover, it was found that the VT relaxation of symmetric sublevels limits the VV' relaxation process. Likewise, at high temperatures, the VT relaxation of asymmetric levels is hindered by the VT relaxation of symmetric sublevels, particularly the VT relaxation of asymmetric sublevels that proceed through the formation of symmetric sublevels *b* or *c*. Symmetric sublevels are formed in VV' and VT relaxation reactions. Their subsequent VT relaxation takes place in a descending ladder fashion, being the relaxation of the lowest level *a* the slowest step in the process. Therefore, it is concluded that the relaxation of symmetric sublevels slows down the relaxation of asymmetric levels and can lead to Treanor-like vibrational distribution functions and higher vibrational temperatures.

We also showed that, while T_V may increase with the gas temperature, the ratio T_V/T decreases with the gas temperature in the studied range of electron temperature and density values. It was also shown that above certain values of gas

temperature, the VT relaxation is dominant; no vibrational excitation is attained and thus $T_V = T$. At sufficiently high electron densities, the limit at which the ratio T_V/T becomes 1 is when thermal equilibrium is reached and $T_e = T = T_V$.

Furthermore, we demonstrated that the behavior of the ratio T_V/T with increasing gas temperatures can be fitted to an expression that incorporates the Landau-Teller temperature dependence of VT relaxation. The fittings were evaluated by computing the Adjusted R-square and the Root Mean Square Error (RMSE), yielding both very good results in the gas temperature range of $300 - 1500$ K. Within this temperature range, the average Adjusted R-square is higher than 0.99 and the average Root Mean Square Error (RMSE) is smaller than 0.22. It is to be noted however, that at temperatures higher than 1500 K, the quality of the fittings decay, although the trends remain correct and the fitted curves approximately match the results of the vibrational kinetics model. This expression can therefore be used to approximately predict the ratio T_V/T at timescales longer than ~10^{-5} s, as VT relaxation proceeds and the gas temperature increases, particularly for ionization degrees greater than 10^{-6} and gas temperatures lower than ~1500 K.

References

1   V. D. Rusanov, A. a. Fridman and G. V. Sholin, *Uspekhi Fiz. Nauk*, 1981, **134**, 185.

2   W. Bongers, H. Bouwmeester, B. Wolf, F. Peeters, S. Welzel, D. van den Bekerom, N. den Harder, A. Goede, M. Graswinckel, P. W. Groen, J. Kopecki, M. Leins, G. van Rooij, A. Schulz, M. Walker and R. van de Sanden, *Plasma Process. Polym.*, 2017, **14**, 1600126.

3   L. F. Spencer and A. D. Gallimore, *Plasma Sources Sci. Technol.*, 2013, **22**, 015019.

4   B. L. M. Klarenaar, M. Grofulović, A. S. Morillo-Candas, D. C. M. van den Bekerom, M. A. Damen, M. C. M. van de Sanden, O. Guaitella and R. Engeln, *Plasma Sources Sci. Technol.*, 2018, **27**, 045009.

5   T. Silva, N. Britun, T. Godfroid and R. Snyders, *Plasma Sources Sci. Technol.*, 2014, **23**, 025009.

6   T. Silva, N. Britun, T. Godfroid and R. Snyders, *Plasma Process. Polym.*, 2017, **14**, 1600103.

7   A. Vesel, M. Mozetic, A. Drenik and M. Balat-Pichelin, *Chem. Phys.*, 2011, **382**, 127–131.

8   N. den Harder, D. C. M. van den Bekerom, R. S. Al, M. F. Graswinckel, J. M. Palomares, F. J. J. Peeters, S. Ponduri, T. Minea, W. A. Bongers, M. C. M. van de Sanden and G. J. van Rooij, *Plasma Process. Polym.*, 2017, **14**, 1600120.

9   I. Belov, V. Vermeiren, S. Paulussen and A. Bogaerts, *J. CO2 Util.*, 2018, **24**, 386–397.

10   A. Fridman, *Plasma chemistry*, Cambridge University Press, 2008.

11   M. Capitelli, C. M. Ferreira, B. F. Gordiets and A. I. Osipov, *Plasma Kinetics in Atmospheric Gases*, Springer Berlin Heidelberg, Berlin, Heidelberg, 2000, vol. 31.

12   T. Kozák and A. Bogaerts, *Plasma Sources Sci. Technol.*, 2014, **23**, 045004.

13   T. Kozák and A. Bogaerts, *Plasma Sources Sci. Technol.*, 2015, **24**, 015024.

14   P. Diomede, M. C. M. van de Sanden and S. Longo, *J. Phys. Chem. C*, 2017, **121**, 19568–19576.

15   P. Diomede, M. C. M. van de Sanden and S. Longo, *J. Phys. Chem. A*, 2018, **122**, 7918–7923.

16   L. D. Pietanza, G. Colonna and M. Capitelli, *Plasma Sources Sci. Technol.*, 2017, **26**, 125007.

17 L. D. Pietanza, G. Colonna, G. D'Ammando and M. Capitelli, *Plasma Phys. Control. Fusion*, 2017, **59**, 014035.

18 M. Capitelli, G. Colonna, G. D'Ammando and L. D. Pietanza, *Plasma Sources Sci. Technol.*, 2017, **26**, 055009.

19 T. Silva, M. Grofulović, B. L. M. Klarenaar, A. S. Morillo-Candas, O. Guaitella, R. Engeln, C. D. Pintassilgo and V. Guerra, *Plasma Sources Sci. Technol.*, 2018, **27**, 015019.

20 E. V. Kustova and E. A. Nagnibeda, *Chem. Phys.*, 2006, **321**, 293–310.

21 E. V. Kustova and E. A. Nagnibeda, *Chem. Phys.*, 2012, **398**, 111–117.

22 I. Armenise and E. Kustova, *J. Phys. Chem. A*, 2018, **122**, 8709–8721.

23 J. F. de la Fuente, S. H. Moreno, A. I. Stankiewicz and G. D. Stefanidis, *React. Chem. Eng.*, 2016, **1**, 540–554.

24 A. Berthelot and A. Bogaerts, *Plasma Sources Sci. Technol.*, 2016, **25**, 045022.

25 S. H. Moreno, A. I. Stankiewicz and G. D. Stefanidis, *React. Chem. Eng.*, 2019, **4**, 1253–1269.

26 A. Berthelot and A. Bogaerts, *J. Phys. Chem. C*, 2017, **121**, 8236–8251.

27 I. Suzuki, *J. Mol. Spectrosc.*, 1968, **25**, 479–500.

28 M. Grofulović, L. L. Alves and V. Guerra, *J. Phys. D. Appl. Phys.*, 2016, **49**, 395207.

29 *Phelps database, www.lxcat.net, retrieved on January 10*, 2019.

30 J. A. Blauer and G. R. Nickerson, *A survey of vibrational relaxation rate data for processes important to CO2–N2–H2O infrared plume radiation*, Irvine, California, 1973.

31 T. G. Kreutz, J. a O'Neill and G. W. Flynn, *J. Phys. Chem.*, 1987, **91**, 5540–5543.

32 R. D. Sharma, *Phys. Rev.*, 1969, **177**, 102–107.

33 C. E. Treanor, J. W. Rich and R. G. Rehm, *J. Chem. Phys.*, 1968, **48**, 1798–1807.

34 R. E. Beverly, *Opt. Quantum Electron.*, 1982, **14**, 501–513.

3

A NEW METHODOLOGY FOR THE REDUCTION OF VIBRATIONAL KINETICS IN NON-EQUILIBRIUM MICROWAVE PLASMA: APPLICATION TO CO₂ DISSOCIATION

Plasma reactor technologies have the potential to enable storage of green renewable electricity into fuels and chemicals. One of the major challenges for the implementation of these technologies is the energy efficiency. Empirical enhancement of plasma reactors performance has proven to be insufficient in this regard. Numerical models are becoming therefore essential to get insight into the process for optimization purposes. The chemistry in non-thermal plasmas is the most challenging and complex part of the model due to the large number of species and reactions involved. The most recent reaction kinetic model for carbon dioxide (CO₂) dissociation in non-thermal microwave plasma considers more than one hundred species and thousands of reactions. To enable the implementation of this model into multidimensional simulations, a new reduction methodology to simplify the state-to-state kinetic model is presented. It is based on four key elements; 1) all the asymmetric vibrational levels are lumped within a single group, or fictitious species, CO₂*, 2) this group follows a non-equilibrium Treanor distribution, 3) an algebraic approximation is used to compute the vibrational temperature from the translational temperature based on the Landau-Teller formula and 4) weighted algebraic expressions are applied, instead of complex differential equations, to calculate the rates of the most influencing reactions; this decreases substantially the calculation time. Using this new approach, the dissociation and vibrational kinetics are captured in a reduced set of 44 reactions among 13 species. The predictions of the reduced kinetic model regarding the concentrations of the heavy species in the afterglow zone are in good agreement with those of the detailed model from which the former was derived. The methodology may also be applied to other state-to-state kinetic models in which interactions of vibrational levels have the largest share in the global set of reactions.

3.1. Introduction

Two major environmental and scientific challenges faced nowadays are energy storage and greenhouse gas emissions [1–5]. The pressing need in employing renewable energy sources has brought up new challenges regarding electricity storage, which need to be overcome before the current energy mix can be upgraded to one based on renewable energy sources [3]. Various alternatives are being investigated such as mechanical, chemical, electromagnetic and thermal storage [3–6]. The valorisation of carbon dioxide (CO_2) to produce synthetic fuels has been identified as one of the approaches to convert renewable electricity surplus into easy-to-store chemicals [6]. In this regard, plasma-based systems combine the opportunity of utilizing both electricity surplus as well as greenhouse gases, as feedstock, for the conversion process. Plasma reactor technology offers potential benefits, such as compactness, robustness and fast response time to temporal variations at the reactor inlet [7,8]. Therefore, it is a suitable technology to cope with the intermittent and fluctuating pattern of renewable energy supply (e.g., solar and wind energy) [2,9]. Moreover, the characteristics of non-thermal plasma are particularly favorable for the dissociation and utilization of CO_2, making it a very promising technology for chemical process intensification.

One of the major drawbacks to commercialize plasma technology is the high energy consumption [10]. Despite the extensive research conducted experimentally to optimize plasma reactor performance [11,12], there are still a lot of uncertainties that need to be addressed in order to fully understand the reaction mechanisms in non-thermal plasma conditions and optimize plasma processes [13]. Therefore, there is a need to develop reliable plasma chemistries that can be implemented in plasma reactor models for evaluation of different reactor configurations and process optimization [1]. Predictive plasma reactor models are inherently multiphysics models describing electromagnetic wave propagation, mass conservation, electron and fluid dynamics, heat transfer and plasma chemical kinetics [14–16]. When detailed kinetic models, including all the elementary steps, are taken into account, the model becomes highly complex due to the large number of reactions and species needed to describe the plasma reactive system. Large chemical kinetic models require solution of a large number of transport equations in addition to estimating the chemical source terms, often governed by stiff ordinary differential equations (ODEs) [17]. Hence, to enable the applicability of plasma kinetic models in

multidimensional simulations, a simplification approach to reduce complex kinetic models is presented in this work.

Several attempts have been made to develop reaction kinetic models for CO_2 chemistry. In [18], a numerical model for the plasma-chemical reactions taking place in a pure CO_2 glow discharge was developed, albeit vibrational kinetics were not included. In [19], a high temperature non-equilibrium reacting CO_2 flow was studied; although a detailed description of the vibrational kinetics by means of kinetic theory methods was given, the plasma chemistry was missing. More recently, a state-to-state kinetic model including all the relevant chemical reactions in a CO_2 non-thermal microwave discharge was proposed [20]. In a subsequent publication [21], the kinetic model was updated to evaluate the energy efficiency in the discharge. This model consists of 126 species and more than 10000 reactions, including electron impact, neutrals and vibrational energy transfer reactions. In [9], a reduced kinetic model for CO_2 dissociation in dielectric barrier discharges (DBD) was introduced. This model includes the most relevant plasma species and reactions in DBD discharge conditions, but lacks vibrational kinetics. Such a model is then unsuitable for microwave discharges where dissociation through vibrational excitation of the molecule appears to be the most efficient dissociation mechanism [11,22].

Up to date, a practical and manageable kinetic model for CO_2 dissociation in non-thermal microwave plasma has not been reported. In this work, a novel two-step approach for reduction of vibrational kinetics is presented and applied to CO_2 dissociation in non-equilibrium microwave discharges. Two different simplification techniques are coupled to carry out the reduction process: i) chemical lumping of species, where several species are grouped into a single pseudo-species, in combination with ii) a skeletal reduction approach, which includes identification and selection of the most influencing species in the dissociation process without loss of qualitative potential [1,19,23]. The novelty of the presented model lies in four key elements; 1) all the asymmetric vibrational levels are lumped within a single group instead of several groups as reported in [24–26], 2) this group follows the non-equilibrium Treanor distribution, 3) an algebraic approximation is used to compute the vibrational temperature from the translational temperature based on the Landau-Teller formula and 4) weighted algebraic expressions are applied, instead of complex differential equations, to calculate the

rates of the most influencing reactions. The obtained kinetic model comprises 13 species and 44 reactions whereby all the relevant chemical reactions influencing the CO_2 dissociation process are accounted for. The comparison of the results given by the detailed and reduced kinetic models shows good agreement. In particular, the best match is obtained in the afterglow zone, where the species concentrations represent those at the outlet of the reactor. It is important to remark that the purpose of the work is to explore and validate a new methodology for the reduction of vibrational plasma kinetics, exemplified herein for a CO_2 non-thermal microwave discharge, rather than performing self-consistent multidimensional simulations, a task that has not been carried out yet.

3.2. Description of the model

To properly evaluate non-equilibrium reaction kinetics, state-to-state (STS) kinetic models are developed accounting for all the internal excited states and their interactions. This approach leads to reaction mechanisms with a large number of species (in the order of dozens to hundreds) and reactions (in the range of hundreds to thousands), which are not practical for multidimensional simulations. Therefore, the application of STS kinetic models has been mostly limited to zero and one-dimensional simulations. The STS kinetic model reported in [21] was taken as starting point in this work. In the following subsection, a detailed description of the plasma chemical reactive system and also the simplification methodology is given.

3.2.1. Reduced plasma kinetic model: species and reactions

The species considered in the reduced kinetic model are displayed in table 3.1. As stated in [12,27], the CO_2 molecule presents three normal vibrational modes, the symmetric bending mode, the symmetric stretch mode and the asymmetric stretch mode. The symmetric modes of vibration of this molecule are herein denoted as CO_2v_a, CO_2v_b and CO_2v_c (table 3.1). The asymmetric stretch mode is found to be the most energy efficient dissociation channel due to its capacity to store vibrational energy. In this mode, 21 vibrational excited levels are considered up to the dissociation limit of the molecule [20]. The reduction potential of the model is based on the lumping of all the asymmetric vibrational excited levels into a fictitious species, referred to as CO_2^*. This leads to a substantial simplification of the STS kinetic model, as most of the reactions come from the state-to-state interactions of vibrational levels [28].

The reactions included in the reduced kinetic model are shown in tables 3.2, 3, 4 and 5. In this model, four different types of reactions are included; these are electron impact reactions, reactions of neutral species, vibrational energy exchange reactions and surface reactions, which are presented in tables 3.2, 3, 4 and 5, respectively.

Table 3.1. Chemical species included in the reduced kinetic model. CO_2v_a, CO_2v_b and CO_2v_c are the symmetric modes of vibration whereas CO_2* represents a fictitious species accounting for all the asymmetric vibrational levels.

Type	Species
Neutral ground states	CO_2, CO, O, O_2
Vibrationally excited states	CO_2v_a, CO_2v_b, CO_2v_c, CO_2*
Charged species	CO_2^+, CO^+, O_2^+, O^+, e

Electron impact reactions form the driving force of the plasma. The electrons gain kinetic energy from the electromagnetic field, which is further transferred to other species through collisions. The generation of new electrons occurs via ionization reactions, which are responsible for sustaining the plasma.

Table 3.2. Electron impact reactions (RX) considered in the reduced kinetic model.

No	Process	Reaction	Cross section
RX1	CO_2 Elastic scattering	$e + CO_2 \rightarrow e + CO_2$	[29]
RX2	CO_2* Elastic scattering	$e + CO_2* \rightarrow e + CO_2*$	Same as RX1
RX3	CO Elastic scattering	$e + CO \rightarrow e + CO$	[30,31]
RX4	O Elastic scattering	$e + O \rightarrow e + O$	[31]
RX5	O_2 Elastic scattering	$e + O_2 \rightarrow e + O_2$	[32]
RX6	CO_2 Ionization	$e + CO_2 \rightarrow e + e + CO_2^+$	[29]
RX7	CO_2 Ionization from CO_2*	$e + CO_2* \rightarrow e + e + CO_2^+$	Same as RX6
RX8	CO Ionization	$e + CO \rightarrow e + e + CO^+$	[30]
RX9	O Ionization	$e + O \rightarrow e + e + O^+$	[33]
RX10	O_2 Ionization	$e + O_2 \rightarrow e + e + O_2^+$	[32]
RX11	Vibrational (de) excitation to CO_2v_a	$e + CO_2 \leftrightarrow e + CO_2v_a$	[29]
RX12	Vibrational (de) excitation to CO_2v_b	$e + CO_2 \leftrightarrow e + CO_2 v_b$	[29]
RX13	Vibrational (de) excitation to CO_2*	$e + CO_2 \leftrightarrow e + CO_2*$	See section 3.2.2

Reactions of neutral species play an important role in the formation of reactive species to promote chemical reactions. At favorable dissociation conditions, a fraction of the energy transferred from the electrons to the CO_2 molecule is stored as internal energy in high vibrational levels of the asymmetric mode, which can either facilitate its dissociation or be transferred to the bulk gas as heat.

Table 3.3. Reactions of neutrals (RN) included in the model. $M = CO_2$, CO or O_2. Gas temperature (T_g) in K and rate constants in cm^3/s and cm^6/s for binary and ternary reactions, respectively.

No	Process/Reaction	Rate constant
RN1	CO_2^* Dissociation by collisions with CO_2, CO and O_2 $CO_2^* + M \rightarrow CO + O + M$	$9.59 \times 10^{-16} (T_g/300)^{2.92} \exp(639/T_g)$
RN2	CO_2^* Dissociation by collisions with O $CO_2^* + O \rightarrow CO + O_2$	$3.35 \times 10^{-14} (T_g/300)^{1.47} \exp(-271/T_g)$
RN3	Three-body CO and O recombination $CO + O + M \rightarrow CO_2 + M$	$8.2 \times 10^{-34} \exp(-1510/T_g)$
RN4	Two-body CO and O_2 recombination $CO + O_2 \rightarrow CO_2 + O$	$1.23 \times 10^{-12} \exp(-12800/T_g)$
RN5	Three-body O recombination $O + O + M \rightarrow O_2 + M$	$1.27 \times 10^{-32} (T_g/300)^{-1} \exp(-170/T_g)$

Vibrational energy transfer reactions are responsible for the energy exchange between vibrationally excited molecules and the vibrational energy loss to ground state molecules. In this model, these reactions mainly lead to generation of heat by transferring the energy to the bulk gas via vibrational-translational (VT) relaxation reactions. Note that the parameters ν_{s2} and ν_{s3} represent the stoichiometric coefficients of the symmetric excited states for reactions RV2 and RV3, whereas ν_{l2} and ν_{l3} indicate the stoichiometric coefficients of the lumped excited state for the same reactions (RV2 and RV3).

Table 3.4. Vibrational energy transfer reactions (RV) considered in the model. $M = CO_2$, CO or O_2. Gas temperature (T_g) in K. ν_{s2}, ν_{s3}, ν_{l2} and ν_{l3} represent the stoichiometric coefficients of the symmetric excited states (s) and the lumped excited state (l), respectively, for the reactions RV2 and RV3.

No	Process/Reaction	Rate constant
RV1	VT Relaxation of symmetric vibrationally excited states x = a,b,c	
	$CO_2v_x + M \rightarrow CO_2 + M$	$7.14 \times 10^{-8} \exp(-177T_g^{-1/3} + 451T_g^{-2/3})$
	$M = CO_2$	x 1
	$M = CO, O_2$	x 0.7
RV2	VT Relaxation of the lumped asymmetric vibrationally excited state	
	$CO_2^* + M \rightarrow \nu_{l2} CO_2^* + \nu_{s2} (CO_2v_a + CO_2v_b + CO_2v_c) + M$	
	$M = CO_2$	$4.72 \times 10^{-17} (T_g/300)^{6.55} \exp(1289/T_g)$
	$M = CO$	$1.47 \times 10^{-17} (T_g/300)^{6.53} \exp(1282/T_g)$
	$M = O_2$	$1.95 \times 10^{-17} (T_g/300)^{6.53} \exp(1282/T_g)$
RV3	VV' Relaxation between symmetric and asymmetric vibrationally excited states	
	$CO_2^* + CO_2 \rightarrow \nu_{l3} CO_2^* + \nu_{s3} (CO_2v_a + CO_2v_b)$	$3.99 \times 10^{-15} (T_g/300)^{4.46} \exp(398/T_g)$

The charged species, electrons and ions, diffuse together toward the walls by the effect of ambipolar diffusion, where electrons and ions are recombined via collisions on the reactor wall.

Table 3.5. Surface reactions (RS) included in the reduced kinetic model.

No	Process	Reaction	Sticking coefficient (γ)
RS1	CO_2^+ Neutralization	$CO_2^+ \rightarrow CO_2$	1
RS2	CO^+ Neutralization	$CO^+ \rightarrow CO$	1
RS3	O^+ Neutralization	$O^+ \rightarrow O$	1
RS4	O_2^+ Neutralization	$O_2^+ \rightarrow O_2$	1

Using the simplification approach, which is described in the following sections, the STS model has been significantly reduced to 44 reactions among 13 species accounting for the most relevant processes that dominate the dissociation of CO_2 in non-equilibrium microwave plasma. A schematic representation of the reaction pathway is presented in figure 3.1.
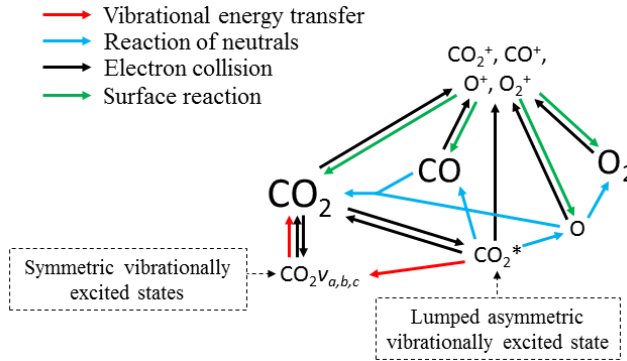

Fig. 3.1. Reaction pathway of the reduced kinetic model.

3.2.2. Simplification approach

Up to date, various approaches have been adopted to reduce STS kinetic models. For instance, in [28], the Principal Component Analysis (PCA) is applied to the CO_2 dissociation process driven by vibrational kinetics; in this approach, a large database of results obtained with the STS kinetic model is required to identify the principal components. One can also make use of commercially available software, such as CHEMKIN-PRO [34], which is mainly used for combustion processes, and PumpKin [35], which employs algorithms to identify key components and group

large set of reactions in reduced reaction pathways; the latter is mostly used in plasma chemical models. The approaches in [36] and [37] are closer to the one presented here; specifically, the kinetics are described by the vibrational and translational temperatures for the dissociation and recombination regimes of $N_2 + N$ in non-equilibrium hypersonic flows. Approaches where internal modes of molecules are divided into several groups have been reported as well [24–26]. Such a multigroup lumping method was recently applied to reduce the vibrational kinetics of CO_2 [38]. In this method, the vibrational levels of the asymmetric mode are lumped into various groups, each characterized by an internal Boltzmann equilibrium distribution given by its own vibrational temperature.

In this work, a new reduction approach is introduced to simplify the STS kinetic model proposed in [21] for the dissociation of CO_2 in non-equilibrium microwave discharges. As opposed to [24–26], our approach is based on lumping all the asymmetric vibrational levels within a single group. In addition, a non-equilibrium distribution, the so-called Treanor distribution, is considered in the lumping process instead of the commonly used Boltzmann distribution. It is known that the Treanor distribution overestimates the population of high energy levels, yet, this is balanced by the high VT and VV' rates obtained for the group (see Simplification approach section). The complexity of multi-temperature approaches, widely used up to now, is reduced by the introduction of an algebraic approximation linking the vibrational and translational temperatures. Another advantage of this methodology is the implementation of weighted algebraic expressions to compute rate constants, instead of solving the complex differential equations used in [24–26], thereby enabling a faster calculation of the reaction rates. The application of this technique results in significant simplification regarding the number of reactions and species to describe the dissociation of CO_2. Few methods have succeeded in the reduction of detailed plasma kinetic models, which concern mainly diatomic molecules. In the case of more complex molecules, the development of practical and manageable approaches is subject to ongoing research in order to enable multidimensional modeling of non-equilibrium plasma processes.

As stated before, the main reduction in the presented approach is achieved by grouping the asymmetric vibrationally excited states of CO_2, which represent the main dissociation channel of the molecule in this type of discharges. Hence, the 21 vibrational levels considered in the detailed kinetic model [21] to describe the

dissociation processes are lumped into a single asymmetric vibrational excited state. The fictitious species (CO_2^*) is the representation of all asymmetric vibrational excited states that are not in thermal equilibrium with the translational energy mode of the molecule. An illustration of the lumped species is outlined in figure 3.2.
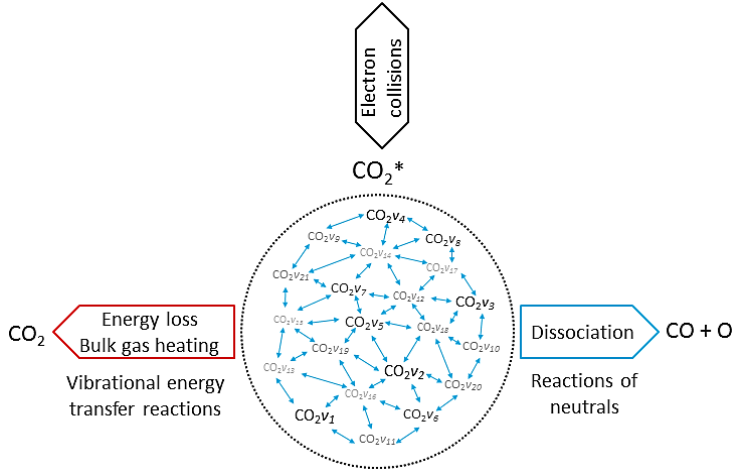

Fig. 3.2. Lumping of 21 asymmetric vibrational levels into a fictitious species CO_2^*.

High CO_2 dissociation rates can be attained when the high vibrational levels of CO_2 remain far from equilibrium [21]. In low temperature plasmas, the highest relaxation rate is the (vibrational-vibrational) VV relaxation, i.e. the interaction of CO_2 molecules that are excited in the same vibrational mode. When the temperature of the gas increases, the (vibrational-translational) VT relaxation rate is boosted, thus leading to a high energy loss by heating up the gas. It is assumed that the vibrational levels lumped into the fictitious species CO_2^* solely exchange energy through VV relaxation. Although, as a group, they can either dissociate or lose energy via VT relaxation as shown in figure 3.2. One of the major assumptions taken in the presented model is that the excited states follow the so-called Treanor non-equilibrium distribution [39], which allows for the calculation of the population densities of all asymmetric vibrationally excited states. The reason behind this assumption is the dominant vibrational energy transfer mechanism in the discharge: electron impact vibrational excitation (0→1) followed by VV relaxation. Hence, the energy used in the dissociation is mainly transferred through this mechanism, which also results in a Treanor vibrational distribution. For simplicity, a good approximation is to fit their energy levels to a diatomic anharmonic oscillator

model and compute an effective anharmonicity coefficient so that the Treanor distribution can be calculated. The Treanor distribution enables the evaluation of the departure from thermal equilibrium given by the Boltzmann distribution. Figure 3.3 shows this concept more in detail by plotting the vibrational distribution functions considering different approaches: 1) Boltzmann distribution, 2) STS kinetic model [20] (microwave discharge, power density = 25 W cm^{-3} and 0.8 ms time) and 3) Treanor distribution. The T_v/T_g value shown in figure 3.3 do not correspond to the values used to carry out the validation of the model, instead it shows the qualitative difference of the various VDF's. At low T_v/T_g values, the Treanor distribution approaches the Boltzmann distribution (becoming equal when $T_v/T_g = 1$), whereas at high T_v/T_g values the highly non-equilibrium nature of the discharge is noticeable. The departure from thermal equilibrium observed for both the STS and Treanor vibrational distributions represents the stored vibrational energy in the asymmetric mode. In comparison to the Treanor distribution the high levels of the STS distribution are depleted due to VT relaxation and dissociation. Herein, the overpopulation of the Treanor distribution is used to compute effective rates for vibrational relaxation and dissociation.
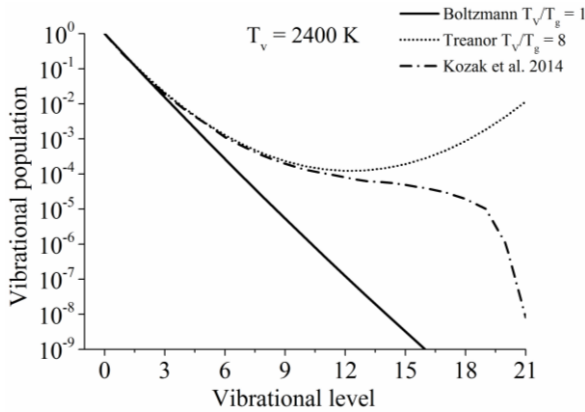

Fig. 3.3. Comparison of the vibrational distributions functions considering the approaches: 1) Boltzmann distribution, 2) STS kinetic model [20] (microwave discharge, power density = 25 W cm^{-3}) and 0.8 ms time) and 3) Treanor distribution.

The vibrational and bulk gas temperatures (T_v and T_g) are required to calculate the Treanor distribution, which reads [39]

$$n_v = n_0 \exp\left(-\frac{vE_1}{T_v} + \frac{vE_1 - E_v}{T_g} \right)$$

(3.1)

where n_v is the population density and E_v the energy in eV of the vibrational level v, n_0 is the population density of the CO_2 ground state and T_g and T_v are the bulk gas and the vibrational temperatures (both in eV), respectively. The vibrational temperature in the previous equation is based on the population density of the first vibrational level and it is computed as follows.

$$T_v = \frac{E_1}{\ln\left(\frac{n_0}{n_1}\right)} \tag{3.2}$$

The discharge can be characterized by the T_v/T_g ratio, which should be high enough at low bulk gas temperatures to achieve efficient dissociation. For multidimensional models this mean or characteristic value of the discharge could be used for the calculations, instead of considering spatial variations of the T_v/T_g values throughout the discharge. Considering the conditions studied in [21], T_v/T_g values lie in the range of 5.2 to 7. A sensitivity analysis carried out to study the effect of this value on the kinetics yielded the best agreement with a value of 6 (see Validation of the model section). On the other hand, at temperatures beyond the characteristic vibrational temperature, the VT and VV relaxation processes become comparable, even for the lowest vibrational levels [39]. In this case, the non-thermal effect is not attained and the discharge is completely thermalized, $T_v/T_g=1$. The conditions at which a plasma reaches thermal equilibrium vary depending on the type and duration of the discharge. Since it is rather complex to determine when a microwave plasma reaches thermal equilibrium (between 4000 to 5000 K [12]), a value of 5070 K is assumed. This temperature is 1.5 times the characteristic vibrational temperature of CO_2 and is above 5000 K, which ensures thermal equilibrium conditions of the plasma (dominance of VT over VV relaxation). Moreover, as found in [40], the gas temperature in a pure CO_2 microwave plasma torch is about 5000 K, which is consistent with our assumption. For further clarification, a comparison of the influence of these two parameters is given in the subsequent section, in which it is shown that the gas temperature at which quasi-equilibrium plasma conditions are reached barely has any influence on the results, while the high T_v/T_g value affects the calculations to a higher degree. The accuracy of the values chosen to compute the Treanor distribution is of secondary importance for the scope of this work, which is to demonstrate the validity of the reduction methodology.

Another point of discussion is the shape of the curve to estimate the T_v/T_g ratio. An exponential dependence is proposed as an initial approximation based on the Landau-Teller temperature dependence of vibrational-translational relaxation (VT), which becomes more relevant as temperature increases. Besides, a simple expression is preferred so that only two points are required for the fitting (see figure 3.4). For the considered range of temperatures the following expression gives a reasonable agreement of the temperature dependence with STS calculations of CO_2 vibrational kinetics.

$$T_v/T_g = a \exp\left(\frac{b}{T_g^{1/3}}\right) \times \frac{1}{T_g} = 10937 \exp\left(\frac{-12.05}{T_g^{1/3}}\right) \times \frac{1}{T_g} \qquad (3.3)$$

An accurate description of T_v and T_g would require the full set of reactions, which is not practical, or even possible, for multidimensional simulations. The coefficients a and b were computed by fitting this function to the proposed values of T_v/T_g. By following this approach, the Treanor distribution becomes exclusively a function of the gas temperature, thereby facilitating the calculation of the distribution. The Treanor distribution at various gas temperatures enables the estimation of rate constants for reactions involving the fictitious species CO_2^*. These parameters are obtained by adding the individual contributions of the vibrational levels, which are computed from their populations and individual rate constants.
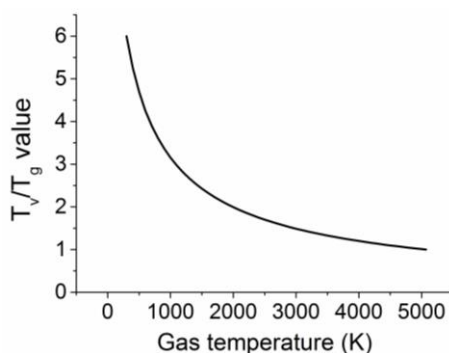

Fig. 3.4. T_v/T_g ratio-gas temperature dependence according to equation 3.3.

3.2.2.1. Electron impact reactions

One of the major simplifications in the reduced kinetic model is accomplished by assuming a Maxwellian electron energy distribution function (EEDF). This approximation is commonly accepted for typical microwave discharges as shown in [41], where a comparison between Maxwellian and non-equilibrium EEDFs is carried out. The studied microwave discharges present typical electron temperature values in the range 0.5 to 2 eV, in which the Maxwellian EEDF is rather similar to the non-equilibrium EEDF. Nevertheless, careful consideration should be given to this assumption, as reported in [42], where it was shown that non-equilibrium distributions can present an overpopulation in the tail, i.e. at high electron energies, as compared to a Maxwellian EEDF. These overpopulated tails are caused by superelastic collisions with electronically excited states and can influence high-threshold electron impact processes, resulting in increase in their reaction rates.

At low electron energies, the highest reaction rates are expected for elastic scattering and vibrational excitation since these reactions show the largest collisional cross sections [43]. On the other hand, at high electron energies, the EEDF is considerably smaller, meaning that the rate constants are orders of magnitude smaller than processes taking place at low energies. For instance, for an electron temperature of 2 eV, the rate coefficient of the electron impact CO_2 dissociation, which takes place at relatively high electron energies, is 3 orders of magnitude smaller than the rate coefficient of vibrational excitation. Therefore, only reactions with large cross sections are considered in the high electron energy range. In particular, besides elastic scattering, the largest cross section and the lowest energy threshold is attributed to the single charge ionization of CO_2 [29]. In fact, the ionization rate due to single charge ionization is at least two orders of magnitude larger than other ionization processes, such as dissociative ionization or multiple charge ionization. In conclusion, three types of collision processes (elastic scattering, vibrational excitation and non-dissociative single charge ionization) are taken into account for the reduced kinetic model.

Concerning collisions of electrons with the main neutral products of CO_2, i.e. CO, O, O_2 and O_3, these species take part in important processes of the reactive system, thus displaying high population densities. Based on the results given in [21], the population density of O_3 is at least two orders of magnitude less than that of O_2 and three orders of magnitude less than the one of CO_2. Moreover, O_3 is mainly a

product formed in the afterglow and does not have a major influence on the dissociation kinetics of CO_2. For this reason, the O_3 species is not included in the model. By analyzing the cross section data reported [30–33,43,44], it can be concluded that the same type of reactions (elastic scattering, vibrational excitation and ionization) should be considered for the neutral species.

It is noted that the electronic excitation process has been neglected for neutral species in the reduced kinetic model, as it barely influences the CO_2 dissociation kinetics at low electron energies. Furthermore, assuming quasi-neutrality of plasma and an ionization degree of about 10^{-5}, [21] the mass fractions of the charged species are ~5 orders of magnitude lower than the neutrals. Therefore, reactions with charged species are not included in the model.

With regard to electron collisions with vibrationally excited species, vibrational excitation reactions are considered for CO_2 and neglected for other neutrals as the energy transfer to vibrational modes of these species is considerably lower [21]. While the symmetric vibrational modes of CO_2, CO_2v_a and CO_2v_b, in combination with the lumped asymmetric vibrational mode CO_2^*, are included, higher symmetric levels, such as the CO_2v_c and CO_2v_d are not added, as the cross sections for multiquantum vibrational jumps are smaller than single quantum vibrational jumps. Reverse processes of vibrational excitation, called de-excitation reactions, are also included in the model by using the detailed balancing principle [45].

The black arrows in figure 3.1 show the electron impact reactions included in the reduced kinetic model. A total of 16 electron impact reactions are included; we refer to table 3.2 for more information.

Cross section calculation for vibrational excitation from CO_2 to CO_2^*

An overall vibrational excitation cross section is computed by lumping the vibrational excitation processes in the asymmetric vibrational mode, from the CO_2 ground state to the higher states within CO_2^*. Vibrational de-excitation cross sections are obtained from the overall cross section by applying the detailed balancing principle. The calculation is carried out by scaling the cross sections using the Fridman's approximation. Then, the computed cross sections are added to estimate the overall cross section. The total electron impact vibrational excitation

rate for CO_2 is the sum of the vibrational excitation rates from level 0 to all higher levels, thus

$$n_0 n_e \sum_{j=1}^{21} k_{0,j} = n_0 n_e \gamma \int_0^\infty \varepsilon \sigma_V(\varepsilon) f(\varepsilon) d\varepsilon \tag{3.4}$$

where n_0 is the population density of the vibrational level 0 (CO_2); n_e is the population density of electrons; $k_{0,j}$ is the rate coefficient for the vibrational excitation from level 0 to level j; ε is the electron energy; $\sigma_{0,j}(\varepsilon)$ is the cross section for the vibrational excitation from level 0 to level j; $f(\varepsilon)$ is the electron energy distribution; γ is a conversion units constant and $\sigma_V(\varepsilon)$ is the cross section for the excitation of CO_2 to CO_2* (reaction RX13 in table 3.2) and is computed as follows.

$$\sigma_V(\varepsilon) = \sum_{j=1}^{21} \sigma_{0,j}(\varepsilon) \tag{3.5}$$

Not all the cross sections for the transitions from any level i to a higher level j are available. Hence, they are computed using the Fridman's approximation [12]. Specifically, the cross section of the lowest transition, from level 0 to level 1 ($\sigma_{0,1}$), is scaled to higher transitions by applying the following expression

$$\sigma_{i,j}\left(\varepsilon + E_{i,j} - E_{0,1}\right) = \sigma_{0,1}(\varepsilon)\, exp\left(\frac{-\alpha(j - i - 1)}{1 + \beta i}\right) \tag{3.6}$$

where $E_{i,j} = E_j - E_i$ is the energy difference between levels j and i and α and β are scaling factors. For the specific case of CO_2, the α factor takes the value of 0.5 and the β factor is assumed to be 0 [12,20]. This approximation is used to compute all the transitions from level 0, which are subsequently added to obtain σ_v. The cross section's magnitude increases as a consequence of adding the cross sections of multiquantum vibrational jumps, while the discrete energy levels explain the presence of multiple peaks. The values of $\sigma_{0,1}$ used in the calculations are taken from [29].

In figure 3.5, a comparison between the cross section for the transition from level 0 to level 1 and the cross section for the excitation from CO_2 to CO_2^* is presented. The energy threshold of the process is the minimum energy required to put a CO_2 molecule into vibration, which in this case is $E_1 - E_0 = 0.29$ eV.
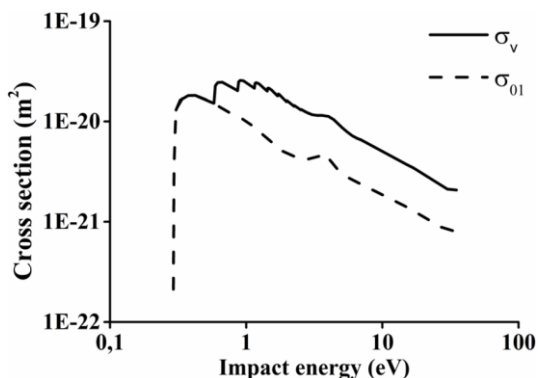

Fig. 3.5. Cross section for the vibrational excitation from CO_2 to CO_2^*.

3.2.2.2. Reactions of neutral species

As mentioned in the previous section, a large portion of the energy is transferred from the electrons to the vibrational modes of the CO_2 molecule. Once the asymmetric mode is energized, the stored vibrational energy can be utilized to dissociate the molecule. A total of 11 dissociation and recombination reactions with neutrals are included in the reduced kinetic model (see blue arrows in figure 3.1 and table 3.3). When compared to the STS kinetic model, three neutrals species (C, C_2O and O_3) are disregarded. The reason to neglect these species is the low net production rates and therefore the very low population densities (5 orders of magnitude smaller than CO_2) displayed in the overall reaction scheme. Moreover, these species show a minor influence on the dissociation kinetics. The reactions of neutral species are then restricted to the ones involving CO_2, CO, O and O_2.

In figure 3.1, it can be observed that the lumped excited species CO_2^* is considered in the dissociation processes as dissociation reactions involving CO_2 ground state (v = 0) present the highest activation energies leading to very low reaction rates.

Due to the change in the activation energy of the dissociation reactions, as a consequence of the stored vibrational energy, the rate constants of reactions RN1 and RN2 must be computed. To estimate the efficiency in the reduction of the

activation energy due to vibrational excitation, the Fridman-Macheret α-model is applied [12]. The following expression is used [46]

$$k_v(E_v, T_g) = A \exp\left(-\frac{E_a - \alpha E_V}{T_g}\right) \tag{3.7}$$

where A is the conventional pre-exponential factor, E_a is the activation energy of the reaction in K, E_v is the vibrational energy of level v in K (energy levels given in [20]), T_g is the bulk gas temperature in K and α is the efficiency of the vibrational energy in reducing the activation energy. The α values for RN1 (α = 1) and RN2 (α = 0.5) are taken from [20].

The rate constants of each level are then multiplied by the population densities obtained from the Treanor distribution. For the dissociation reaction RN1, the following equation is aplied [37].

$$k(T_g) = \sum_{v=1}^{21} n_v(T_g) k_v(E_v, T_g) \tag{3.8}$$

For the dissociation reaction RN2, a different expression is used. RN1 is an endothermic reaction with a high activation energy, which virtually vanishes at the highest vibrational levels, whereas RN2 is a thermoneutral reaction with an activation energy that vanishes at vibrational levels above v = 10. Hence, the form of the rate constant is divided into two groups: 1) vibrational levels from 1 to 10 and 2) levels from 11 to 21. We propose the following expression to compute the rate constant for RN2

$$\ln k(T_g) = \frac{v_1}{v_2} \ln k_1(T_g) + \frac{v_2 - v_1}{v_2} \ln k_2 \tag{3.9}$$

where v_1 is the number of levels in the first group and v_2 the total number of levels; k_1 is the averaged rate constant of the first group and k_2 the one of the second group. Lastly, the averaged rate constant is estimated by adding the individual contributions of the lumped vibrational levels (v = 1 − 21). This process is repeated at various temperatures within the range of interest, 300 − 1500 K. Note that the validity of the rate constant expressions considered for the vibrational energy

exchange reactions lies in the range 300 to 1500 K [47], which hinders the evaluation of this model at higher gas temperatures.

In figure 3.6, the calculated rate constants for the reactions RN1 and RN2 at different temperatures are displayed. These values are then fitted to a modified Arrhenius type of equation so that a single temperature-dependent expression for the CO_2* dissociation reactions can be implemented (table 3.3, RN1 and RN2 rate constants).
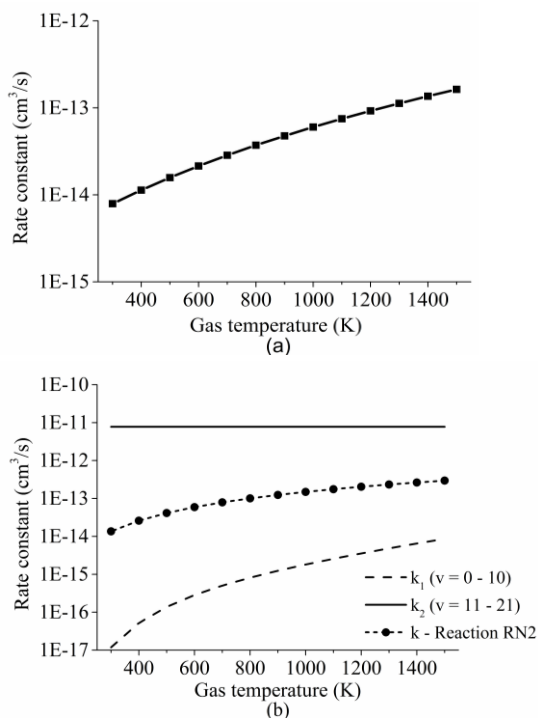

Fig. 3.6. (a) Rate constant of reaction RN1 as function of gas temperature and (b) rate constant of reaction RN2 as function of gas temperature (k_1 and k_2 are shown for reference).

3.2.2.3. Vibrational energy transfer reactions

The outcome of these energy exchange processes is mainly related to energy loss from vibrationally excited states to the bulk gas. Two types of relaxation reactions are considered, VT and VV' relaxation. In the VT type, vibrational and translational degrees of freedom exchange energy in which either a symmetric vibrationally excited state loses its energy in a collision with a neutral ground state

(RV1) or the lumped asymmetric excited state transfers a fraction of its vibrational energy to the symmetric vibrational modes $CO_2v_{a,b,c}$(RV2). The VV' relaxation process (RV3) comprises the energy exchange due to collisions between the lumped excited state CO_2^* and a CO_2 ground state, thus transferring a portion of its vibrational energy to the symmetric modes of the molecule. A total of 13 vibrational energy exchange reactions are included in the reduced kinetic model (red arrows in figure 3.1 and table 3.4). The following subsections describe how the rate constants for the reactions RV2 and RV3 are calculated. The energy change in the reactions is fitted to diatomic anharmonic oscillator models so that the anharmonicity coefficient can be computed to scale the rate constants from the lowest vibrational state to higher ones at specific gas temperatures [20]. The approach to calculate these rates is rather similar to the one used for the reaction of neutrals with one difference; the stoichiometric coefficients also depend on the Treanor distribution, which then depends on the bulk gas temperature.

Rate constant for reaction RV2

The initial step is to compute the rate constants of the VT relaxation reactions for all the asymmetric vibrational levels within CO_2^*. In these reactions, a purely asymmetric vibrational level v relaxes into a lower asymmetric level v – 1 with a symmetric sublevel a,b,c. It is assumed that symmetric sublevels relax rapidly via VT relaxation, thus becoming in thermal equilibrium with the asymmetric level. This mechanism is not a direct process and consists of multiple VT relaxation reactions, in which the first process is considered to be the rate limiting step [48].

$$\left.\begin{array}{l} CO_2(0\ 0\ v) + M \rightarrow CO_2(0\ 1\ v-1) + M \\ \rightarrow CO_2(0\ 2\ v-1) + M \\ \rightarrow CO_2(0\ 3\ v-1) + M \end{array}\right\} \xrightarrow{VT\ Relaxation} CO_2(0\ 0\ v-1) + M \quad \left.\begin{array}{l}(V2a, Ref.[20]) \\ (V2b, Ref.[20]) \\ (V2c, Ref.[20])\end{array}\right] \quad (3.10)$$
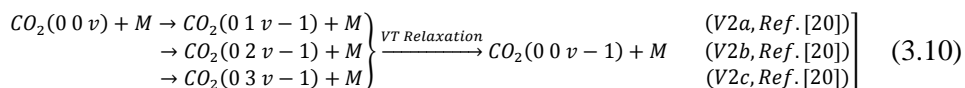
The rate constants are scaled by using expressions derived from the SSH theory [49,50]. The scaling of the reaction rates is carried out by fitting the energy change in the reaction to a diatomic anharmonic oscillator model. The rate constants of reactions involving higher vibrational levels v > 1 are estimated from the rate constant of the reaction corresponding to the lowest levels (from v = 1 to v = 0). The calculation procedure for scaling the reactions is adapted from [20].
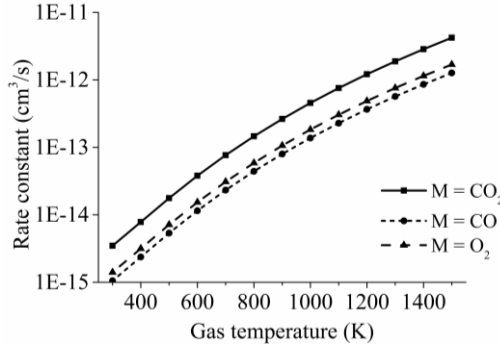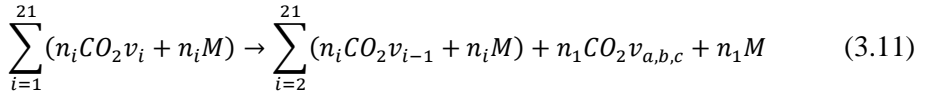
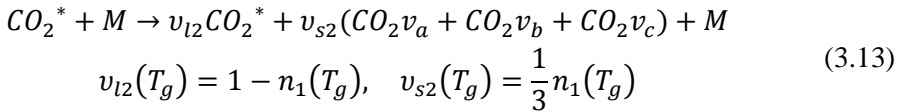**Fig. 3.7.** Rate constant of reaction RV2 as function of gas temperature for M = CO$_2$, CO and O$_2$.

The reactions V2a,b,c [21] of all asymmetric vibrational levels within CO$_2$ are multiplied by the corresponding Treanor population and added to obtain three reactions per collision partner M

$$\sum_{i=1}^{21}(n_i CO_2 v_i + n_i M) \rightarrow \sum_{i=2}^{21}(n_i CO_2 v_{i-1} + n_i M) + n_1 CO_2 v_{a,b,c} + n_1 M \qquad (3.11)$$

by introducing the fictitious species CO$_2$* they can be simplified to

$$CO_2{}^* + M \rightarrow (1 - n_1)CO_2{}^* + n_1 CO_2 v_{a,b,c} + M \qquad (3.12)$$

For a specific collision partner M it is possible to express these reactions in a more general "lumped" expression, which is more convenient for implementation into the model
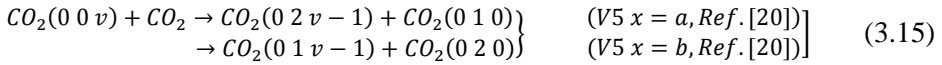
$$CO_2{}^* + M \rightarrow v_{l2}CO_2{}^* + v_{s2}(CO_2 v_a + CO_2 v_b + CO_2 v_c) + M$$
$$v_{l2}(T_g) = 1 - n_1(T_g), \quad v_{s2}(T_g) = \frac{1}{3}n_1(T_g) \qquad (3.13)$$

where v_{l2} and v_{s2} are the stoichiometric coefficients of the lumped excited state and the symmetric levels a,b,c respectively. The coefficients are function of the population density of the first asymmetric vibrational level n_1, which is computed with the Treanor distribution at a specific gas temperature T_g. The total averaged rate constant of the reaction RV2 (see table 3.4) for a specific collision partner M is estimated by adding the averaged rate constants of the three individual reactions.

$$k_M(T_g) = k_{M,a}(T_g) + k_{M,b}(T_g) + k_{M,c}(T_g) \qquad (3.14)$$

The averaged rate constant of each reaction is computed as in equation 3.8, considering that the individual rate constants k_v are scaled to the asymmetric vibrational level v, and depend on the symmetric sublevel and the collision partner M. For each collision partner M, the temperature range of interest (300 - 1500 K) is evaluated as shown in figure 3.7. For each of the reactions with different collision partners, the rate constant is fitted to a modified Arrhenius equation with the aim of using a more practical expression in the model.
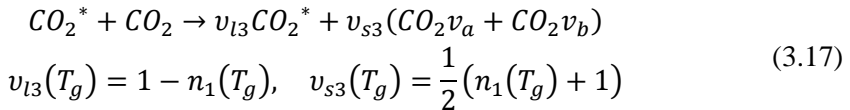
Rate constant for reaction RV3

The calculation process is similar to the one presented above for RV2. In this case, the energy is transferred between different vibrational modes, i.e. the asymmetric and the first two symmetric modes (a, b). The reaction scheme is represented as

$$
\begin{aligned}
CO_2(0\,0\,v) + CO_2 &\rightarrow CO_2(0\,2\,v-1) + CO_2(0\,1\,0)) \qquad (V5\ x = a, Ref.[20]) \\
&\rightarrow CO_2(0\,1\,v-1) + CO_2(0\,2\,0)) \qquad (V5\ x = b, Ref.[20])
\end{aligned} \qquad (3.15)
$$

Assuming a rapid VT relaxation of the symmetric sublevels and adding the reactions of all asymmetric levels within CO_2*, the following expression is obtained for V5 x = a.

$$
\sum_{i=1}^{21}(n_i CO_2 v_i + n_i CO_2) \rightarrow \sum_{i=2}^{21}(n_i CO_2 v_{i-1} + n_i CO_2 v_a) + n_1 CO_2 v_b + n_1 CO_2 v_a \qquad (3.16)
$$

The reaction RV3 included in the model is a result of combining the previous reaction with the analogous reaction V5 for the symmetric level b. Once the two combined reactions are put together, RV3 can be written as

$$
CO_2* + CO_2 \rightarrow v_{l3} CO_2* + v_{s3}(CO_2 v_a + CO_2 v_b)
$$
$$
v_{l3}(T_g) = 1 - n_1(T_g), \quad v_{s3}(T_g) = \frac{1}{2}(n_1(T_g) + 1) \qquad (3.17)
$$

The stoichiometric coefficients v_{l3} and v_{s3} are computed as done in the previous section for RV2. The total averaged rate constant of reaction RV3 is estimated by adding the individual averaged rate constants of both reactions.

$$
k(T_g) = k_a(T_g) + k_b(T_g) \qquad (3.18)
$$

The averaged rate constant of each reaction is computed as in equation 3.8, considering that the individual rate constants k_v are scaled to the asymmetric vibrational level v and depend on the symmetric sublevel.

The overall "lumped" rate constant calculated at various temperatures is fitted to a modified Arrhenius equation to obtain a temperature-dependent expression (see table 3.4). The results of the rate constant obtained at various temperatures are displayed in figure 3.8.
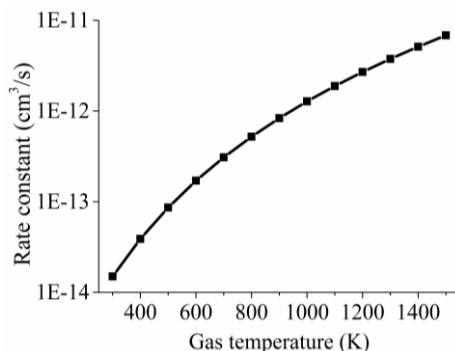

Fig. 3.8. Rate constant of reaction RV3 as function of gas temperature.

3.2.2.4. Surface reactions

This type of reactions take place on the surface of the reactor when chemical species collide with the surface. The rate coefficients for a single species can be determined by the following expression [51]

$$k_s = \left(\frac{1}{1-\gamma/2}\right)\frac{\gamma}{(\Gamma_{tot})^s}\left(\frac{1}{4}\right)\left(\frac{8k_B T_g}{\pi m}\right)^{\frac{1}{2}} \tag{3.19}$$

where γ is the sticking coefficient of the reaction, i.e. the probability that the collision results in a reaction. Γ_{tot} is the total surface site density $[1/m^2]$ and the exponent s is the sum of the stoichiometric coefficients of the surface reactants. The square root term is the mean thermal speed of the colliding species, computed from the Boltzmann constant K_B, the bulk gas temperature T_g and the mass of the species m. It is noted that the first term within the brackets is the Motz-Wise

correction, which is only included when the sticking coefficient is large, i.e. close to 1 [51].

Various surface reactions can occur in the reactor, such as recombination or vibrational de-excitation reactions. The characteristic diffusion time is orders of magnitude smaller than the residence time of the reactor [21], thus recombination reactions on the wall can be neglected. In the latter, the collision frequency is high enough to ensure a dominant vibrational de-excitation through VT relaxation processes. For the abovementioned reasons, neither recombination nor vibrational de-excitation reactions are included in the model. The included surface reactions are related to recombination or neutralization processes through which ions are grounded (green arrows in figure 3.1 and table 3.5) and restore the neutral charge. Due the low temperatures of heavy species, a unity sticking coefficient is assumed for these low energy collisions of ions with the walls [52,53]. Moreover, ions are consumed in these reactions and thus are needed to avoid their accumulation inside the reactor. The expression presented to calculate the rate coefficients can be simplified to the one shown below as no surface species are involved in the reactions.

$$k_s = \left(\frac{1}{1 - \gamma/2}\right)\left(\frac{k_B T_g}{2\pi m}\right)^{\frac{1}{2}} \tag{3.20}$$

3.3. Results and discussion

In this section, a comparison of the results obtained from the proposed reduced model and the detailed STS kinetic model is performed. A qualitative study of the key model parameters is also carried out to identify which parameter displays the highest influence on the reduced model predictions. A simple reactor model was built in the COMSOL Multiphysics-plasma module [54] for this purpose. Spatially uniform quasi-neutral plasma is assumed throughout the reactor volume.

In the previous section, a description of the calculation process to estimate the rate constants for highly relevant chemical reactions in the dissociation kinetics of CO_2 is provided. In this regard, the computed rate constants for reactions involving the lumped excited species CO_2^* are shown in figure 3.9. Two different zones are distinguished in this figure. At low temperatures, below 700-800 K, the rate

constants for the reactions with neutrals are relatively higher than the vibrational energy transfer reactions, thus leading to high dissociation rates of the CO_2 molecule. At high temperatures though, above 800 K, the vibrational reactions become dominant, resulting in a drop of the dissociation rate at the expense of increasing the bulk gas temperature.
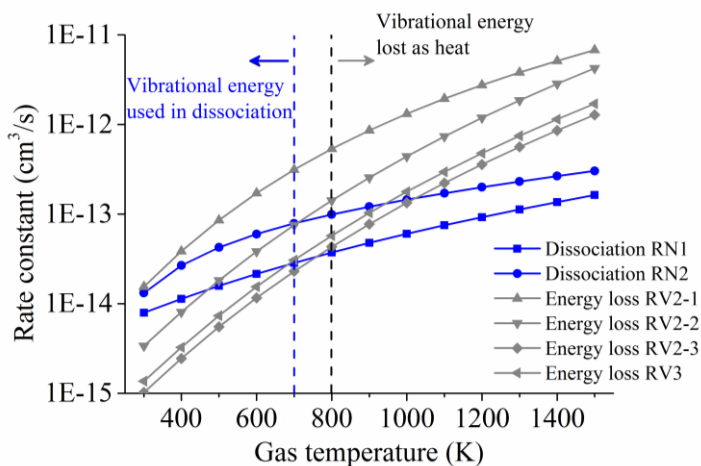

Fig. 3.9. Rate constants of the main reactions leading to dissociation of the CO_2 molecule (blue lines, RN1 and RN2) and the reactions causing energy loss (grey lines, RV2-1, RV2-2, RV2-3 and RV3).

3.3.1. Validation of the model

The simulations to investigate the validity of the reduced kinetic model are carried out at the same conditions as reported in [21]. The discharge takes place at a pressure of 100 torr, reduced electric field of 50 Td, electron density 10^{13} 1/cm^3, specific energy input 0.6 eV/molecule, frequency of the electromagnetic field 2.45 GHz and a residence time of 1.4 x 10^{-5} s. Elastic scattering and ionization reactions are not considered, and CO_2^+ is the only ion included for the quasi-neutrality of the plasma. The initial gas composition is a CO_2 mole fraction of 1; the initial bulk gas temperature is 300 K and the initial electron temperature is 0.39 eV or 4500 K.

In this work, the plasma medium is specified by the electron density and the mean electron energy. In the case of multidimensional simulations, where the spatial distribution and time evolution of the species concentration are to be studied, these parameters should be determined by solving the conservation laws and Boltzmann equation for the electrons. The energy equation is not included in the model. The

electron and gas temperatures profiles in the reactor volume are specified as functions fitted to the results given in [21]. Viscosity effects are neglected and the pressure is considered uniform and constant inside the reactor.

Mass conservation equations are solved for the species to validate the reaction kinetics. Diffusion is neglected given its relatively short characteristic time. Thus, for this specific validation model the surface reactions are not included and the charged species densities are constant. This is done for consistency with [21], even though the results are not affected by the kinetics of charged species. Convection is not considered and time dependent simulations are performed based on the residence time value.

The model is divided into two parts describing two spatial zones; these are the plasma zone, where the plasma is active, and the afterglow zone, where the plasma vanishes. In the former, a constant electron density and an increasing electron temperature profile describe the chemically reactive (plasma) zone. In the latter, the electron density is set to zero, whereas a decreasing electron temperature profile is specified to describe the zone where reactive species relax back to equilibrium and radicals recombine. It is known that the electron density is not constant in either zone, but setting a constant electron density seems to be a good approximation to study the influence of chemical reactions in the overall reactive scheme. The total simulation time is fixed to 0.1 s, which is long enough for the relaxation process (VT and VV') to take place. In conclusion, the inputs required for the model are the electron density, electron temperature, bulk gas temperature and pressure. The comparison of the benchmark STS kinetic model versus the proposed reduced kinetic model is displayed in figure 3.10 where the division of both zones can be observed. As expected, the dissociation of CO_2 occurs mainly in the plasma zone, whereas recombination processes take place in the afterglow.

The major difference as for the computed species concentrations is found in the plasma zone. In the afterglow, the species densities are in good agreement with the STS kinetic model. Notably, the predicted CO_2 density is virtually exact in both models, which in turn allows the calculation of the CO_2 dissociation rate. On the other hand, the concentration of CO and O_2 present an error lower than 10% and 20%, respectively. The steep slopes noticed in the time range $10^{-6} - 10^{-5}$ in figure 3.10a are the result of the STS kinetic model. The processes by which the energy is

transferred from the electrons to the lower levels of the vibrational ladder and then progressively transferred by VV relaxation to higher levels have a time scale of $\sim 10^{-6}$ s. Once the highest vibrational levels are excited, the dissociation of CO_2 starts taking place until the VT relaxation rates become comparable to the VV relaxation ones at about 10^{-5} s and therefore the dissociation rate declines. In the abovementioned time range, the stored vibrational energy enhances the dissociation processes by lowering the activation energy of the reactions. The rate constants for the dissociation processes are rather high, which explains the sharp increase in the densities of CO and O. The increase in the O_2 concentration is mainly due to the O recombination reaction (RN5, table 3.3). Concerning the reduced kinetic model, it is assumed that at low bulk gas temperatures, the lumped excited state CO_2* has a large population of the high vibrational levels, thus initiating the production of CO and O as soon as the species CO_2* is formed by means of electron collisions. This explains the slower dissociation process taking place in the reduced kinetic model in the range 10^{-7} to 10^{-5} s.
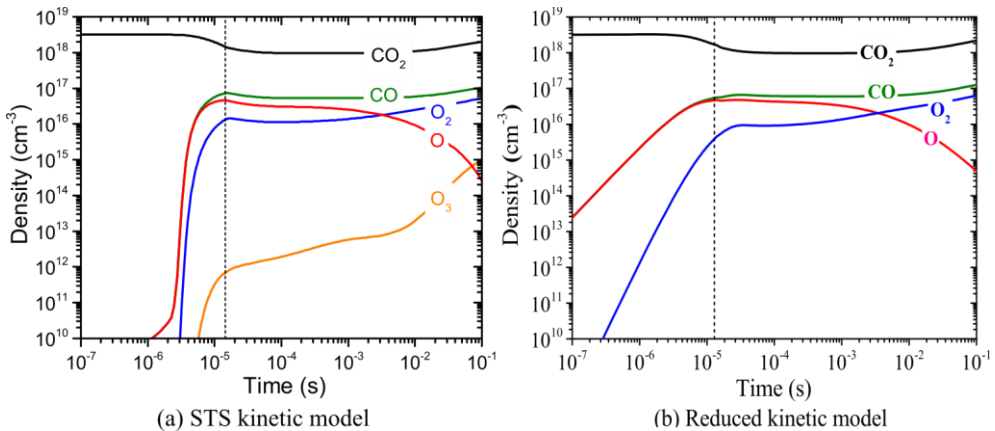

Fig. 3.10. (a) Population densities computed by the STS kinetic model, adapted from [21]. (b) Population densities calculated by the reduced kinetic model of the most relevant neutral species.

It is noticed that the predictions given by the model can be improved by adjusting the assumed value of the T_v/T_g ratio (see Simplification approach section) at low temperature. The value can be experimentally determined by measuring the vibrational and gas temperatures of the discharge, for instance, by optical emission spectroscopy [41]. This fact offers an evident benefit since the STS kinetic model does not enable such tuning due to the large number of reactions. At the very early stage in the plasma zone (10^{-7}-10^{-6} s), the results of the reduced kinetic model do

not match the ones from the STS model. Conversely, the densities calculated at the end of the plasma zone and the afterglow do match the predictions of the STS model. To validate other process conditions, the electron dynamics and the energy equation should be included in the model.

3.3.2. Effect of model parameters

The results presented in figure 3.10b are calculated using constant values of the following model parameters: stoichiometric coefficients $v_{l2} = 0.262$, $v_{s2} = 0.246$, $v_{l3} = 0.262$ and $v_{s3} = 0.869$ for a mean bulk gas temperature of 500 K in the discharge (plasma zone and afterglow). In section 3.2, it was shown that these factors are function of the bulk gas temperature. As stated in [21], the gas temperature increases from 300 to 560 K over the residence time in the plasma zone; therefore an alternative mean bulk gas temperature of 300 K is considered to study the effect of these parameters on the model predictions. It was proven that the error induced by keeping the parameters constant is relatively small since the species concentrations follow nearly the same trends. In this regard, the effect of the T_v/T_g ratio at the initial gas temperature (300 K) as well as the assumed gas temperature at which thermal equilibrium is reached are evaluated and displayed in figure 3.11.
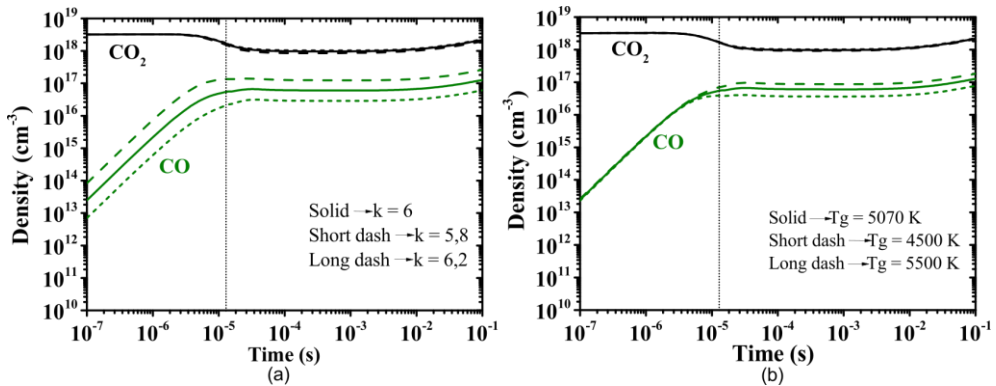
Fig. 3.11. (a) Population densities of CO_2 and CO for different T_v/T_g ratios ($T_v/T_g = k$) at constant gas temperature of 300 K. (b) Population densities for constant T_v/T_g ratio ($T_v/T_g = 6$) considering different gas temperatures at which the plasma becomes thermal.

As expected, when the value of T_v/T_g is higher ($T_v/T_g = 6.2$ – long dash line) the dissociation rate increases and vice versa ($T_v/T_g = 5.8$ – short dash line). As previously stated, the value of T_v/T_g at low temperatures can be seen as the dissociation potential; the higher the T_v/T_g value the higher the vibrational energy

stored in the molecules, thus conducting the process toward higher dissociation rates. The gas temperature at which the plasma becomes thermal seems to be much less influencing than the T_v/T_g ratio at low temperature. Lastly, it is shown that the value of T_v/T_g at low temperature has a higher influence on the predictions of the CO_2 dissociation rate, whereas the gas temperature at which quasi-equilibrium plasma conditions are reached does not have a major effect on the overall process. In this regard, experimental validation of the concept proposed in this work, where the T_v/T_g values are taken from [21], needs to be carried through measurements of the vibrational and gas temperatures in a pure CO_2 microwave discharge via optical emission spectroscopy. However, the experimental determination of these two temperatures is complex and only approximate values can be obtained using current plasma diagnostic techniques. Lastly, the actual implementation of the proposed kinetic model has not yet been done in multidimensional simulations. The computation of local rate constants considering spatial variations of the T_v/T_g ratio can be highly complex. Hence, a better approach is to use a characteristic T_v/T_g value to describe the reactor performance and keep the computational load at its minimum.

3.4. Conclusions

We have introduced a new methodology to simplify detailed plasma vibrational kinetics and applied it to the dissociation of CO_2 in non-equilibrium microwave plasma discharges. In this type of discharges, the dissociation kinetics of the CO_2 molecule are driven by the excitation of the highest vibrational levels of the asymmetric stretching mode. The novelty of the proposed model lies in four key elements; 1) the 21 vibrational levels considered for the asymmetric stretching mode are lumped within a single group, or fictitious species, CO_2^*, 2) this group follows the so-called non-equilibrium Treanor distribution, 3) an algebraic approximation is used to compute the vibrational temperature from the translational temperature based on the Landau-Teller formula and 4) weighted algebraic expressions are applied, instead of complex differential equations, to calculate the rates of the most influencing reactions. The reduced kinetic model comprises 44 reactions among 13 species, as opposed to our benchmark detailed kinetic model, in which +100 species and +10000 reactions are considered, thus reducing substantially the calculation time to less than a minute. For the validation of the reduced kinetic model, a reactor model was built in COMSOL Multiphysics. The predictions of the reduced kinetic model showed that the neutrals densities are in

good agreement with those predicted by the STS kinetic model, notably at the end of the plasma zone and the afterglow, which represent the reactor outlet.

The calculation process for the rate constants of the most influencing chemical reactions in the dissociation kinetics was described. Moreover, it was shown that the bulk gas temperature highly affects the dissociation rate as expected. Remarkably, at temperatures below 700 K, the dissociation rates are faster than the VT relaxation processes, thus resulting in higher conversion. Furthermore, a qualitative analysis of the key model parameters was carried out. The value of the T_v/T_g ratio at low temperature had a considerable effect on the calculation process. This ratio can be used as a fitting parameter to link the presented plasma kinetic model to experimentally measured vibrational and gas temperatures via optical emission spectroscopy. At this stage of development, where current models are in qualitative agreement with experimental data, the introduction of an experimentally obtained parameter describing the non-thermal degree of the discharge can facilitate the transition from STS to more practical models suitable for engineering purposes. Furthermore, this parameter may be used to fit experimental data to the model, improving the overall accuracy of the predictions.

To further assess the influence of plasma/process parameters, the electron dynamics and energy equations should be included in the model. This will be the next step towards development of a self-consistent multidimensional model for non-thermal plasma reactors. As a final note, we believe that the presented approach can also be applied to other plasma chemistries, in which the vibrational kinetics are dominant in the dissociation process.

References

1   J. F. Griffiths, *Prog. Energ. Combust.*, 1995, **21**, 25-107.

2   J. Amouroux, P. Siffert, J. P. Massue, S. Cavadias, B. Trujillo, K. Hashimoto, P. Rutberg, S. Dresvin and X. H. Wang, *Prog. Nat. Sci-Mater*, 2014, **24**, 295-304.

3   S. Sabihuddin, A. E. Kiprakis and M. Mueller, *Energies*, 2015, **8**, 172-216.

4   S. Hameer and J. L. van Niekerk, *Int. J. Energ. Res.*, 2015, **39**, 1179-1195.

5   T. M. I. Mahlia, T. J. Saktisandan, A. Jannifar, M. H. Hasan and H. S. C. Matseelar, *Renew. Sust. Energ. Rev.*, 2014, **33**, 532-545.

6   J. Amouroux and P. Siffert, *Spie Eco-Photonics 2011*, 2011, **8065**, 80650E.

7   Q. Wang, B. Spasova, V. Hessel and G. Kolb, *Chem. Eng. J.*, 2015, **262**, 766-774.

8   J. R. Roth, *Industrial Plasma Engineering*, IOP Publishing Ltd., 1995, vol. 1.

9   R. Aerts, W. Somers and A. Bogaerts, *Chemsuschem*, 2015, **8**, 702-716.

10 H. H. Kim and A. Ogata, *Eur. Phys. J. Appl. Phys.*, 2011, **55**, 13806.

11 V. D. Rusanov, A. A. Fridman and G. V. Sholin, *Uspekhi Fiz. Nauk*, 1981, **134**, 185.

12 A. Fridman, *Plasma chemistry*, Cambridge University Press, 2008.

13 Y. G. Ju and W. T. Sun, *Prog. Energ. Combust.*, 2015, **48**, 21-83.

14 Y. Yang, W. Hua and S. Y. Guo, *Phys. Plasmas*, 2014, **21**, 040702.

15 M. Baeva, A. Bosel, J. Ehlbeck and D. Loffhagen, *Phys. Rev. E*, 2012, **85**, 056404.

16 M. Jimenez-Diaz, E. A. D. Carbone, J. van Dijk and J. J. A. M. van der Mullen, *J. Phys. D. Appl. Phys.*, 2012, **45**, 335204.

17 P. Gokulakrishnan, R. Joklik, D. Viehe, A. Trettel, E. Gonzalez-Juez and M. Klassen, *J. Eng. Gas Turb. Power*, 2014, **136**, 011503.

18 A. Cenian, A. Chernukho, V. Borodin and G. Sliwinski, *Contrib. to Plasm Phys.*, 1994, **34**, 25-37.

19 E. V. Kustova and E. Nagnibeda, *Chem. Phys.*, 2006, **321**, 293-310.

20 T. Kozak and A. Bogaerts, *Plasma Sources Sci. Technol.*, 2014, **23**, 045004.

21 T. Kozak and A. Bogaerts, *Plasma Sources Sci. Technol.*, 2015, **24**, 015024.

22 G. van Rooij, D. van den Bekerom, N. den Harder, T. Minea, G. Berden, W. Bongers, R. Engeln, M. Graswinckel, E. Zoethout and M. van de Sanden, *Faraday Discuss.*, 2015, **183**, 233-248.

23   A. Stagni, C. Saggese, M. Bissoli, A. Cuoci, A. Frassoldati, T. Faravelli and E. Ranzi, *Iconbm: International Conference on Biomass, Pts 1 and 2*, 2014, **37**, 877-882.

24   T. E. Magin, M. Panesi, A. Bourdon, R. L. Jaffe and D. W. Schwenke, *Chem. Phys.*, 2012, **398**, 90-95.

25   A. Guy, A. Bourdon and M. Y. Perrin, *Chem. Phys.*, 2013, **420**, 15-24.

26   H. P. Le, A. R. Karagozian and J. L. Cambier, *Phys. Plasmas*, 2013, **20**, 123304.

27   L. F. Spencer and A. D. Gallimore, *Plasma Sources Sci. Technol.*, 2013, **22**, 015019.

28   K. Peerenboom, A. Parente, T. Kozak, A. Bogaerts and G. Degrez, *Plasma Sources Sci. Technol.*, 2015, **24**, 025004.

29   Y. Itikawa, *J. Phys. Chem. Ref. Data*, 2002, **31**, 749-767.

30   K. Kameta, N. Kouchi and Y. Hatano, in *Interactions of Photons and Electrons with Molecules*, Springer-Verlag, Berlin/Heidelberg, 2003, vol. 17C, pp. 4001–4061.

31   A. Zecca, G. P. Karwasz and R. S. Brusa, *Riv. Nuovo Cimento*, 1996, **19**, 1-146.

32   Y. Itikawa, *J. Phys. Chem. Ref. Data*, 2009, **38**, 1-20.

33   R. R. Laher and F. R. Gilmore, *J. Phys. Chem. Ref. Data*, 1990, **19**, 277-305.

34   H. T. Zheng and Q. Liu, *Math. Probl. Eng.*, 2014, **vol. 2014**, 938618.

35   A. H. Markosyan, A. Luque, F. J. Gordillo-Vazquez and U. Ebert, *Comput. Phys. Commun.*, 2014, **185**, 2697-2702.

36   G. Colonna, I. Armenise, D. Bruno and M. Capitelli, *J. Thermophys. Heat Tr.*, 2006, **20**, 477-486.

37   G. Colonna, L. D. Pietanza and M. Capitelli, *J. Thermophys. Heat Tr.*, 2008, **22**, 399-406.

38   A. Berthelot and A. Bogaerts, *Plasma Sources Sci. Technol.*, 2016, **25**, 045022.

39   C. E. Treanor, J. W. Rich and R. G. Rehm, *J. Chem. Phys.*, 1968, **48**, 1798–1807.

40   H. S. Kwak, H. S. Uhm, Y. C. Hong and E. H. Choi, *Sci. Rep-Uk*, 2015, **5**, 18436.

41   T. Silva, N. Britun, T. Godfroid and R. Snyders, *Plasma Sources Sci. Technol.*, 2014, **23**, 025009.

42 L. D. Pietanza, G. Colonna, G. D'Ammando, A. Laricchiuta and M. Capitelli, *Chem. Phys.*, 2016, **468**, 44-52.

43 K. Anzai, H. Kato, M. Hoshino, H. Tanaka, Y. Itikawa, L. Campbell, M. J. Brunger, S. J. Buckman, H. Cho, F. Blanco, G. Garcia, P. Limao-Vieira and O. Ingolfsson, *Eur. Phys. J. D*, 2012, **66**, 36.

44 S. J. Buckman, J. W. Cooper, M. T. Elford, M. Inokuti, Y. Itikawa and H. Tawara, *Interactions of Photons and Electrons with Atoms*, Springer-Verlag, Berlin/Heidelberg, 2000, vol. 17A.

45 Y. Itikawa, *Molecular processes in plasmas*, Springer Series on atomic, optical and plasma physics, Vol. 43 (Springer Berlin Heidelberg), 2007.

46 R. D. Levine and R. B. Bernstein, in *Dynamics of Molecular Collisions*, Springer US, Boston, MA, 1976, pp. 323–364.

47 J. A. Blauer and G. R. Nickerson, *A survey of vibrational relaxation rate data for processes important to CO2–N2–H2O infrared plume radiation*, Irvine, California, 1973.

48 T. Kozák, *Private communication*, 2015.

49 R. N. Schwartz, Z. I. Slawsky and K. F. Herzfeld, *J. Chem. Phys.*, 1952, **20**, 1591-1599.

50 J. Keck and G. Carrier, *J. Chem. Phys.*, 1965, **43**, 2284-2298.

51 R. J. Kee, M. E. Coltrin and P. Glarborg, *Chemically Reacting Flow*, John Wiley & Sons, Inc., Hoboken, NJ, USA, 2003.

52 K. Hassouni, F. Silva and A. Gicquel, *J. Phys. D. Appl. Phys.*, 2010, **43**.

53 A. J. Ryan, *Emerging Themes in Polymer Science*, The Royal Society of Chemistry, 2001.

54 COMSOL, *Plasma Module User's Guide*, COMSOL 4.4, 2013.

4

A TWO-STEP MODELING APPROACH FOR PLASMA REACTORS – EXPERIMENTAL VALIDATION FOR CO₂ DISSOCIATION IN SURFACE WAVE MICROWAVE PLASMA

Plasma reactors have the potential to enable CO_2 utilization technologies and so there is need to investigate their performance from a chemical or process engineering perspective. Multiphysics models are excellent tools to carry out this analysis; however, practical engineering models of plasma reactors are limited. Herein a two-step modeling approach for plasma reactors is presented. In the first step, a 2D plasma reactor model with a simple chemistry is used to characterize the discharge. The result of this step is used in the second step to develop a global (volume averaged) model of the reactor with the actual chemistry. The approach is applied in the case of CO_2 dissociation in a non-thermal surface wave microwave plasma reactor. Preliminary calculations reveal the need to include the vibrationally enhanced dissociation of CO_2 in the chemistry of the model. Reduced vibrational kinetics are employed for this purpose by introducing the fictitious species CO_2*. The model predictions are compared to experimental results to validate the model and obtain insight into the performance of the reactor. In comparison to the experimental results the conversions obtained with the model are underestimated between 11% and 25%. The dominant dissociation paths in the plasma reactor are also identified. Further calculations are performed to show the importance of an approximate description of the power deposition. Limitations of the approach are discussed as well, especially those with major contribution to the discrepancies between experimental and modeling results.

4.1. Introduction

The utilization of CO_2 emerges as a promising approach in the blend of solutions to cope with two major challenges confronted by human society nowadays, global warming and low-carbon circular economy. Among the CO_2 utilization alternatives, the concept of solar fuels stands out, as the surplus in green electricity is used to produce synthetic fuels from CO_2. Thus, the limitations of renewable sources with respect to their unsteady nature are removed by storing the surplus of green electricity as a fuel that can be used in high demand periods.

Microwave plasma has the potential to enable this technology due to its particular characteristics that allow for efficient splitting of the CO_2 molecule, reaching energy efficiencies up to 90% [1]. The mechanism behind the efficient dissociation of CO_2 is the vibrationally enhanced dissociation, in which the vibrational energy of highly excited states in the asymmetric vibrational mode can decrease the activation energy of the dissociation reaction. That way, the endothermic reaction is carried out efficiently, breaking the very stable CO_2 molecule. The importance of vibrational excitation for achieving an efficient dissociation in diatomic and triatomic molecules has already been known for decades [2,3]. In a nutshell, under adequate conditions, the low-lying asymmetric vibrational states get excited by electron collisions and they transfer their energy to higher vibrational states thus creating an overpopulation of highly energetic states that can easily dissociate. This is claimed to be the most efficient dissociation mechanism; a detailed description can be found elsewhere [1,4].

After some years in the shadows, the CO_2 dissociation by means of non-thermal plasma has recently been brought back to the spotlight, mainly due to the crucial need to find solutions to the aforementioned challenges [5]. From the modeling point of view, research groups in Antwerp, Bari and Lisbon have been working on the fundamental understanding of the physical and chemical processes taking place in the plasma. For this purpose, the Boltzmann equation for the electrons is solved together with detailed kinetic models that involve specific interactions between distinct energy states of the molecules [6–11]. From the experimental point of view, various techniques have recently been used to gain new insights into the effect of different plasma configurations, operating conditions and gas compositions on the behavior of CO_2-containing plasmas [12–21]. Despite these efforts, not all processes taking place inside the plasma, or involved in the dissociation, are fully understood

and crucial data required for modeling, such as cross sections or rate constants, are not available.

Given the potential of the technology, it is beneficial to investigate its performance from a chemical or process engineering point of view. Thus, there is need for practical engineering plasma models that consider dimensionality and transport, and ultimately allow for integration of a plasma reactor to a process system. In this document, we describe a two-step modeling approach for plasma reactors, applied to the specific case of CO_2 dissociation in a non-thermal surface wave microwave plasma reactor. The work is continuation of our previous published research on the matter [12,13,22]. In the first step, the two-dimensional axisymmetric Argon plasma model, developed in [13], is used to characterize the discharge by identifying the power losses, the deposited power density patterns and the time and length scales as well as by performing a qualitative analysis of the plasma and process variables. These results are then used in the second step to develop the model of the CO_2 plasma reactor. During the process, the need to include the vibrationally enhanced dissociation in the chemistry of the model is identified. For this purpose, the methodology for the reduction of vibrational kinetics in non-equilibrium microwave plasma presented in [22] is used. The final model predictions are compared to our previously published experimental results [12] to validate the model and get insight into the performance of our lab-scale reactor. The reader is referred to [12,13,22] for further details on the reduction methodology, the experimental setup and the Argon model.

4.2. First Step: Power deposition and discharge characterization

The energy required for the CO_2 dissociation comes from the microwave power, which is transferred to the electrons and from these to other species. It reaches the highest values inside the surface wave launcher (Surfatron), where most of the microwave power is deposited, and decreases downstream. An estimate of the power deposition per unit volume (deposited power density) can be obtained from our previously developed two-dimensional model of an Argon plasma [13].

The physics of this self-consistent model involve variables whose times and lengths scales differ widely in magnitude, making the non-linear system of equations numerically challenging to solve. Simple chemistries, such as Argon, are preferred in this first step as they allow for the characterization of the discharge

without adding much more complexity to the system of equations. The opposite is true for complex chemistries, such as CO_2 dissociation, for which vibrationally excited states must be included in the non-thermal plasma model. The kinetics of vibrationally excited states lead to very high gradients and rates during the solution of the system of equations as well as numerical instabilities early in the simulation that impede the solution of equations.

The Argon model was slightly modified to account for the heat removal from the reactor. In our experimental setup the cooling system consisted of cooling water at 5 °C flowing inside the Surfatron and compressed air at 20 °C blowing inside the cavity (between the Surfatron and the quartz tube). A detailed modeling of the cooling system is outside the scope of the present work. Thus, for the sake of simplicity the inner wall temperature of the quartz tube was fixed to a specific value.

Simulations at the experimental conditions of the pure CO_2 dissociation reported in [12] were performed in the Argon model to investigate the power deposition in the reactor. In the experiments, the microwave power input was 150 W, the pressure 20 mbar, the inlet temperature 300 K and the inlet flowrate 100, 200 and 300 sccm. The simulations were carried out in a time dependent solver until 0.02 s, which is sufficient time for the process to reach steady state. The results of the simulation for an inlet flowrate of 300 sccm and a tube inner wall temperature of 300 K are shown in figures 4.1-3. Qualitatively similar results were obtained for the other flowrates. The analysis of the results is only performed in the axial direction due to its relevance with the second step of the approach.

Figure 4.1 shows the steady state average values of the electron density, electron temperature and gas temperature as a function of z (axial coordinate). These profiles are obtained by integrating the variables in the radial and angular directions and dividing the result over the cross section of the quartz tube. The steady state for these variables is obtained at ~0.006 s, given their direct relation with the electron kinetics, which are characterized by very short timescales. The steady state for the average velocity and the pressure is reached later, at 0.016 s (profiles shown in figure 4.2).

The steady state of the average deposited power density is shown in figure 4.3. This profile remains constant after 0.006 s, when the plasma variables have also

reached their steady states. However, the portion of the profile corresponding to the Surfatron body (between 38 and 118 mm) stabilizes earlier in the simulation, at ~0.001 s. In this zone, the plasma is ignited and most of the power is deposited.
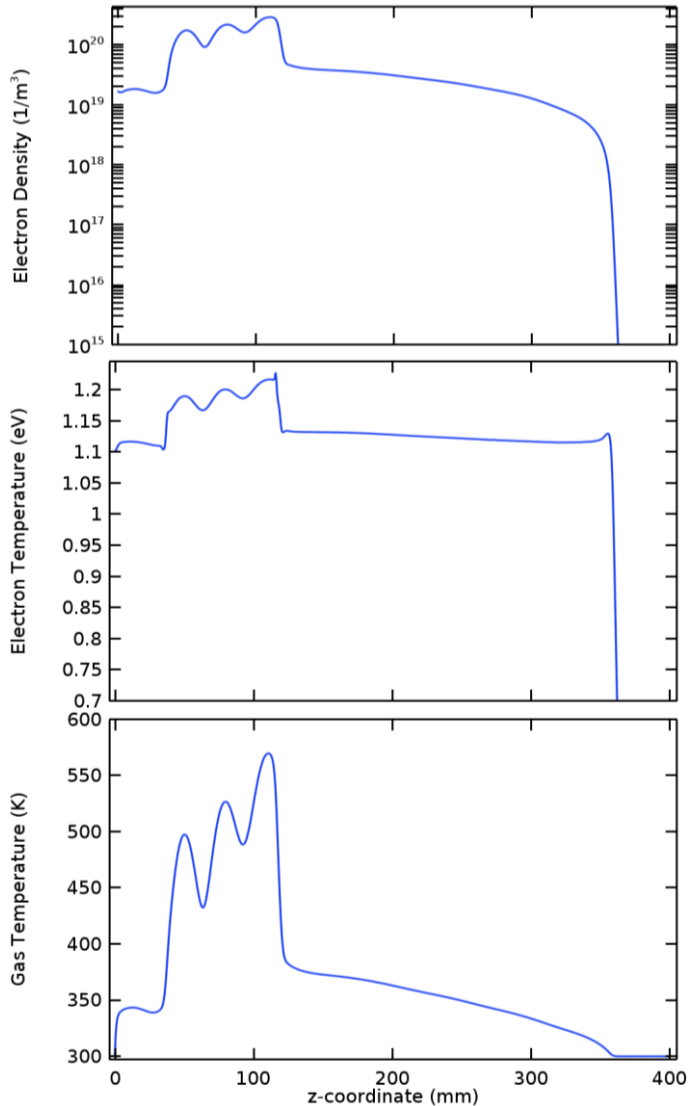

Fig. 4.1. Electron density (top), electron temperature (middle) and gas temperature (bottom) profiles at steady state (0.006 s). These profiles were obtained using the Argon model [13] for a flowrate of 300 sccm, inlet temperature of 300 K, inner wall temperature of 300 K, outlet pressure of 20 mbar and a microwave power input of 150 W. (1 eV ≈ 11600 K).

In a surface wave discharge, the generated plasma serves as a propagating medium for the surfaces waves that are created and shaped inside the surface wave launcher. These electromagnetic waves travel axially in both directions inside the plasma while feeding it with their power [23]. This can be easily seen in figure 4.3, where the power density decreases as the electromagnetic waves travel through the plasma and completely vanishes when the plasma does as well (see figure 4.1). The power density oscillations, also observed in figure 4.3, are related to the variations in the magnitude of the surface wave electric field and, particularly, its axial component. Inside the plasma the axial component of the electric field dominates over the radial component, thus having a larger contribution to the power deposition. Outside of the plasma, the radial component dominates [24]. It can also be seen that all variables exhibit fluctuations driven by the power deposition fluctuations inside the Surfatron body.
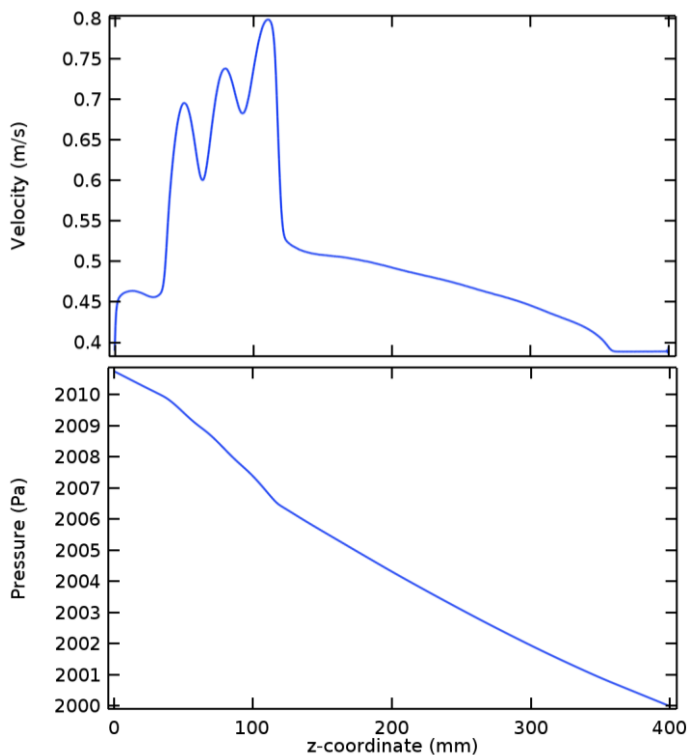

Fig. 4.2. Velocity (top) and pressure (bottom) profiles at steady state (0.016 s). Argon model at the same conditions given in figure 4.1.

Electrons are the driving force in a plasma, they take energy form the microwaves before transferring it to the heavy species. The behavior of the variables in figures 4.1 and 4.2 can be explained in simple terms from the variations seen in figure 4.3. The microwave power energizes the electrons, increasing their mean energy, which is proportional to the electron temperature. High ionization rates are obtained at high electron temperatures and therefore high electron densities are located at zones of high deposited power densities. Conversely, more power can be deposited in zones of high electron densities. The electrons subsequently transfer their energy to the Argon species via elastic and inelastic collisions, which ultimately leads to a local increase of the gas temperature where high electron densities are located. Similarly, the velocity increases at zones of high temperatures due to the local expansion of the gas. For this ideal gas, the variation between the temperature and the velocity is roughly linear given the very low pressure drop. At higher local velocities the pressure drop increases, but for the entire reactor it remains low and almost linear with the tube length, as expected for this laminar flow.

The total power deposited in the plasma is 121.8 W, which corresponds to the area below the curve of figure 4.3 multiplied by the quartz tube cross section. This value is smaller than the 150 W of microwave power input to the Surfatron due to the leakage of microwaves. Figure 4.4 shows the time average power flow in the positive radial and z directions at the edge of the Surfatron body, where most of the microwave leak takes place. The addition of a waveguide at the Surfatron outlet has proven to be successful in limiting these power losses, thereby increasing the overall performance of the reactor for the case of CO_2 reduction with hydrogen [13].

Another important quantity is the 89.4 W of power that is deposited inside the Surfatron body, within a length of approximately 8 cm. This gives an average power density of 8.9×10^7 W/m^3, which is enough to ignite and sustain the plasma. The remaining 32.4 W are deposited at considerably lower power densities, with an average power density of 9.5×10^6 W/m^3 over 27 cm of plasma (approximately 35 cm of total Argon plasma length according to figure 4.1).
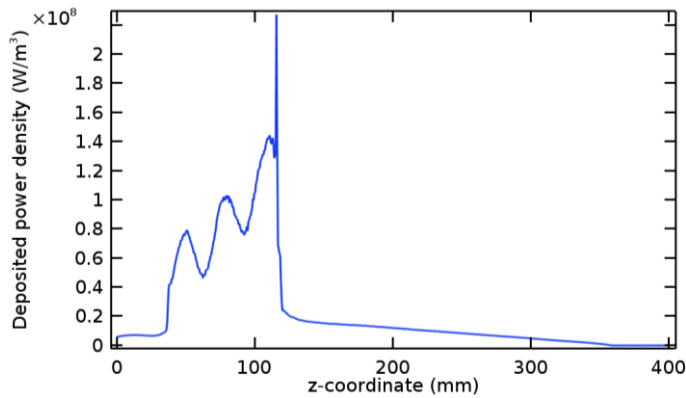
Fig. 4.3. Deposited power density profile at steady state (0.006 s). Argon model at the same conditions given in figure 4.1. The power density peak seen at 116 mm is related to the intense electric field formed at this point due to the Surfatron design (see small protrusion at the bottom of figure 4.4).
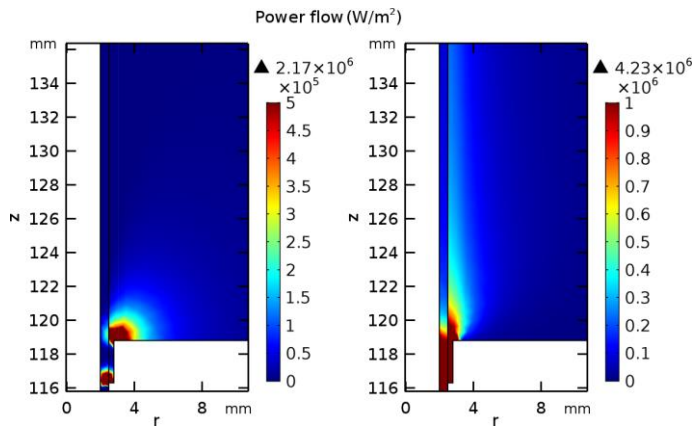
Fig. 4.4. Time average power flow (0 to 0.02 s) in the positive radial direction (left) and positive z direction (right). Argon model at the same conditions given in figure 4.1.

Figure 4.5 shows the evolution of the power deposition in time, distinguishing the total deposited power from the power deposited inside the Surfatron body. These two quantities reach their steady state values at approximately the same time as the plasma variables do (0.006 s) and their difference is established at the early stages of the discharge.

Additional simulations were performed for the lowest experimental inlet flowrate and a higher wall temperature (results summarized in table 4.1). It is concluded that in our setup for an Argon plasma at the conditions of the CO_2 dissociation

experiments, approximately 80% of the power input is deposited into the plasma and 20% in lost to the surroundings. Moreover, 60% of the power input is deposited effectively at high power densities, while 20% is gradually deposited at low power densities. The latest plays a role in sustaining the plasma, although its effectiveness in this regard is considerably inferior for a molecular plasma, due to the internal degrees of freedom of the molecules (mainly vibration at low electron temperatures). Molecular plasmas are highly collisional in comparison to atomic plasmas; consequently the electron temperature is lower and decays faster in space and time. Therefore, in the so-called afterglow, the small amount of energy gained by the electrons at low power densities is predominantly transferred to vibrational states (of CO_2, CO and O_2 molecules in a CO_2 plasma) and ultimately to heat, further increasing the temperature and the relaxation rates.
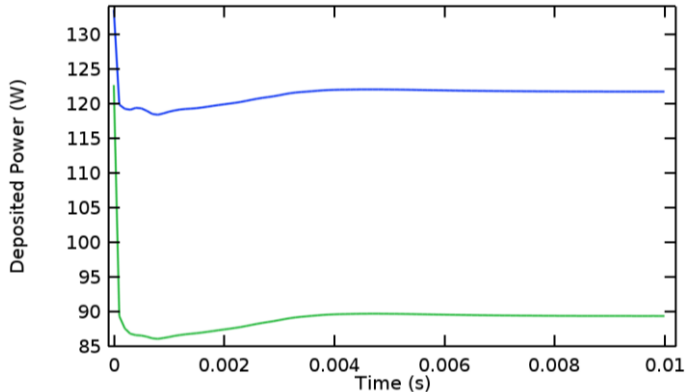
Fig. 4.5. Deposited microwave power over time. Blue: total deposited power, green: deposited power inside the Surfatron body (at high power densities). Argon model at the same conditions given in figure 4.1.

The quartz tube temperature has a minor effect on the power deposition according to the results shown in table 4.1. The real temperature of the inner wall is clearly not uniform along the reactor, but measurements indicated that it ranged from 50 to 90 °C downstream of the Surfatron [12]. A rough estimation of the surface plasma/inner reactor wall temperature was also done by means of thermal imaging, showing temperatures as high at 600 K at the Surfatron outlet [13]. The variation of the deposited power is shown to be small within the range of these temperatures.

Table 4.1. Deposited power and deposition efficiencies at selected inlet flowrates and wall temperatures T_w. The results were obtained with the Argon model for an inlet temperature of 300 K, outlet pressure of 20 mbar and a microwave power input of 150 W. SB: Surfatron body.

Flowrate (sccm)	T_w (K)	Total P_{dep} (W)	Deposition eff. (%)	$P_{dep, SB}$ (W)	SB-Deposition eff. (%)
100	300	123.1	82%	91.1	61%
100	600	126.0	84%	92.7	62%
300	300	121.8	81%	89.4	60%
300	600	125.9	84%	92.6	62%

To illustrate the approach, a profile similar to that of figure 4.3 is used as input to the global model for CO_2 dissociation. Using a profile based on the results of the Argon model is more descriptive than a power input value as it gives information on where and how the power is deposited into the plasma. This information is necessary for the modeling of the reactor, given its direct relation with the plasma variables. Furthermore, it is also closer to reality than assuming, for instance, a uniform power deposition in the plasma.

The simplified deposited power density profile used in the CO_2 model is designed to be easier to construct and adjust to the CO_2 plasma, while retaining the main characteristics of the profile shown in figure 4.3 that is, a high and oscillating power density inside the Surfatron body and a lower and approximately linearly decaying power density outside of it. The deposited power density profile, $P_{d,den}(z)$, can be computed using the following equation, in which r_i is the inner radius, L_p is the length of the plasma and P_{dep} is the total deposited power computed from the power input and the deposition efficiency.

$$\iiint_V P_{d,den}\, dV = \pi r_i^2 \int_{L_p} P_{d,den}(z)dz = P_{dep} \tag{4.1}$$

4.3. Second step: Global model in a Lagrangian approach

In a so-called global model the variables are averaged over the reactor volume, removing the spatial dependence in the equations. Thus, the equations to solve are simplified to the much simpler rate equations, such as the following equation for the conservation of species

$$\frac{dn_i}{dt} = R_{prod,i} - R_{loss,i} \tag{4.2}$$

where the rates of production and loss of a species i is given by the chemical reactions. The electron temperature is computed by the following equations

$$e\frac{dn_\varepsilon}{dt} = R_\varepsilon + P_{d,den} + R_{ion}(\varepsilon_e + \varepsilon_i) \tag{4.3}$$

$$T_e = \frac{2}{3}\bar{\varepsilon} = \frac{2}{3}\frac{n_\varepsilon}{n_e} \tag{4.4}$$

where e is the elementary charge, n_ε the electron energy density, R_ε the electron energy loss over all electron impact reactions (see table 4.4), $P_{d,den}$ the deposited power density, R_{ion} the rate of ion losses to the walls (see table 4.8, reaction RS3), $(\varepsilon_e + \varepsilon_i)$ the mean energy lost per electron-ion pair lost to the wall (see section 4.3.3), $\bar{\varepsilon}$ the mean electron energy and n_e the electron density, which is computed from the electroneutrality assumption.

These time-dependent equations can be used in a Lagrangian description to obtain a one-dimensional model of the plasma reactor. In this approach, it is assumed that the reactor behaves as a plug flow reactor and a perfectly mixed volume element is tracked in the time domain as it flows throughout the reactor. There is no flow entering or leaving the volume element. The microwave power is deposited in the volume element depending on its position according to the profile computed from equation 4.1. The velocity of the element is computed from the flowrate and process conditions, and it is integrated to find its position. This also allows to transform the results of the global model from the time domain into the space domain, i.e. the axial coordinate. In section 4 all results are conveniently given in the space domain, as functions of z and not time. Figure 4.6 illustrates the approach.

Radial and angular variations of the variables inside the reactor are neglected by using this approach. The volume element is axisymmetric, with a radius equal to the inner radius of the quartz tube used in the experimental setup, 2 mm. The length of the quartz tube is approximately 40 cm from the starting point of the surface wave launcher to the sampling point for the mass spectroscopy analysis used for the quantification of the gas composition. Tubing of 3 mm inner radius and 2.5 m length connects the sampling point to the mass spectrometer.
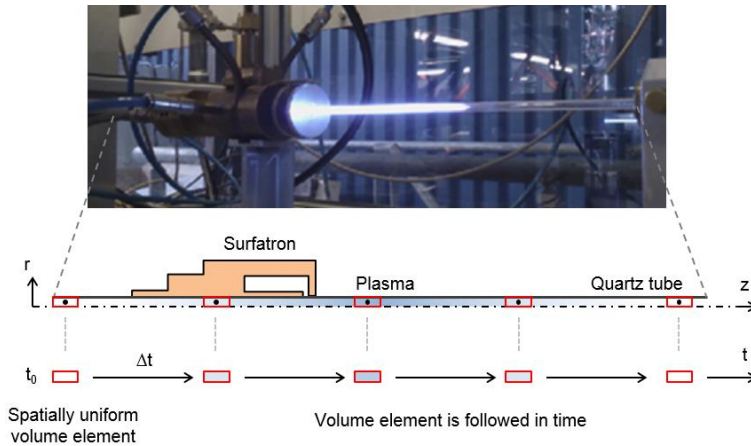
Fig. 4.6. Approach for modeling CO_2 dissociation in a microwave plasma reactor. Top: Experimental setup used in [12], middle: Two-dimensional axisymmetric sketch of the reactor [13], bottom: Approach used in this work.

This simple model can predict the plasma and process variables within reasonable agreement while using much less computational resources than a two-dimensional model. The COMSOL Multiphysics' Plasma Module was used for the implementation of the global model. A detailed explanation of the equations solved in this module can be found elsewhere [25], herein only brief explanations are provided when needed. The following subsections describe the most relevant aspects of the global model.

4.3.1. Species

The species included in the CO_2 model are listed in table 4.2. These consist of neutral, excited and charged species. CO_2 and the products of its dissociation comprise the neutral species. Excited states refer to the internal degrees of freedom of CO_2 used in the calculation of the electron temperature and the fictitious species CO_2* [22], which groups all levels in the asymmetric vibrational mode of the CO_2 molecule. As mentioned before, highly excited states in this vibrational mode are involved in the vibrationally enhanced dissociation of CO_2.

Table 4.2. Species considered in the CO_2 model.

Type	Species
Neutral ground states	CO_2, CO, O, O_2
Vibrationally excited states	$CO_2 v_i$, CO_2*
Electronically excited states	$CO_2 e_1$, $CO_2 e_2$
Charged species	CO_2^+, O^-, e

Vibrational and electronically excited states are only included for CO_2, considering that it is the initial and dominant species in the discharge and therefore it has the highest influence in the electron kinetics. Table 4.3 lists the excited states along with their energy levels and statistical weights. The vibrational state of a CO_2 molecule is given by three quantum numbers $(i\,j\,k)$ describing the vibrational levels in the symmetric stretching, symmetric bending and asymmetric stretching modes, respectively. The symmetric bending levels are degenerate as the bending can take place in orthogonal planes, having, for a vibrational level j a degeneracy of $j + 1$. In addition, the symmetric levels $((i + 1)\,j\,k)$ and $(i\,(j + 2)\,k)$ are coupled due to the proximity of their energy levels, implying that they coexist and therefore are usually grouped into a single species. The statistical weights given in table 4.3 refer to the total degeneracy of the species. In the case of $CO_2 v_8$, the statistical weight was computed considering the coupled symmetric levels with a maximum energy slightly lower than the energy threshold of the excitation cross section. The electronically excited species are assumed to be non-degenerate. Lastly, two charged species besides electrons are considered, the positive ion CO_2^+ and the negative ion O^-. The production/consumption of these two species is coupled to the electron density due to the electroneutrality assumption. Lower electron densities are obtained at a higher production of O^- and the opposite is true for CO_2^+.

Table 4.3. Excited states included in the CO_2 model. The species and their energies are based on [10].

Species	Vibrational states	Threshold (eV)	Statistical Weight
$CO_2 v_1$	$(0\ 1\ 0)$	0.083	2
$CO_2 v_{2a}$	$(0\ 2\ 0)$	0.167	3
$CO_2 v_{2b}$	$(1\ 0\ 0)$	0.167	1
$CO_2 v_3$	$(0\ 3\ 0) + (1\ 1\ 0)$	0.252	6
$CO_2 v_4$	$(0\ 0\ 1)$	0.291	1
$CO_2 v_{5a}$	$(2\ 0\ 0)$	0.339	1
$CO_2 v_{5b}$	$(0\ 4\ 0) + (1\ 2\ 0) + (0\ 1\ 1)$	0.339	10
$CO_2 v_6$	$(0\ 5\ 0) + (2\ 1\ 0) + (1\ 3\ 0) + (0\ 2\ 1) + (1\ 0\ 1)$	0.422	12
$CO_2 v_{7a}$	$(3\ 0\ 0)$	0.505	1
$CO_2 v_{7b}$	$(0\ 6\ 0) + (2\ 2\ 0) + (1\ 4\ 0)$	0.505	15
$CO_2 v_8$	$(0\ n\ 0) + (n\ 0\ 0)$	2.500	256
$CO_2 e_1$	-	7.0	1
$CO_2 e_2$	-	10.5	1

4.3.2. Reactions

The set of reactions is based on our previous work and has been updated according to the species, which now include a negative ion and more excited states. The reactions are mainly elementary two-body reactions and few three-body reactions. They are further divided into electron impact reactions, vibrational energy transfer reactions, reactions between neutral species, reactions involving charged species and surface reactions. Tables 4.4-8 show these reactions.

The energy gained by the electrons from the electromagnetic fields is transferred to other species through electron impact reactions. Their rate constants are given as functions of the mean electron energy in the form of tabulated data. The cross sections used for the calculations are given in the references of table 4.4. These cross sections were integrated with a Maxwellian Electron Energy Distribution Function (EEDF) for mean electron energies up to 10 eV. It is known that the EEDF is in general non-Maxwellian and the rate constants of electron impact processes can be overestimated due to this assumption, particularly for high energy processes. To illustrate this, the rate constant for the direct electron impact dissociation (RX15 in table 4.4) can be overestimated up to an order of magnitude for low electron temperatures (~0.7 eV), when compared to the result obtained by solving the Two-Term Approximation of the Boltzmann equation. For higher electron temperatures (~2 eV), the rate constant is overestimated by less than 40%. The same comparison for the vibrational excitation of the first asymmetric level (low energy process, RX6 in table 4.4) gives an overestimation of around 20% for an electron temperature of 0.7 eV. For higher electron temperatures (>1.8 eV), the deviation is only 1%. Nevertheless, it is very important to remark that different values of the mean electron energy are obtained when the energy conservation equation for the electrons (equation 4.3) is solved with rates computed with a Maxwellian EEDF and a non-equilibrium EEDF. Therefore, the overestimations mentioned before do not represent the error induced in the rates of the electron impact processes by assuming a Maxwellian EEDF. Indeed, the error is expected to be smaller considering the higher mean electron energies required for a non-equilibrium EEDF to achieve an ionization rate comparable to that obtained with a Maxwellian EEDF. The electron temperature determining the Maxwellian EEDF is computed using equations 4.3 and 4.4.

Table 4.4. Electron impact reactions. Rate constants computed from the cross sections of the references, except for reactions RX16 and RX22 which are given directly (see notes).

No	Process	Reaction	Ref	Note
RX1	Elastic scattering	$e + CO_2 \rightarrow e + CO_2$	10	A
RX2	Dissociative attachment	$e + CO_2 \rightarrow CO + O^-$	10	
RX3a	Vibrational excitation	$e + CO_2 \rightarrow e + CO_2 v_1$	10	
RX3b	Superelastic deexcitation	$e + CO_2 v_1 \rightarrow e + CO_2$	10	
RX4a	Vibrational excitation	$e + CO_2 \rightarrow e + CO_2 v_{2a}$	10	
RX4b	Vibrational excitation	$e + CO_2 \rightarrow e + CO_2 v_{2b}$	10	
RX5	Vibrational excitation	$e + CO_2 \rightarrow e + CO_2 v_3$	10	
RX6	Vibrational excitation	$e + CO_2 \rightarrow e + CO_2 v_4$	10	
RX7a	Vibrational excitation	$e + CO_2 \rightarrow e + CO_2 v_{5a}$	10	
RX7b	Vibrational excitation	$e + CO_2 \rightarrow e + CO_2 v_{5b}$	10	
RX8	Vibrational excitation	$e + CO_2 \rightarrow e + CO_2 v_6$	10	
RX9a	Vibrational excitation	$e + CO_2 \rightarrow e + CO_2 v_{7a}$	10	
RX9b	Vibrational excitation	$e + CO_2 \rightarrow e + CO_2 v_{7b}$	10	
RX10	Vibrational excitation	$e + CO_2 \rightarrow e + CO_2 v_8$	10	
RX11	Electronic excitation	$e + CO_2 \rightarrow e + CO_2 e_1$	10	
RX12	Electronic excitation	$e + CO_2 \rightarrow e + CO_2 e_2$	10	
RX13	Total ionization	$e + CO_2 \rightarrow 2e + CO_2^+$	10	
RX14a	Vibrational excitation	$e + CO_2 \rightarrow e + CO_2^*$	22	
RX14b	Superelastic deexcitation	$e + CO_2^* \rightarrow e + CO_2$	22	
RX15	Electron impact dissociation	$e + CO_2 \rightarrow e + CO + O$	26	B
RX16	Dissociative recombination	$e + CO_2^+ \rightarrow CO + O$	27	C
RX17	Elastic scattering	$e + CO \rightarrow e + CO$	28	A
RX18	Elastic scattering	$e + O_2 \rightarrow e + O_2$	29	A
RX19	Dissociative attachment	$e + O_2 \rightarrow O + O^-$	29	D
RX20a	Electron impact dissociation	$e + O_2 \rightarrow e + O + O$	29	D,E
RX20b	Electron impact dissociation	$e + O_2 \rightarrow e + O + O$	29	D,F
RX21	Elastic scattering	$e + O \rightarrow e + O$	29	G
RX22	Three-body electron attachment	$e + O + M \rightarrow O^- + M$	30	H

Notes

A: Computed from the cross section set of the reference.

B: The total cross section referred as the sum of partial cross sections is used here.

C: Rate constant given by $2.0 \times 10^{-11} T_e^{-0.5} T_g^{-1}$ (m³/s).

D: www.lxcat.net, retrieved on November 1, 2017.

E: Assuming a direct dissociation into ground state Oxygen atoms (^{3}P) from electronic states A $^3\Sigma_u^+$, A $^3\Delta_u$ and c $^1\Sigma_u^-$ with threshold energy of 6 (eV).

F: Assuming a direct dissociation into ground state Oxygen atoms from the electronic state B $^3\Sigma_u^-$ with threshold energy of 8.4 (eV).

G: www.lxcat.net, retrieved on August 9, 2018.

H: Rate constant given by 10^{-43} (m⁶/s). M = CO_2, CO, O_2 or O.

The reactions in table 4.4 are: 1) collision processes from a *complete* and *consistent* cross section set for CO_2 (RX1-13), 2) additional processes for CO_2 that make no contribution to equation 4.3 (RX14,15) and 3) elastic scattering and processes leading to electron losses for the other species. An elastic scattering cross section is computed by subtracting the cross sections of inelastic processes (attachment, excitation and ionization) from the effective momentum transfer cross section.

Table 4.5. Vibrational energy transfer reactions. Rate constants in (m^3/s). $M = CO_2$, CO or O_2, unless otherwise stated. The rate constants of reactions RV1 and RV2 are computed from the non-thermal degree of the discharge T_V/T, where T_V is the vibrational temperature (see Modeling results and experimental validation).

No	Reaction	Rate constant	Ref
RV1	$CO_2* + M \rightarrow \nu_l\, CO_2* + (1-\nu_l)\, CO_2 + M$	$f(T_V/T)$	[22]
RV2	$CO_2* + CO_2 \rightarrow \nu_l\, CO_2* + (1-\nu_l)\, CO_2 + CO_2$	$f(T_V/T)$	[22]
RV3	$CO_2\nu_i + M \leftrightarrow CO_2 + M$	$7.14 \times 10^{-14}\exp(-177T^{-1/3} + 451T^{-2/3})$	[31]
RV4	$CO_2\nu_4 + CO_2 \leftrightarrow CO_2 + CO_2$	$0.43 \times 10^{-6}\exp(-407T^{-1/3} + 824T^{-2/3}) +$	[31]
		$0.86 \times 10^{-6}\exp(-404T^{-1/3} + 1096T^{-2/3}) +$	
		$1.43 \times 10^{-11}\exp(-252T^{-1/3} + 685T^{-2/3}) +$	
		$2 \times 2.13 \times 10^{-11}\exp(-242T^{-1/3} + 633T^{-2/3})$	
RV5	$CO_2\nu_4 + M \leftrightarrow CO_2 + M$ (M = CO, O_2)	$0.43 \times 10^{-6}\exp(-407T^{-1/3} + 824T^{-2/3}) +$	[31]
		$0.86 \times 10^{-6}\exp(-404T^{-1/3} + 1096T^{-2/3}) +$	
		$1.43 \times 10^{-11}\exp(-252T^{-1/3} + 685T^{-2/3})$	

Vibrationally excited states created by electron impact reactions are mostly deexcited by collisional processes at moderate and high pressures. In the case of symmetric vibrational states ($CO_2\nu_i$, $i \neq 4$), the deexcitation takes place via Vibrational-Translational (VT) relaxation, i.e. the energy stored in the vibrational degree of freedom is transferred to the translational degree of freedom i.e., as heat. The probability of this energy transfer is highest for processes in which one vibrational quantum is transferred and the rate increases as the vibrational level increases. It is therefore assumed that the process takes place in a cascade fashion and the limiting rate is the VT relaxation of the first symmetric vibrational level. The rate constant of the latter is assumed for the VT relaxation reactions of all symmetric vibrational levels (reaction RV3) and all collision partners M.

For purely asymmetric vibrational levels ($CO_2\nu_4$, CO_2*), the deexcitation takes place via VT relaxation and intermode Vibrational-Vibrational relaxation (VV'), where vibrational energy is transferred to the symmetric vibrational modes.

However, the vibrational relaxation of the symmetric modes is much faster than the same in the asymmetric mode; it is therefore assumed that any symmetric level formed in the VT or VV' relaxation is immediately relaxed. Purely asymmetric vibrational states are thus involved in their vibrational relaxation processes and the VV' relaxation acts as an additional VT relaxation process. Therefore, the rate constant for the reaction RV4 is the sum of the VT and VV' relaxation rate constants of the reference. Specifically, the first three terms in the expression correspond to the VT relaxation reactions $CO_2v_4 + M \leftrightarrow CO_2v_i + M \leftrightarrow CO_2 + M$ with $M = CO_2$ and the symmetric levels CO_2v_1, $CO_2v_{2a} + CO_2v_{2b}$ and CO_2v_3 as respective intermediate states. Reaction RV5 corresponds to the analogous VT relaxation reactions for $M = CO$ and O_2. The last term in the expression for the rate constant of reaction RV4 corresponds to the VV' relaxation reactions $CO_2v_4 + CO_2 \leftrightarrow CO_2v_i + CO_2v_j \leftrightarrow CO_2 + CO_2$ with the symmetric levels CO_2v_1, $CO_2v_{2a} + CO_2v_{2b}$ or $CO_2v_{2a} + CO_2v_{2b}$, CO_2v_1 as intermediate states.

Table 4.6. Reactions between neutral species. Rate constants in (m^3/s) for two-body reactions and (m^6/s) for three-body reactions. $M = CO_2$, CO or O_2. The rate constants of reactions RN3 and RN4 are computed from the non-thermal degree of the discharge T_V/T, where T_V is the vibrational temperature (see Modeling results and experimental validation).

No	Reaction	Rate constant	Ref
RN1	$CO_2 + M \rightarrow CO + O + M$	$4.39 \times 10^{-13}\exp(-65000/T)$	[1]
RN2	$CO_2 + O \rightarrow CO + O_2$	$7.77 \times 10^{-18}\exp(-16600/T)$	[1]
RN3	$CO_2{}^* + M \rightarrow CO + O + M$	$f(T_V/T)$	[22]
RN4	$CO_2{}^* + O \rightarrow CO + O_2$	$f(T_V/T)$	[22]
RN5	$CO + O + M \rightarrow CO_2 + M$	$8.2 \times 10^{-46}\exp(-1510/T)$	[32]
RN6	$CO + O_2 \rightarrow CO_2 + O$	$1.23 \times 10^{-18}\exp(-12800/T)$	[1]
RN7	$O + O + M \rightarrow O_2 + M$	$1.27 \times 10^{-44}(T/300)^{-1}\exp(-170/T)$	[33]

For reactions RV1,2 the rate constants are computed according to the methodology of the reference, i.e. from the state-specific normalized populations and rate constants of the vibrational levels lumped within the fictitious species $CO_2{}^*$. In addition, the symmetric levels are replaced by ground state CO_2 for the reasons previously explained. Rate constants for reverse reactions are computed by using the detailed balancing principle. No reverse reactions are considered for reactions RV1,2 as the highly energetic fictitious species $CO_2{}^*$ can only be produced by electron collisions.

Thermal dissociation of CO_2 takes place through reactions RN1 and RN2, whereas vibrationally enhanced dissociation takes place through the analogous reactions RN3 and RN4. The rate constants for the reactions RN3,4 are computed by following the approach of the given reference. This approach is also used to compute the enthalpy change in these reactions, as exemplified here for RN3. Figure 4.7 illustrates the enthalpy change in the dissociation reaction RN1 for specific levels of the asymmetric vibrational mode of CO_2. For this reaction and this vibrational mode, the vibrational energy decreases the activation energy, which is also the enthalpy change of the reaction.
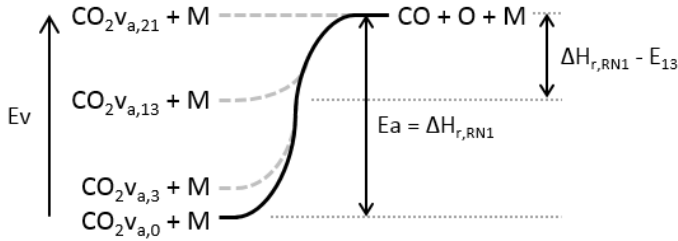

Fig. 4.7. Enthalpy change of the CO_2 dissociation reaction RN1 for selected asymmetric vibrational levels. The energy barrier of the reaction decreases as the vibrational energy increases up to the dissociation limit of 5.5 eV.

The enthalpy change of the lumped reaction RN3 is computed by adding the heat of the dissociation reactions for all asymmetric vibrational levels (grouped inside CO_2^*) and the result is made equal to the heat of reaction of the lumped reaction, as follows.

Reactions of asymmetric levels	Heat of reaction
$CO_2 v_{a,21} + M \rightarrow CO + O + M$	$[CO_2^*] n_{21} [M] k_{RN1,21} (\Delta H_{r,RN1} - E_{21})$
$\vdots$	$\vdots$
$CO_2 v_{a,1} + M \rightarrow CO + O + M$	$[CO_2^*] n_1 [M] k_{RN1,1} (\Delta H_{r,RN1} - E_1)$
$CO_2^* + M \rightarrow CO + O + M$	$[CO_2^*][M] k_{RN3} \Delta H_{r,RN3}$

Therefore, the expression for the enthalpy change of reaction RN3 is

$$\Delta H_{r,RN3} = \frac{\sum n_i k_{RN1,i} (\Delta H_{r,RN1} - E_i)}{\sum n_i k_{RN1,i}} \tag{4.5}$$

The brackets denote concentration, n_i is the normalized population of the asymmetric vibrational level i, k is the rate constant, ΔH_r the enthalpy change and E_i the vibrational energy of the asymmetric vibrational level i. The enthalpy change of reaction RN4 is computed likewise, from its analogous reaction RN2 and considering that only half of the vibrational energy decreases the activation energy [1]. Any vibrational energy surplus in this case becomes heat of the products.

The remaining reactions between neutrals are recombination reactions producing O_2 and CO_2. Reactions involving charged species are limited to three detachment reactions, releasing electrons from the negative ions O^-.

Table 4.7. Reactions involving charged species. Rate constants in (m^3/s). $M = CO_2$, CO or O_2.

No	Reaction	Rate constant	Ref
RI1	$O^- + CO \rightarrow CO_2 + e$	5.5×10^{-16}	[34]
RI2	$O^- + O \rightarrow O_2 + e$	2.3×10^{-16}	[35]
RI3	$O^- + M \rightarrow O + M + e$	4.0×10^{-18}	[36]

Ions can also recover a neutral charge in a collision with a wall, as well as excited states can also return to their ground state through the same action. Given the low temperature of heavy species (neutrals, excited and ions), it is assumed that the probability of this grounding event is 1, i.e. every time an excited or charged species collides with a wall it returns to the neutral ground state. This probability is also referred to as the sticking coefficient and is given in table 4.8 along with the surface reactions of the model. No surface reaction is considered for the negative ions O^- as they are confined in the plasma core due the action of the ambipolar field.

Table 4.8. Surface reactions for excited and charged species.

No	Reaction	Sticking coefficient	Correction factor	Diffusion length
RS1	$CO_{2v_i} \rightarrow CO_2$	1	1	$\Lambda_{eff,cyl}$
RS2	$CO_{2e_i} \rightarrow CO_2$	1	1	$\Lambda_{eff,cyl}$
RS3	$CO_2^+ \rightarrow CO_2$	1	h_l, h_r	N/A

The rate constants can be computed from the sticking coefficients by using the following expression [37]

$$k_s = \left(\frac{1}{1 - \gamma/2}\right)\frac{\gamma}{4}\sqrt{\frac{8RT}{\pi M_n}} \tag{4.6}$$

where γ is the sticking coefficient, the term in parenthesis the Motz-Wise correction for high sticking coefficients and the square rooted term is the thermal velocity of the colliding species. The rate constant for the surface reaction of CO_2^+ is multiplied by a correction factor to take into consideration the effect of ambipolar diffusion (see next section). In the case of neutral species, the total loss rate to the walls is computed from [38]

$$\frac{1}{k_l} = \frac{1}{k_D} + \frac{1}{k_s} \tag{4.7}$$

where k_l is the loss rate, k_D is the diffusion rate of the species to the walls and k_s is the previously defined rate constant for the surface reaction. The loss rate is therefore the contribution of the transport of species to the walls and their reaction when colliding the walls. Naturally, either of these can be the rate limiting step in the process. The diffusion rate is calculated by equation 4.8 as function of the diffusion coefficient of the species k through the mixture, $D_{k,m}$, the effective diffusion length, Λ_{eff}, and the dimension over which diffusion takes place, V/S.

$$k_D = \frac{D_{k,m}}{\Lambda_{eff}^2} \frac{V}{S} \tag{4.8}$$

Surface recombination reactions for neutral species are neglected. The sticking coefficients of these reactions cannot be determined intuitively and are difficult to estimate; they are functions of the gas and wall temperatures and strongly depend on the material of the wall and its surface properties [38]. Experimentally obtained values are also scarce and not in agreement [39,40]. In addition, no significant carbon deposition was observed during the CO_2 dissociation experiments in our setup.

4.3.3. Transport effects

The effects of transport on energy and mass conservation are treated globally. Momentum conservation is not solved for, viscous effects are disregarded and the pressure is assumed uniform and constant throughout the reactor (see figure 4.2 for the negligible pressure loss of order 10^{-3} in the Argon model).

Diffusion effects are only considered for the surface reactions as the concentration of the reacting species at the wall is not equal to their average concentration. Regarding the excited states, the diffusion coefficients $D_{k,m}$ and the effective diffusion length Λ_{eff} are needed to compute their diffusion rates from equation 4.8. The calculation of the former is based on the kinetic gas theory and is included in COMSOL's Plasma Module [25]. The latter, for a cylindrical reactor of length L_r and inner radius r_i can be estimated as follows [41].

$$\frac{1}{\Lambda_{eff,cyl}^2} = \left(\frac{\pi}{L_r}\right)^2 + \left(\frac{2.405}{r_i}\right)^2 \tag{4.9}$$

The positive ion diffuses to the walls at a higher rate due to the action of the ambipolar field. The correction factors h_l, h_r for the surface reaction of CO_2^+ are the wall to center ratios of the species concentration in the z and r dimensions, respectively, and are computed, based on [42], from

$$h_l = \frac{n_{l/2}}{n_0} \approx \frac{0.86}{(3 + L_r/2\lambda_i + (0.86 L_r u_B/\pi D_a)^2)^{1/2}} \tag{4.10}$$

$$h_r = \frac{n_r}{n_0} \approx \frac{0.8}{(4 + r_i/\lambda_i + (0.8 r_i u_B/2.405 J_1(2.405) D_a)^2)^{1/2}} \tag{4.11}$$

In the above expressions, J_1 is the Bessel function of the first order, λ_i is the ion-neutral mean free path, u_B the Bohm velocity and D_a the ambipolar diffusion coefficient, computed as follows

$$\lambda_i = \frac{1}{n_g \sigma_i} \tag{4.12}$$

$$u_B \approx \sqrt{\frac{e T_e}{M}} \tag{4.13}$$

$$D_a \approx D_{CO_2^+,m}\left(1 + \frac{T_e}{T}\right) \tag{4.14}$$

where n_g is the density of neutrals, σ_i the total ion-neutral collisional cross section and M the mass of the ion. An average and constant value of 10^{-18} m^2 is assumed for this cross section, which is within the typical range of values for CO_2^+ transport

in its parent gas [43]. Moreover, it is also assumed that all heavy species are in thermal equilibrium (share the same temperature) and the electronegativity of the discharge is very low $\alpha = n_{O^-}/n_e \ll 1$ and hence the plasma behaves similar to an electropositive discharge.

Regarding heat transfer, it is assumed that heat conduction is the dominant heat transfer mechanism in the plasma [44]. The heat transfer equation therefore corresponds to that of a cylinder with heat generation inside and a constant wall temperature. It can be easily shown than in this case a parabolic temperature profile is obtained and the heat losses and maximum temperature are

$$Q_{loss} = 8\lambda_{mix}\frac{T - T_w}{r_i^2} \tag{4.15}$$

$$T_{max} = 2T - T_w \tag{4.16}$$

where λ_{mix} is the thermal conductivity of the gas mixture, computed from the species' mole fractions and thermal conductivities [25], which in turn are computed from the Stiel-Thodos equation [45].

The heat losses are included in the following heat transfer equation to calculate the temperature of the gas in the plasma

$$\rho c_{p,mix}\frac{dT}{dt} = Q_{gen} - Q_{loss} \tag{4.17}$$

where ρ is the gas density, $c_{p,mix}$ the specific heat at constant pressure of the gas mixture and Q_{gen} the heat source from reactions. The internal energy lost to the walls by the excited species is normalized per unit volume and added to the heat source from gas phase reactions. Likewise, the ionization energy of the positive ions is also added.

The acceleration induced by the ambipolar field leads to higher kinetic energies in the positive ions. This kinetic energy is $\varepsilon_i = V_s + 0.5T_e$, with the sheath voltage V_s computed as in [38]

$$V_s = T_e\ln\sqrt{\frac{M}{2\pi m_e}} \tag{4.18}$$

where m_e is electron mass. Additionally, to preserve the electroneutrality in the plasma, an electron is also lost each time a positive ion is neutralized or "lost" to the walls. The kinetic energy lost per Maxwellian electron is $\varepsilon_e = 2T_e$. The sum of these kinetic energies $(\varepsilon_i + \varepsilon_e)$ is also normalized per unit volume and is added to Q_{gen}. This approach ensures that the energy from the microwaves not used in chemical reactions ends up as heat in the plasma.

The contribution of the asymmetric vibrational states to the specific heat of the fictitious species CO_2* is computed from their vibrational energy. The following equations are used for the calculation

$$\frac{C_{P,vib}}{R} = \frac{C_{V,vib}}{R} + 1 \tag{4.19}$$

$$C_{V,vib} = \left(\frac{\partial E_{vib}}{\partial T}\right)_V \tag{4.20}$$

$$E_{vib} = \frac{\sum n_i E_i}{\sum n_i} \tag{4.21}$$

where $C_{P(V),vib}$ is the contribution of the asymmetric vibrational mode to the molar specific heat at constant pressure (volume) of CO_2*, R the universal gas constant, E_{vib} the mean vibrational energy, and n_i and E_i are the population and vibrational energy of the level i, respectively. The reader is referred to [22] for the details regarding the calculation of the energies and populations of the vibrational levels grouped within CO_2*. The calculation of the enthalpy change in deexcitation reactions of CO_2* is performed using the computed specific heat for this species.

4.4. Modeling results and experimental validation

The simplified profile used as input for the CO_2 model is shown in figure 4.8. This profile is based on figure 4.3 and consists of three peaks of the same magnitude distributed uniformly inside the Surfatron body and a declining power density downstream. The plasma obtained in the CO_2 experiments is shorter than the Argon plasma at the same process conditions, with a total length of approximately 20 cm [12,13]. Assuming this value for the plasma length as well as deposition efficiencies of 62% inside the Surfatron body and 21% for the surface wave (refer to table 4.1, the value corresponding to $T_W = 600$ K is assumed for the former), the piecewise linear profile is calculated using equation 4.1. It is also assumed that the

power deposition starts inside the Surfatron body and the profile remains constant within the range of studied flowrates as it was observed in the Argon model.
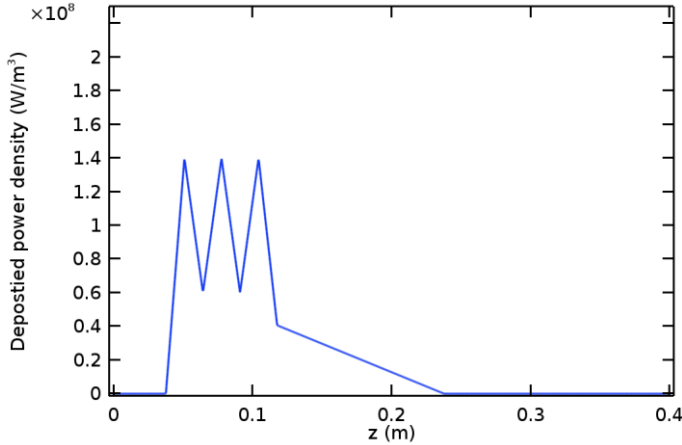

Fig. 4.8. Deposited power density profile for the CO_2 model. Refer to figure 4.3 for the power density profile obtained with the Argon model.

The simulations in the CO_2 model are performed at the same process conditions of the experiments for three different values of the inlet flowrate, 100, 200 and 300 sccm. The pressure is fixed at 20 mbar, the initial (inlet) temperature and the wall temperature are both 300 K and the input power is 150 W. CO_2 is ~100% of the initial composition and the initial mass fractions of the excited species are computed by assuming a Boltzmann distribution. In addition, thermal equilibrium is initially assumed for the electrons and the initial ionization degree (electrons to neutrals ratio) is 10^{-10}. A direct solver is used for the fully coupled system of equations and the solution time is optimized using Anderson acceleration with a dimension of iteration space of 10.

The CO_2 conversion in the plasma reactor as a function of the axial position can be computed with the following expression, where n_{CO_2} is the total density of the CO_2 species and v is the flow velocity.

$$X(z) = 1 - \frac{n_{CO_2}(z)v(z)}{n_{CO_2}(0)v(0)} \tag{4.22}$$

Several reactions in the model can contribute to the dissociation of the CO_2 molecule. These can be arranged into 5 different paths:

1. Dissociative attachment (RX2, table 4.4).
2. Ionization + dissociative recombination (RX13 + RX16, table 4.4).
3. Direct electron impact dissociation (RX15, table 4.4).
4. Thermal dissociation (RN1,2, table 4.6).
5. Vibrationally enhanced dissociation (RX14a, table 4.4 + RN3,4, table 4.6).

The dashed lines in figure 4.9 show the CO_2 conversion computed when the vibrationally enhanced dissociation of CO_2 is not considered. In this case, the conversion at the reactor outlet ($x = 0.4$ m) is 11%, 16% and 31% for 300, 200 and 100 sccm, respectively. In these calculations the direct electron impact dissociation is the dominant path, forming approximately 92% of CO. Dissociative recombination after ionization and dissociative attachment also contribute, forming 5.5% and 2.5% of CO, respectively. Thermal dissociation is orders of magnitude smaller than the other paths due to the relatively low temperatures in the plasma.
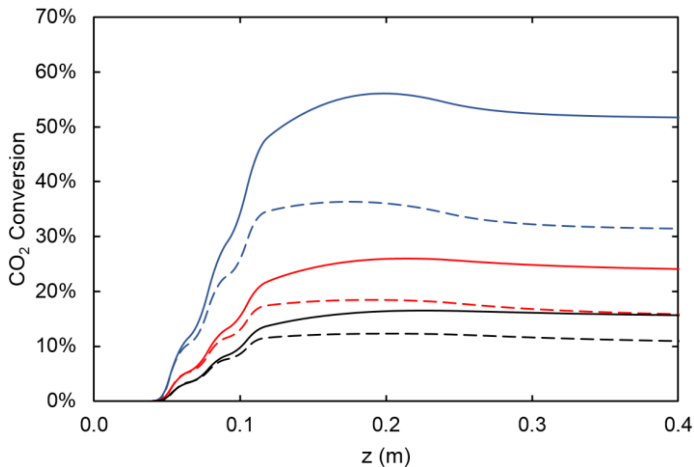

Fig. 4.9. CO_2 conversion as a function of the axial position in the reactor for 100 (blue), 200 (red) and 300 sccm (black). Results ignoring the vibrationally enhanced CO_2 dissociation are shown in dashed lines. The solid lines correspond to the full model, including the fictitious species CO_2* and its reactions. In all cases, the CO_2 recombination from $x = 0.4$ m until the measuring device located at $x = 2.9$ m is estimated to be less than 1%.

These conversion values are clearly far from the experimental values of 18%, 32% and 66% obtained for the same flowrates, indicating that the vibrationally enhanced dissociation could play a significant role in the dissociation of CO_2. It is worth

mentioning that the CO_2 recombination from the reactor outlet to the measuring device is, in all cases, estimated to be less than 1% and is therefore neglected. Hereinafter, conversion refers to the conversion at the outlet of the reactor unless otherwise stated.

It is possible to estimate the CO_2 dissociation via vibrational excitation by including the fictitious species CO_2^* in the model. The stoichiometric coefficients, reaction rates, enthalpy of reactions and specific heat required to include this species in the model are computed from the non-thermal degree by following the methodology presented in [22] (see previous sections 4.3.2 and 4.3.3). This reduction methodology is based on 1) lumping all asymmetric vibrational levels within the fictitious species CO_2^*, 2) assuming a Treanor distribution of these levels, 3) using an algebraic approximation based on the Landau-Teller formula to compute the evolution of non-thermal degree in the discharge and 4) employing weighted algebraic expressions to compute the rate constants of reactions involving CO_2^*. The application of this methodology results in a substantial simplification regarding the number of reactions and species required to describe the vibrationally enhanced dissociation of CO_2.

The non-thermal degree is an implicit comparison between VV and VT relaxation and is given by the ratio between the vibrational temperature T_V and the gas temperature T. The vibrational temperature is based on the population density of the first vibrational level of the asymmetric mode and is computed from $T_V = E_1/\ln(n_0/n_1)$. An efficient dissociation of CO_2 is possible at low temperatures and high non-thermal degrees, when the vibrational energy is predominantly exchanged between vibrational levels (VV relaxation) instead of being lost as heat (VT relaxation).

The CO_2 model without the fictitious species CO_2^* is used to estimate the non-thermal degree at the characteristic time of the VT relaxation, i.e. the time at which VT relaxation kicks in and the evolution of T_V/T follows the trend described in [22]. This characteristic time is approximately 1.6×10^{-4} s and it is computed at the initial conditions of the discharge from $\tau_{VT} = \left(k_{RV4} n_{CO_2}\right)^{-1}$, where k_{RV4} is the rate constant of the VT relaxation reaction RV4 and n_{CO_2} is the population density of CO_2. The non-thermal degree is then computed at 1.6×10^{-4} s after the power

deposition starts, giving the approximate values of 3.5, 3.1 and 2.6 for 300, 200 and 100 sccm, respectively.

The results of the full model, including CO_2*, are shown in the solid lines of figure 4.9. The conversion in the plasma reactor is now 16%, 24% and 52% for 300, 200 and 100 sccm, respectively. The absolute increase in the conversion by considering the vibrationally enhanced dissociation is 5%, 8% and 21%, which also correspond to a relative increase of 45%, 50% and 68%, respectively. These numbers confirm that this path plays a significant role and must be considered when modeling the CO_2 dissociation in non-thermal plasmas. In these calculations, the dominant paths for the dissociation are now the direct electron impact dissociation and the vibrationally enhanced dissociation. The dissociative recombination after ionization and dissociative attachment also have minor contributions, whereas thermal dissociation is still negligible.

Table 4.9 gives the percentage of CO molecules formed by each of the dissociation paths. The direct electron impact dissociation accounts for approximately 55% of the dissociation, while 40% is due to the vibrationally enhanced dissociation. Although not shown in the table, there is an absolute increase in the dissociation for each path as the flowrate decreases, due to an increase in the electron density. However, the dissociation rate for all paths increase differently as the electron temperature increases, modifying the rate constant of the electron impact reactions.

Table 4.9. Percentage of CO molecules formed per CO_2 dissociation path. Thermal dissociation is orders of magnitude smaller due to the low temperatures of the discharge and is therefore not shown.

Flowrate	CO_2 Dissociation path			
	1	2	3	5
(sccm)	DA	I + DR	DEID	VED
100	1.4%	3.0%	53.2%	42.4%
200	1.5%	2.8%	54.0%	41.7%
300	1.6%	2.8%	56.2%	39.4%

The conversions obtained with the full model are still lower than the experimental values, having relative errors of 11%, 25% and 21%. These deviations can be seen in figure 4.10, where the experimental and modeling results are plotted as functions of the flowrate. Given the complexity of modeling plasma and the simplifications taken in the process, the results are considered in fair agreement. Indeed, various

elements have influence on the lower conversions obtained in the model, particularly the power deposition. The power deposition efficiencies were characterized from a model of an atomic plasma and are assumed to remain the same for a molecular plasma. However, this is not necessarily true since molecules have more degrees of freedom and have chemical bonds that can be broken (or formed); therefore, molecular plasmas are more reactive and have more energy channels through which the energy given by the electrons can flow or be stored. In other words, this means that the power deposition in the CO_2 plasma is expected to be higher than the value taken from the Argon model. The calculation of a correction factor for the power deposition in the CO_2 plasma can be problematic due to the complexity of the physics involved in the 2D self-consistent model, e.g. the electromagnetic wave equation inside and outside of the reactor. The formulation of the power deposition depends on the type discharge and the presence of electric arcs can simplify the treatment [46].
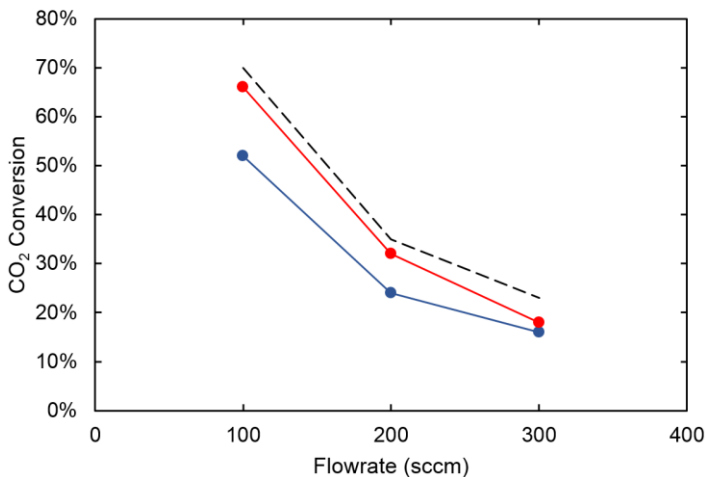

Fig. 4.10. CO_2 conversion as a function of the flowrate. Red: experimental results, blue: full model simulation results. The dashed line shows the limiting case for the maximum conversion assuming 100% of deposited power and 75% of deposited power inside the Surfatron body.

The dashed line of figure 4.10 illustrates the influence of the deposition efficiencies in the conversion. For these calculations, it is assumed that all 150 W of power input are deposited in the plasma, with 75% of it being deposited inside the Surfatron body (approximate ratio of 62/83). The non-thermal degrees are kept constant, implying that these conversions are slightly underestimated. Nevertheless, these results serve as a limiting case, proving that this uncertainty

alone can explain the lower conversions in the model. It is to be noted that the power deposition remains lower than 100% in the CO_2 plasma. As we proved experimentally, the addition of a waveguide reduces the power losses and increases the performance of the reactor for the case of CO_2 reduction with hydrogen [13].
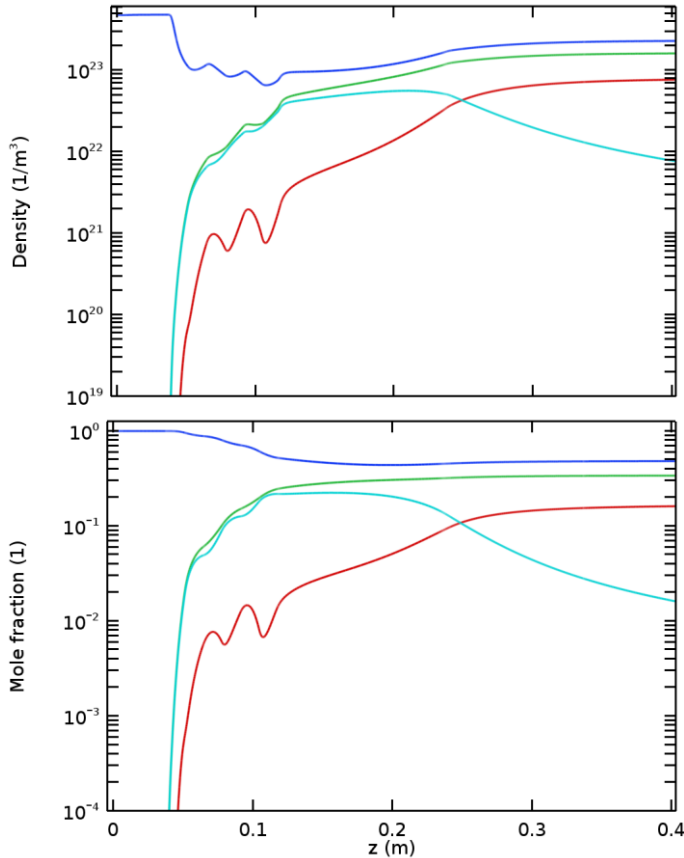

Fig. 4.11. Densities (top) and mole fractions (bottom) of neutral species as functions of the axial position in the reactor for a flowrate of 100 sccm. Blue: CO_2, green: CO, cyan: O, red: O_2.

The portion of power deposited inside the Surfatron body can also vary, having further influence on the conversion, as most of the CO_2 dissociation takes place there. Figure 4.11 shows the densities and mole fractions of the neutral species as functions of the axial position in the plasma reactor. The oscillations seen in the graph at the top are partially caused by expansions due to the increase in the gas temperature when power is deposited. This effect is not present in the mole fractions shown in the graph at the bottom, where the remaining fluctuations are

then related to the reacting system. In the bottom graph, it is seen that most of the CO_2 dissociation takes place inside the Surfatron body, forming mainly CO and O. O_2 is subsequently formed by the recombination of two O atoms, or in the reaction of CO_2* and O.

The fluctuations still seen in O_2 are located at the peaks of the power deposition profile and are related to electron impact dissociation reactions of O_2. The maximum dissociation of CO_2, corresponding to a maximum conversion of 56%, is slowly reached downstream of the Surfatron; afterwards, recombination takes place and the final conversion of 54% is achieved. O atoms also recombine into O_2 downstream of the Surfatron, notably past the end of the plasma. The final products are then CO_2, CO and O_2, as expected.

The energy efficiency of the reactor can be computed from the CO_2 conversion, considering that a minimum of 2.93 eV per CO_2 molecule are required for the reaction $CO_2 \rightarrow CO + 1/2\,O_2$ to take place. The energy input per particle in the plasma, commonly known as Specific Energy Input (SEI), is also used in the calculation, as follows

$$\eta = X\frac{2.93}{\text{SEI}} \tag{4.23}$$

$$\text{SEI} = \frac{P_{dep}M_{n,inlet}}{eN_A\dot{m}} \tag{4.24}$$

where $M_{n,inlet}$ is the mean molar mass at the inlet (44.01 kg/kmol for CO_2), N_A is the Avogadro constant and $\dot{m}$ is the mass flowrate. The energy efficiencies calculated with the model are in agreement with the experimental values; the results are presented in table 4.10.

Table 4.10. Energy efficiency of the plasma reactor for the considered flowrates. The experimental values are taken from [12], where a power deposition of 150 W is assumed.

Flowrate (sccm)	SEI, model (eV/molecule)	E. Efficiency, model (%)	E. Efficiency, exp. (%)
100	17.3	8.8	8.3
200	8.7	8.1	8.3
300	5.8	7.9	6.8

Assuming 100% of power deposition in the model, as before, the energy efficiencies for the same flowrates increase to approximately 10%, which is still a low value. The reason for this is that the experimental conditions and the reactor itself were not optimized for an efficient dissociation of CO_2, which is achieved at low values of SEI (<2 eV/molecule). At high values of the SEI, such as the ones in table 4.10, relatively high electron densities and electron temperatures are obtained, shifting the EEDF away from the vibrational excitation reactions. An efficient dissociation of CO_2 should take place mostly through vibrational excitation, not direct electron impact dissociation with a higher energy requirement. As mentioned before, the latter is the main dissociation path in the Surfatron reactor, leading to low energy efficiencies.

The effect of the SEI is clearly seen in the top and middle graphs of figure 4.12, showing that both the electron density and electron temperature increase as the SEI increases (flowrate decreases). Nonetheless, the results for the different flowrates are quite similar and within the range of typical values for non-thermal CO_2 microwave plasmas: $T_e \approx 0.5 - 2$ eV and $n_e \approx 10^{18-20}$ $1/m^3$. The ionization degree in the plasma is then 10^{-5} inside the Surfatron body and 10^{-6} outside.

Experimental values of the electron density and electron temperature in this reactor were determined downstream of the Surfatron for gas mixtures of H_2 and CO_2 [12]. Electron densities in the order of 10^{21} and 10^{20} $1/m^3$ were estimated for H_2:CO_2 ratios of 4 and 3, respectively. Likewise, electron temperatures of 1.3 and 0.7 eV were estimated for H_2:CO_2 ratios of 3 and 1, respectively. Lower electron densities and temperatures are expected for lower mixing ratios [11]. These reference values suggest that the computed electron densities are within the expected order of magnitude while the electron temperatures are slightly overestimated (see below discussion on lack of electron transport).

A qualitative match between figure 4.1 and figure 4.12 is also observed, confirming that these variables follow the power deposition profile. Therefore, given that the variables in figures 4.1 and 4.12 determine the rate of the electron impact reactions, it can be inferred that not only the deposited power, but also the density at which it is deposited has an influence on the results.
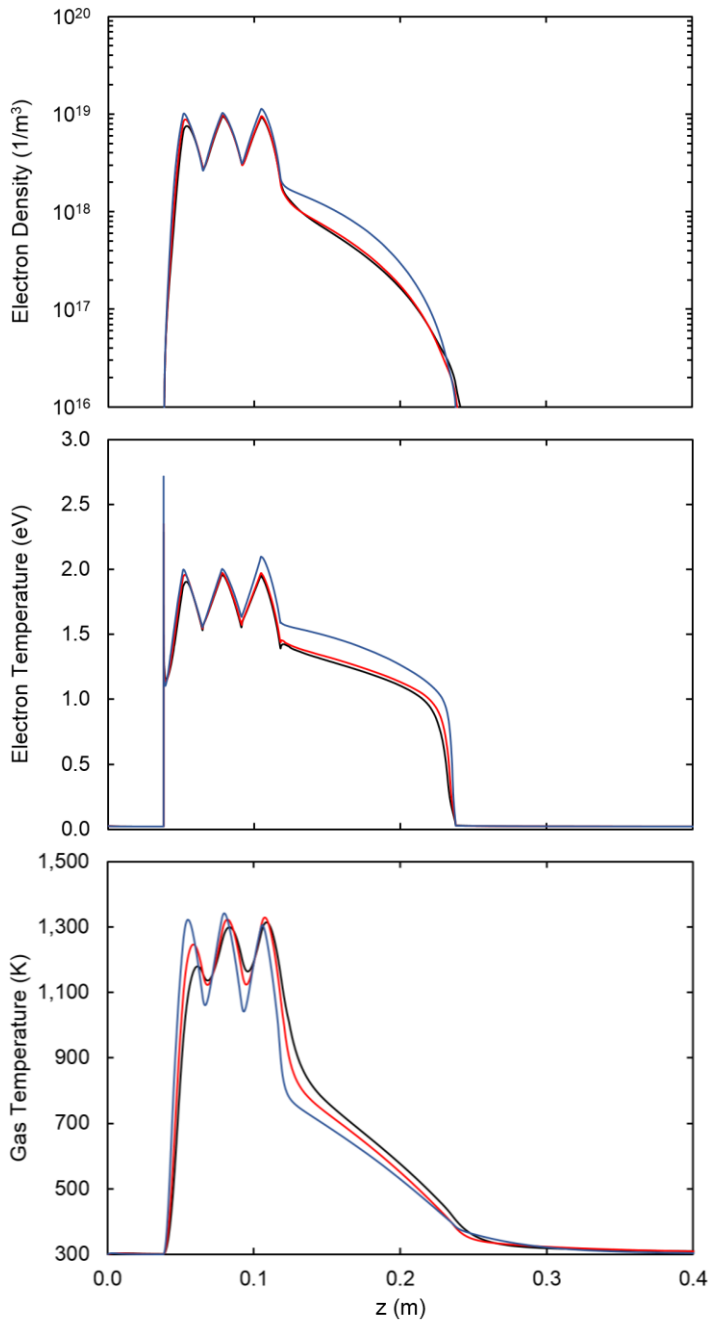
Fig. 4.12. Electron density (top), electron temperature (middle) and gas temperature (bottom) as a function of the axial position in the reactor for 100 (blue), 200 (red) and 300 sccm (black).

The lack of electron transport in the CO_2 model is also evident by comparing the electron densities and electron temperatures of figure 4.1 and figure 4.12. In the Argon model, a smaller difference is seen between the values inside and outside of the Surfatron body. Furthermore, the slope at which they decrease in the low power density zone is flatter, being virtually horizontal for the electron temperature. Thus, the lack of electron transport in the CO_2 model results in a less uniform plasma with a reduced reactivity due to the rapid decay in the number of electrons.

The average gas temperature, shown at the bottom of figure 4.12, does not vary much with the flowrate, except in the first and last peaks of the power deposition. The variations seen in the first peak are related to the electron density, while the CO_2 dissociation explains the variations in the last peak. The CO_2 dissociation is also related to the electron temperature and density variations seen for a flowrate of 100 sccm in figure 4.12.

Despite the variations, the maximum average temperature for the flowrates is the same, reaching around 1300 K inside the Surfatron body. Hence, according to equation 4.16, the maximum gas temperature at the center of the plasma is 2300 K, which is within the range of our previously estimated values for the gas temperature, 2200 - 2400 K [12].

It is also possible to verify the previous assumption regarding the electropositive behavior of the plasma. Figure 4.13 shows that the maximum electronegativity is around 0.2 as the power deposition begins. However, it promptly decays and for most of the plasma, it is in the order of magnitude of 10^{-3}, which agrees with the assumption of a very low electronegativity ($\alpha = n_{O^-}/n_e \ll 1$). This means that there are few negative ions, which are confined at the core of the plasma and their effect on the positive ions can be neglected.

Even though the positive ions are not held back in their movement towards the walls, the rate of surface recombination is two orders of magnitude smaller than the collisional counterpart (dissociative recombination, RX16 table 4.4). Thus, most electrons are lost inside the plasma instead of being lost to the walls.
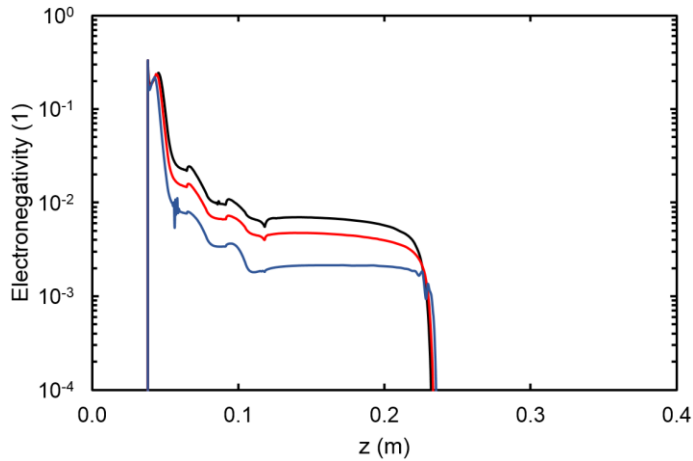
Fig. 4.13. Electronegativity as a function of the axial position in the reactor for 100 (blue), 200 (red) and 300 sccm (black).

Contrarily, the rates of collisional and surface deexcitation of vibrationally excited species are comparable, with the surface process becoming more important as the vibrational level increases due to the limiting rate assumed for the collisional process. Moreover, the reverse collisional process intensifies the relevance of the surface deexcitation, making its contribution to vibrational deexcitation larger than the collisional counterpart.

The importance of surface reactions in this model is expected from the characteristic diffusion time, which, depending on the computed gas temperature, is estimated in the order of 0.1 - 1 ms. This characteristic time is shorter than the residence time in the plasma reactor, which for 20 cm of plasma is approximately 3.7, 5.7 and 11.6 ms for 300, 200 and 100 sccm, respectively. Therefore, for such a small reactor and relatively low operating pressure, the species have sufficient time to diffuse and possibly collide with the walls.

For larger reactors, the surface reactions can be neglected considering that their rates scale as $1/r$ compared to the gas phase reactions. In addition, longer characteristic diffusion times are also obtained and fewer species would reach the walls during the short residence times in the reactor.

4.5. Conclusions

We have developed a two-step modeling approach for plasma reactors, consisting of a plasma characterization step using simple chemistry and a global modeling step using the actual chemistry of interest. Specifically, in the first step, we used a self-consistent two-dimensional axisymmetric Argon plasma model of a laboratory surface wave microwave plasma reactor to characterize the discharge, particularly the power deposition along the reactor. In the second step, the outcome of the first step was used to develop a zero-dimensional volume-averaged CO_2 plasma model, under a Lagrangian description, which represents a one-dimensional model of our experimental setup.

With the global model we showed that the vibrationally enhanced dissociation is a relevant process taking place in the reactor and must be included in the model. For this purpose, we have used the fictitious species CO_2* that groups all levels in the asymmetric vibrational mode of the CO_2 molecule. We also pointed out the significant role of the surface reactions in the deactivation of excited species at the investigated conditions in our plasma reactor. The relevance of the surface reactions should be evaluated according to the reactor design and operating conditions before deciding whether to include them in the modeling process.

The results of the simulations showed CO_2 conversions of 16%, 24% and 52%, for inlet flowrates of 300, 200 and 100 sccm, respectively. The relative increase in the conversion when the vibrationally enhanced dissociation is considered was 45%, 50% and 68%, respectively. With the model we also identified the direct electron impact dissociation and the vibrationally enhanced dissociation as the dominant paths for the CO_2 dissociation in our plasma reactor, accounting for approximately 55% and 40% of CO formation, respectively.

The experimental conversions for the corresponding flowrates of 300, 200 and 100 sccm are 18%, 32% and 66%, respectively. Thus, the agreement between the modeling and experimental values, mentioned in the previous paragraph, is good in view of the complexity involved in modeling non-thermal CO_2 plasma reactors. The experimental validation of the CO_2 plasma variables indicates that the electron densities are close to the expected order of magnitude and the gas temperature is in agreement with the experimentally estimated values. The electron temperatures are

slightly overestimated, mainly due to the lack of electron transport in the global model.

The power deposition profile determined with the Argon model was identified as the major source of error, due to the uncertainty of its variation when the plasma is generated in a CO_2 flow, e.g. higher power depositions are expected in a molecular plasma. Despite this, the profile obtained from the Argon model was adopted as it is more descriptive than a power input value and closer to reality than an arbitrarily shaped profile. Using the Argon model, it was determined that 17% of the power input is lost to the surroundings and the remaining power is deposited into the plasma. Moreover, it was identified that 75% of the power deposition occurs inside the Surfatron body, whereas 25% is gradually deposited by the surface waves as they travel axially along the plasma.

Additional simulations showed that the uncertainties regarding the power deposition profile can explain the error obtained in the CO_2 conversion. It is therefore essential to have an approximate description of the power deposition profile, including the deposited power inside the Surfatron reactor, the power of the surface wave, the length of the plasma and the power deposition densities (shape of the profile). It was also shown with both models that the latter can be particularly important as the plasma variables have a fast response and closely follow the same variations.

Further limitations of the global model were also discussed, especially those that can contribute to the discrepancies in the results. Among these are the simplified treatment of the heat transfer inside the reactor body, the simplified treatment of the heat and mass transfer in the radial direction (due to averaging) and the lack of heat and mass transfer (plug flow assumption) in the axial direction (due to the Lagrangian approach).

Despite these limitations, we believe that the two-step modeling approach is valuable for process engineering applications involving design, optimization and verification of plasma reactors and their performance.

References

1 A. Fridman, *Plasma chemistry*, Cambridge University Press, 2008.

2 V. D. Rusanov, A. a. Fridman and G. V. Sholin, *Uspekhi Fiz. Nauk*, 1981, **134**, 185.

3 M. Capitelli, M. Dilonardo and E. Molinari, *Chem. Phys.*, 1977, **20**, 417–429.

4 M. Capitelli, C. M. Ferreira, B. F. Gordiets and A. I. Osipov, *Plasma Kinetics in Atmospheric Gases*, Springer Berlin Heidelberg, Berlin, Heidelberg, 2000, vol. 31.

5 R. Snoeckx and A. Bogaerts, *Chem. Soc. Rev.*, 2017, **46**, 5805–5863.

6 T. Kozák and A. Bogaerts, *Plasma Sources Sci. Technol.*, 2014, **23**, 045004.

7 T. Kozák and A. Bogaerts, *Plasma Sources Sci. Technol.*, 2015, **24**, 015024.

8 L. D. Pietanza, G. Colonna, G. D'Ammando, A. Laricchiuta and M. Capitelli, *Plasma Sources Sci. Technol.*, 2015, **24**, 042002.

9 L. D. Pietanza, G. Colonna, G. D'Ammando, A. Laricchiuta and M. Capitelli, *Phys. Plasmas*, 2016, **23**, 013515.

10 M. Grofulović, L. L. Alves and V. Guerra, *J. Phys. D. Appl. Phys.*, 2016, **49**, 395207.

11 P. Diomede, M. C. M. van de Sanden and S. Longo, *J. Phys. Chem. C*, 2017, **121**, 19568–19576.

12 J. F. de la Fuente, S. H. Moreno, A. I. Stankiewicz and G. D. Stefanidis, *Int. J. Hydrogen Energy*, 2016, **41**, 21067–21077.

13 J. F. de la Fuente, S. H. Moreno, A. I. Stankiewicz and G. D. Stefanidis, *Int. J. Hydrogen Energy*, 2017, **42**, 12943–12955.

14 W. Bongers, H. Bouwmeester, B. Wolf, F. Peeters, S. Welzel, D. van den Bekerom, N. den Harder, A. Goede, M. Graswinckel, P. W. Groen, J. Kopecki, M. Leins, G. van Rooij, A. Schulz, M. Walker and R. van de Sanden, *Plasma Process. Polym.*, 2017, **14**, 1600126.

15 T. Silva, N. Britun, T. Godfroid and R. Snyders, *Plasma Sources Sci. Technol.*, 2014, **23**, 025009.

16 L. F. Spencer and A. D. Gallimore, *Plasma Sources Sci. Technol.*, 2013, **22**, 015019.

17 B. L. M. Klarenaar, M. Grofulović, A. S. Morillo-Candas, D. C. M. van den Bekerom, M. A. Damen, M. C. M. van de Sanden, O. Guaitella and R. Engeln, *Plasma Sources Sci. Technol.*, 2018, **27**, 045009.

18 B. Hrycak, M. Jasiński and J. Mizeraczyk, *Acta Phys. Pol. A*, 2014, **125**, 1326–1329.

19 M. Jasiński, M. Dors and J. Mizeraczyk, *Int. J. Plasma Environ. Sci. Technol.*, 2008, **2**, 134–139.

20 L. M. Martini, S. Lovascio, G. Dilecce and P. Tosi, *Plasma Chem. Plasma Process.*, 2018, **38**, 707–718.

21 L. M. Martini, N. Gatti, G. Dilecce, M. Scotoni and P. Tosi, *Plasma Phys. Control. Fusion*, 2018, **60**, 014016.

22 J. F. de la Fuente, S. H. Moreno, A. I. Stankiewicz and G. D. Stefanidis, *React. Chem. Eng.*, 2016, **1**, 540–554.

23 M. Jimenez-Diaz, E. a D. Carbone, J. van Dijk and J. J. a M. van der Mullen, *J. Phys. D. Appl. Phys.*, 2012, **45**, 335204.

24 M. Selby and G. M. Hieftje, *Spectrochim. Acta Part B At. Spectrosc.*, 1987, **42**, 285–298.

25 COMSOL, *Plasma Module User's Guide*, COMSOL 5.3, 2017.

26 L. S. Polak and D. I. Slovetsky, *Int. J. Radiat. Phys. Chem.*, 1976, **8**, 257–282.

27 R. E. Beverly, *Opt. Quantum Electron.*, 1982, **14**, 501–513.

28 *Phelps database, www.lxcat.net, retrieved on October 24*, 2017.

29 L. L. Alves, *J. Phys. Conf. Ser.*, 2014, **565**, 012007.

30 H. Shields, A. L. S. Smith and B. Norris, *J. Phys. D. Appl. Phys.*, 1976, **9**, 1587–1603.

31 J. A. Blauer and G. R. Nickerson, *A survey of vibrational relaxation rate data for processes important to CO2–N2–H2O infrared plume radiation*, Irvine, California, 1973.

32 A. Cenian, A. Chernukho, V. Borodin and G. Śliwiński, *Contrib. to Plasma Phys.*, 1994, **34**, 25–37.

33 S. Hadj-Ziane, B. Held, P. Pignolet, R. Peyrous and C. Coste, *J. Phys. D. Appl. Phys.*, 1992, **25**, 677–685.

34 T. G. Beuthe and J.-S. Chang, *Jpn. J. Appl. Phys.*, 1997, **36**, 4997–5002.

35 J. T. Gudmundsson and E. G. Thorsteinsson, *Plasma Sources Sci. Technol.*, 2007, **16**, 399–412.

36 H. Hokazono and H. Fujimoto, *J. Appl. Phys.*, 1987, **62**, 1585–1594.

37 R. J. Kee, M. E. Coltrin and P. Glarborg, *Chemically Reacting Flow*, John Wiley & Sons, Inc., Hoboken, NJ, USA, 2003.

38 M. A. Lieberman and A. J. Lichtenberg, *Principles of Plasma Discharges and Materials Processing*, John Wiley & Sons, Inc., Hoboken, NJ, USA, 2005.

39 A. F. Kolesnikov, I. S. Pershin, S. A. Vasil', evskii and M. I. Yakushin, *J. Spacecr. Rockets*, 2000, **37**, 573–579.

40   N. G. Bykova, S. A. Vasil'evskii, A. N. Gordeev, A. F. Kolesnikov, I. S. Fershin and M. I. Yakushin, *Fluid Dyn.*, 1997, **32**, 876–886.

41   P. J. Chantry, *J. Appl. Phys.*, 1987, **62**, 1141–1148.

42   C. Lee and M. A. Lieberman, *J. Vac. Sci. Technol. A Vacuum, Surfaces, Film.*, 1995, **13**, 368–380.

43   L. A. Viehland and E. A. Mason, *At. Data Nucl. Data Tables*, 1995, **60**, 37–95.

44   C. M. Ferreira, B. F. Gordiets and E. Tatarova, *Plasma Phys. Control. Fusion*, 2000, **42**, B165–B188.

45   L. I. Stiel and G. Thodos, *AIChE J.*, 1964, **10**, 26–30.

46   G. Trenchev, S. Kolev, W. Wang, M. Ramakers and A. Bogaerts, *J. Phys. Chem. C*, 2017, **121**, 24470–24479.

5

CONCLUSIONS AND OUTLOOK

5.1. Conclusions

The non-thermal plasma reactor technology was investigated from a process engineering perspective, taking the CO_2 dissociation in a non-thermal microwave plasma reactor as the case study. Outcome of this research are a reduction methodology for vibrational kinetics and a two-step modeling approach for non-thermal plasma reactors, both intended for engineering purposes.

VV relaxation is the fastest process and VT relaxation is the slowest process throughout the typical conditions used for CO_2 dissociation in non-thermal microwave plasmas, i.e. high electron densities and low electron and gas temperatures. It was shown that Treanor-like vibrational distribution functions can be obtained even if VT relaxation is included in the calculations. Indeed, even at high gas temperatures, the relaxation of symmetric sublevels slows down the relaxation of asymmetric levels and can lead to Treanor-like vibrational distribution functions and high vibrational temperatures.

The vibrational temperature may increase with the gas temperature, but at the studied conditions, their ratio decreases with increasing gas temperatures. Indeed, the vibrational-to-translational temperature ratio becomes 1 above certain values of gas temperature, when VT relaxation dominates and no vibrational excitation is attained. At high electron densities, the limit at which this ratio becomes 1 is when thermal equilibrium is reached and the plasma is characterized by a single temperature. It was demonstrated that the behavior of the temperature ratio with increasing gas temperatures can be fitted to an algebraic expression that incorporates the Landau-Teller temperature dependence of VT relaxation. This expression was used to approximate the evolution of the temperature ratio with increasing gas temperatures and dramatically reduce the vibrational kinetics of CO_2 in non-thermal microwave plasma.

The methodology for the reduction of vibrational kinetics exploits the wide difference in the timescales of the plasma processes, especially at low gas temperatures. The processes are thus divided into the very fast (immediate) VV relaxation and the slower competing processes that take place at longer, but yet comparable timescales. The expression for the temperature ratio is used to update its value at the longer timescales as VT relaxation proceeds and the gas

temperature increases. The wide difference in timescales and the long timescale behavior of the temperature ratio are the pillars of the reduction methodology.

The four key elements of the reduction methodology, exemplified for CO_2, are 1) the asymmetric vibrational levels are lumped within a single group, or fictitious species, CO_2^*, 2) this group follows the Treanor distribution, 3) an algebraic expression is used to approximate the temperature ratio and 4) weighted algebraic rate constants are employed for reactions involving CO_2^*. It was shown that by using this methodology the reaction kinetics are captured in a reduced set of 44 reactions among 13 species, as opposed to the benchmark STS kinetic model, in which +100 species and +10000 reactions are considered. Such drastic simplifications of complex plasma chemistries are needed to enable their implementation in practical engineering models that consider dimensionality and transport.

Qualitative analysis of the key parameters in the reduction methodology showed that the temperature ratio has a considerable effect on the reaction rates of the reduced kinetic model. The temperature ratio, also called non-thermal degree, is an implicit comparison between VV and VT relaxation. An efficient dissociation of CO_2 is possible at low temperatures and high non-thermal degrees, when the vibrational energy is predominantly exchanged between vibrational levels (VV relaxation) instead of being lost as heat (VT relaxation).

An engineering approach for modeling non-thermal plasma reactors was developed. The inputs for the modeling approach are parameters that can easily be measured experimentally, such as power and process conditions, instead of intermediate plasma variables, such as electron density or vibrational temperature. Likewise, as a result of the modeling approach, the reactor performance can be evaluated in the engineering terms of conversion and energy efficiency.

The modeling approach consists of two steps, a plasma characterization step using simple chemistry and a performance evaluation step using the actual chemistry of interest. In the first step, a multidimensional self-consistent plasma reactor model can be used with a simple plasma chemistry to circumvent the numerical instabilities that arise when implementing complex non-thermal plasma chemistries, which frequently impede the solution of the equations. Among the results of this first step is the analysis of the power deposition along the reactor,

including the estimation of power losses and the calculation of the power deposition densities. In the second step, the outcome of the first step is used to develop a zero-dimensional volume-averaged plasma model, under a Lagrangian description, to represent a one-dimensional model of the plasma reactor. By using the chemistry of interest, it is possible to evaluate the performance of the reactor for the chemical process. Moreover, the reduction methodology with a fictitious species can be used if vibrationally enhanced dissociation must be included in the model, as was shown for CO_2.

The reduction methodology, the modeling approach and the findings presented in this thesis are the result of CO_2 dissociation study in a non-thermal microwave plasma reactor. Nevertheless, these are based on general fundamentals that apply to other types of discharges and chemistries as well. Therefore, the reduction methodology and the modeling approach can potentially be applied to discharges with similar characteristics to those of non-thermal microwave plasma and similar chemistries to that of CO_2, such as pure molecular plasmas of diatomic and triatomic molecules. The modeling approach can be used for process engineering applications involving the design, optimization and verification of plasma reactors and their performance. The reduction methodology can be implemented in the modeling approach when the vibrational kinetics are considered relevant.

5.2. Outlook

The modeling of non-thermal plasma reactors for chemical processing applications is a highly sophisticated task. Several challenges must be addressed to improve the quality, practicality, and accuracy of plasma models for engineering purposes. It is well known that the intricated chemistry of non-thermal plasma is usually the most complicated aspect of such models. In this regard, a better understanding of some molecular processes is still needed, as well as reliable cross section data and rate constants, which are not yet fully available. Further efforts and new approaches to investigate such processes are therefore needed. Similarly, there is still need for practical approaches to model non-thermal plasma reactors for engineering purposes, such as the one presented here. The recent release of commercial packages for plasma modeling, such as COMSOL Multiphysics and PLASIMO, is a step in the right direction. However, the numerical instabilities that arise when solving multidimensional self-consistent models with complex chemistries must be tackled. The continuous increase in computing performance surely helps to

overcome these challenges, but the breakthrough of quantum computers could perhaps be of a major benefit.

CO_2 dissociation in non-thermal microwave plasma reactors at industrial scales has been elusive for a long time due to several challenges, most of them interrelated. An efficient dissociation requires low electron temperatures and high electron densities; however, these variables are not independent and high electron densities require high electron temperatures. Vibrationally enhanced dissociation and VT relaxation proceed at comparable timescales, but the latter should be avoided or limited at least. The new species produced by the dissociation process also consume power from the microwaves and affect the characteristics of the plasma. In addition, very low pressures are usually needed to retain the non-thermal characteristics of the plasma.

Innovative solutions must be found to disentangle and overcome such challenges. The solutions should include novel catalysts that make use of the vibrational energy, in-situ separation of produced species in the plasma zone, or even means to tailor the EEDF in such a way that higher electron densities can be achieved at lower electron temperatures. Further, an industrial scale non-thermal microwave reactor should employ high power to achieve high throughputs and the microwave leakage should therefore be minimized in view of the energy efficiency. The scalability of microwave power sources is however a well-known challenge by itself. Furthermore, the penetration of the microwaves and the wall loses should both be considered for sizing the reactor. While the former suggests smaller reactors, the latter suggest larger reactors. Flow patterns, such as the reverse vortex flow, can also reduce the wall loses and stabilize the plasma, especially at pressures closer to the desired atmospheric pressure. Such a reactor could find its niche in locations with inexpensive green electricity and vast amounts of CO_2 that can be readily captured. Despite its potential benefits, the use of non-thermal microwave plasma reactors for pure CO_2 dissociation still has intricated challenges to overcome. Perhaps other relevant applications that also benefit from the characteristics of non-thermal plasma can find a shorter course to large-scale applications; for instance, the reduction of CO_2 with hydrogen. In such mixture of molecular gases, the chemistry of radicals formed in the plasma becomes more relevant as an efficient dissociation via vibrational excitation becomes harder to achieve.

A

SUPPORTING INFORMATION – CHAPTER 2

A.1. CO₂ Vibrational levels, energies and degeneracies

Table A.1. Considered vibrational levels, specified by the quantum numbers $(i_1\ i_2\ i_3)$, their energies and degeneracies (g). The vibrational energies are computed from equation 2.2 and the degeneracies from $i_2 + 1$.

	Energy (eV), $E_{(i_1\ i_2\ i_3)}$ $i_1 = 0$			
i_3	$i_2 = 0$ $(g = 1)$	$i_2 = 1$ $(g = 2)$	$i_2 = 2$ $(g = 3)$	$i_2 = 3$ $(g = 4)$
0	0.000	0.083	0.166	0.250
1	0.291	0.373	0.454	0.536
2	0.579	0.659	0.739	0.820
3	0.864	0.943	1.021	1.100
4	1.146	1.223	1.300	1.378
5	1.425	1.501	1.576	1.652
6	1.701	1.775	1.849	1.923
7	1.974	2.046	2.119	2.191
8	2.243	2.314	2.385	2.456
9	2.510	2.579	2.649	2.718
10	2.773	2.841	2.909	2.977
11	3.034	3.100	3.166	3.233
12	3.291	3.356	3.420	3.486
13	3.545	3.608	3.672	3.735
14	3.796	3.858	3.920	3.982
15	4.044	4.104	4.165	4.225
16	4.289	4.348	4.406	4.465
17	4.531	4.588	4.645	4.703
18	4.770	4.825	4.881	4.937
19	5.005	5.059	5.113	5.168
20	5.238	5.290	5.343	5.396
21	5.467			

The vibrational levels $((i_1 + 1)\, i_2\, i_3)$ and $(i_1\, (i_2 + 2)\, i_3)$ are coupled due to the to the proximity of their energy and therefore are grouped into a single species. The total degeneracy of the species is the sum of the degeneracies of the grouped states and is referred to as statistical weight, see table A.2.

Table A.2. Statistical weights of the vibrationally excited species based on the coupled symmetric sublevels.

Species	Grouped vibrational states $(i_1\, i_2\, i_3)$	Degeneracies of grouped states $g = i_2 + 1$	Statistical weight of species $\sum(i_2 + 1)$
$CO_2 v_a$	(0 1 0)	2	2
$CO_2 v_b$	(0 2 0), (1 0 0)	3, 1	4
$CO_2 v_c$	(0 3 0), (1 1 0)	4, 2	6
$CO_2 v_n$	(0 0 n)	1	1
$CO_2 v_{n,a}$	(0 1 n)	2	2
$CO_2 v_{n,b}$	(0 2 n), (1 0 n)	3, 1	4
$CO_2 v_{n,c}$	(0 3 n), (1 1 n)	4, 2	6

A.2. COMSOL Multiphysics solver

The solution of the modeling equations for the different combination of parameters' values was achieved through a parametric sweep, varying one parameter at a time until all combinations were solved. A time-dependent study with a time limit of 0.03 s was used, meaning that for each parameter combination the simulation ran until 0.03 s. This time was proven to be enough to reach the steady state.

The chosen time stepping method was a Backwards Differentiation Formula with minimum order of 1 and a maximum order of 2. An initial time step of 10^{-18} s was used to ensure consistent initial conditions and, as the time-dependent solution progressed, a variable time step was employed.

The equations were solved in a logarithmic formulation, given the very small numbers expected for the dependent variables. An absolute tolerance of 0.001 was specified for all variables in their logarithmic form, which corresponds to a relative tolerance of approximately the same value for the variables in their non-logarithmic form.

The shared-memory multiprocessing parallel direct sparse solver, also known as the PARDISO solver, was the algorithm used to solve the fully coupled set of equations.

Moreover, a constant Newton-Raphson method with a minimal Jacobian update was also specified to minimize the solution time.

Further information on the parametric sweep, the time-dependent study and the solver options and configurations can be found in the COMSOL Multiphysics Reference Manual.

LIST OF PUBLICATIONS

JOURNAL PUBLICATIONS

1. Moreno, S. H., Stankiewicz, A. I. & Stefanidis, G. D. The behavior and modelling of the vibrational-to-translational temperature ratio at long time scales in CO_2 vibrational kinetics. *React. Chem. Eng.* **4**, 2108–2116 (2019).

2. Moreno, S. H., Stankiewicz, A. I. & Stefanidis, G. D. A two-step modelling approach for plasma reactors – experimental validation for CO_2 dissociation in surface wave microwave plasma. *React. Chem. Eng.* **4**, 1253–1269 (2019).

3. de la Fuente, J. F., Moreno, S. H., Stankiewicz, A. I. & Stefanidis, G. D. On the improvement of chemical conversion in a surface-wave microwave plasma reactor for CO_2 reduction with hydrogen (The Reverse Water-Gas Shift reaction). *Int. J. Hydrogen Energy* **42**, 12943–12955 (2017).

4. de la Fuente, J. F., Moreno, S. H., Stankiewicz, A. I. & Stefanidis, G. D. Reduction of CO_2 with hydrogen in a non-equilibrium microwave plasma reactor. *Int. J. Hydrogen Energy* **41**, 21067–21077 (2016).

5. de la Fuente, J. F., Moreno, S. H., Stankiewicz, A. I. & Stefanidis, G. D. A new methodology for the reduction of vibrational kinetics in non-equilibrium microwave plasma: application to CO_2 dissociation. *React. Chem. Eng.* **1**, 540–554 (2016).

ACKNOWLEDGMENTS

My doctoral studies have come to an end. Seven years ago, when I left my home country to pursue a master's degree at TU Delft, I couldn't have imagined that today I'd be writing those words. Herein I would like to thank all the people and the institutions who supported me throughout this journey.

First, I would like to thank my promotors Prof. Georgios Stefanidis and Prof. Andrzej Stankiewicz for encouraging me to pursue a PhD when I was unsure about it. Thank you both for believing in me and for trusting me, especially when I doubted myself. I truly appreciate the autonomy you granted me; it was as enjoyable as it was challenging. Thank you for the support, the guidance and advice that kept me on track. I hope we remain in contact and I wish you the best in your future projects.

I also want to express my gratitude to Leslie van Leeuwen, the assistant of our research group. Leslie, you made our group run smoothly owing to your diligence and responsiveness. Thank you very much for making our lives easier at work.

During these years I had opportunity to meet very talented and friendly people. Among these people I would like to acknowledge the colleagues with whom I shared my office: Javier Fernández, Tim Becker, Meng Wang, Xuan Tao and Hakan Nigar, thank you for the pleasant working environment we had in the office, I wish you the best in your future endeavors. Javier, thank you for bringing your contagious cheerful attitude every day, for the lengthy discussions about plasma and for your support during my master's thesis and the first years of my doctoral studies. Tim, thank you for friendship, for the interesting discussions and for helping me to improve my German, it has been very useful lately. I would like to extend my gratitude to my colleagues of the IRS Research Group and the Process & Energy department for the good times we shared.

My doctoral studies and my master's degree wouldn't have happened without the scholarship awarded to me seven years ago by the TU Delft Process Technology Institute. That scholarship changed my life. For that, for being a good employer, an excellent university and for much more I will be eternally grateful to TU Delft. I will

always cherish the beautiful city of Delft, my home for six years, and the Netherlands for being such a great place to be. The feeling of freedom I felt from the endless blowing wind is perhaps what I will miss the most.

I am equally grateful to Oscar Villamil, Juan Camilo Ortíz and Raúl Fuciños for their long-lasting friendship, for their support and patience, and for making my life in Delft much more enjoyable. Oscar, thank you very much for everything, for always being there, for trusting me and for hearing me out. Camilo, thank you for all the long conversations about everything, for always bringing old forgotten (to me) memories that made us laugh hard and for your help and patience regarding medical advice. Raúl, thank you for all the interesting discussions and for always sharing your peculiar point of views. I also want to express my great appreciation to Maria Alejandra Cardona, Julian Nieto, Carlos Pérez, Laura Arismendi, Daniel Álvarez and Carlos Coy for their friendship and support.

I would like to especially thank my family. Dad, thank you very much for everything you have done, for your resilience and for setting the best example. I will never be able to repay all you have done for me; I am forever indebted to you. I also want to thank my Mom, who departed many years ago but remains in my daily thoughts. She is still the driving force behind many of my deeds, for after all these years I still want to make her feel proud of me. To my brothers, Andres and Miguel, thank you for teaching me intellectual curiosity and determination. Minita y Aminta, my aunts, thank you for all you have done for me, which has been much more than was ever asked or needed. Thank you for your support and for looking after me from the distance. My gratitude also goes to my in-laws, Diva, Gustavo, and María Camila, for their support and for welcoming me with open arms into their family.

Finally, I want to thank my wonderful wife, Mafe. Thank you very much for everything, for all your support and patience, for motivating me and for keeping my spirits high. More importantly, thank you for sharing your life with me, bringing joy along to my own.

Sergio Hernando Moreno Wandurraga
Frankfurt am Main, March 2020

CURRICULUM VITAE

Sergio Moreno was born in 1985 in Bucaramanga, Colombia. In 2008, he completed a 5 years program in Mechanical Engineering at the Universidad Industrial de Santander in Colombia, where he was an Honor Student of the Mechanical Engineering School for 3 years and graduated *Cum Laude*.

Before graduating, Sergio joined the oil industry, where he worked for 5 years in the design, construction and operation of oil production facilities. During this time, he mainly worked in engineering design and project management of large-scale process plants. Afterwards, in search for further development he decided to pursue a master's degree in process engineering.

In 2013, Sergio was awarded a scholarship from the TU Delft Process Technology Institute and enrolled in the Sustainable Processes and Energy Technologies track of the Mechanical Engineering master's program at TU Delft in the Netherlands. In the second year of his master's studies, he devoted his efforts to study plasma reactors, including a short stay at the plasma research group of the University of Antwerp in Belgium, where he proposed a detailed kinetic model for a moderate pressure Hydrogen microwave plasma. By the end of 2015 Sergio successfully defended his master's thesis "Reduced reaction kinetics model for CO_2 dissociation in non-thermal microwave discharges" and graduated *Cum Laude*.

In 2016, Sergio began his doctoral research at the Intensified Reaction & Separation Systems research group of TU Delft, under the supervision of Prof.dr. G. Stefanidis and Prof.dr.ir. A. I. Stankiewicz. During his doctoral research, he continued to develop novel approaches to model plasma reactors. His results were published in a renowned engineering journal and are the matter of this book. After his doctoral research, he joined Evonik Industries AG as a Project Engineer in the Technology & Infrastructure segment.